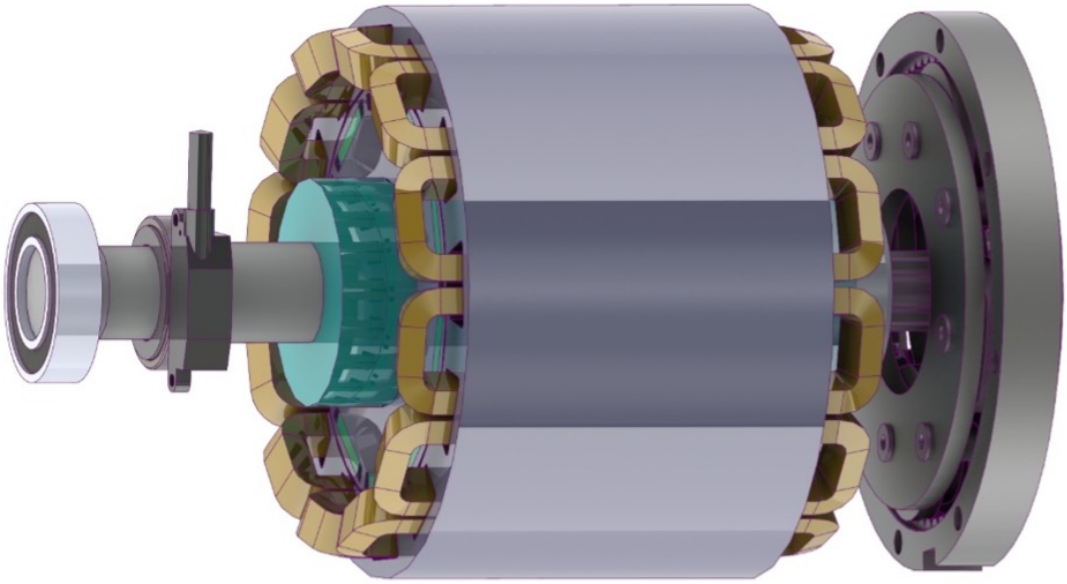

Control and Testing of a PMSM

in a submersible POD system for a medium-size electric leisure boat

M.Sc thesis in Electric Power Engineering

VIKAS SP

Department of Electrical Engineering - Division of Electric Power Engineering

CHALMERS UNIVERSITY OF TECHNOLOGY
Gothenburg, Sweden 2022
www.chalmers.se

Master's thesis 2022

Control and Testing of a PMSM

in a submersible POD system for a medium-size electric leisure boat

VIKAS SP

CHALMERS
UNIVERSITY OF TECHNOLOGY

Department of Electrical Engineering
Division of Electric Power Engineering
Chalmers University of Technology
Gothenburg, Sweden 2022

Control and Testing of a PMSM in a submersible POD system for a medium-size electric leisure boat
VIKAS SP

Supervisors: Junfei Tang, Bowen Jiang, Nimananda Sharma, and Yujing Liu, Electric Power Engineering
Examiner: Yujing Liu, Electric Power Engineering

Master's Thesis 2022
Department of Electrical Engineering
Division of Electric Power Engineering Chalmers University of Technology
SE-412 96 Gothenburg
Telephone +46 31 772 1000

Cover: CAD drawing of the PMSM in question

Typeset in LaTeX
Printed by Chalmers Reproservice
Gothenburg, Sweden 2022

Control and Testing of a PMSM in a submersible POD system for a medium-size electric leisure boat

VIKAS SP
Department of Energy and Environment
Chalmers University of Technology

Abstract

Electrification of the boats is one stream towards sustainable development. A lot of research and development is taking place towards this. Using a Permanent Magnet Synchronous Machine (PMSM) for boat propulsion is suitable because of its properties. A submersible POD system in which the electric machine's cooling is taken care by the natural water is an attractive option to save energy and on-board space. In order to encourage research and development activities in electrification of boat vessels, department of electric power engineering and department of marine technology had taken up a project. As part of this project, a POD system and its components were designed and manufactured. This propulsion system needs a control system designed and the machine needs to be tested. This work highlights the steps followed to achieve this.
First, a PMSM's process model and its control system were developed. The developed control system was verified in *MATLAB-Simulink* environment. Next, hardware testing was carried out to verify the controller and machine's performance using *DSpace-Controldesk* tools. As a next step, in order to have a chip-system to control the PMSM, the control algorithm was programmed to a Texas Instrument DSP *TMS320F28379D* and tested.
The Electrical and Electronic rigging of hardware testing was completed and closed-loop control was tested successfully in the *DSpace-Controldesk* environment. The machine was not operated to full capacity due to limitations in the DC supply. When using the DSP, the control was failing due to noise in the current sensors on the inverter and it was decided that a different inverter module was to be implemented.

Keywords: PMSM modeling, PMSM control design, Closed-loop current control, Hardware testing, Submersible POD system, Propeller-integrated PMSM

Acknowledgements

I would like to thank my supervisor, Professor Yujing Liu, for his constant support and guidance. I enjoyed working in the lab with Junfei Tang, Nimananda Sharma, and Bowen Jiang. Thank you very much for your support, despite having a busy schedule.
I want to thank Stefan Lundberg and Douglas Nilsson for their help in mounting the machine on the test bench. We wouldn't have achieved the objective of the thesis without perfect mounting of the machine. I also want to thank Xiaoliang Huang, Artem Rodionov, Felix Mannerhagen and Georgios Medemlis for sharing their opinion and helping me learn.
Finally, I wish to recognize my family and friends for their constant support, which has kept me motivated and helped me in this work.

Vikas SP, Gothenburg, September 2021

Abbreviations

IC Internal Combustion
IMO International Maritime Organization
PMSM Permanent Magnet Synchronous Machine
DSP Digital Signal Processor
EV Electric Vehicle
CFD Computational Fluid Dynamic
LES Large Eddy Simulation
IPM Interior Permanent Magnet
MMF Magneto Motive Force
EMF Electromotive Force
MTPA Maximum Torque Per Ampere
CCS Code Composer Studio
VSI Voltage Source Inverter
PWM Pulse Width Modulated
IGBT Insulated Gate Bipolar Transistors
SVPWM Space Vector Pulse Width Modulated

Contents

List of Figures **xiii**

List of Tables **xvii**

1 Introduction **1**
1.1 Background . . . 1
1.1.1 History of Electric boats . . . 1
1.1.2 Recent development in marine electrification . . . 2
1.1.3 Research in Marine electrification at Chalmers . . . 3
1.2 Aim . . . 3
1.3 Scope . . . 4

2 Aspects of POD design and its components **5**
2.1 Hydrodynamics . . . 5
2.2 Drivetrain . . . 11
2.3 Thermal evaluation . . . 13
2.4 Gearbox Calculations . . . 16
2.5 Prototype . . . 17

3 Components in PMSM drivetrain **19**
3.1 PMSM . . . 20
3.1.1 Fundamental Electromagnetic Equations . . . 20
3.1.2 Rotor . . . 23
3.1.3 Stator . . . 24
3.1.4 Losses and efficiency . . . 28
3.1.4.1 Copper losses . . . 29
3.1.4.2 Iron losses . . . 30
3.1.4.3 Efficiency . . . 31
3.2 DC/AC Inverter . . . 31
3.2.1 Three Phase Inverter . . . 32

4 Controller design for a PMSM **39**
4.1 Modeling a PMSM . . . 39
4.1.1 Flux linkage in a PMSM . . . 39
4.1.2 Space Vectors and Alpha-Beta Coordinates . . . 39
4.1.3 Process model . . . 44
4.2 Controller design . . . 44

4.2.1 Current Controller according to IMC 45
4.2.2 Maximum Torque Per Ampere (MTPA), Current and Voltage limit 46
4.2.3 Speed and position controller 49

5 Testing and tuning the controller **53**
5.1 MATLAB-Simulink environment 53
5.2 DSpace-Controldesk environment 55
5.3 DSP-Code Composer Studio (CCS) environment 56
5.4 Test Setup 58

6 Results and Conclusion **61**

Bibliography **65**

A Appendix 1 **I**
A.1 Main file I
A.2 Interrupt function VI
A.3 EQEP Function XV

B Appendix 2 **XIX**

List of Figures

1.1 Jacobi's electromotor.[2] 2
1.2 Eelex 8000.[3] 3
1.3 Candela C7.[4] 3
1.4 Leisure boat for design consideration: Ryds 510GTI.[7] 4
1.5 Ryds 510GTI: Outboard IC removed.[7] 4

2.1 Velocity distribution in the wakes behind smaller POD diameter.[7] . 6
2.2 Velocity distribution in the wakes behind larger POD diameter.[7] . . 6
2.3 Propeller efficiency versus the POD to Propeller diameter ratio.[7] . . 6
2.4 Propeller characteristics curve for a Wageningen B-series propeller.[7] 6
2.5 Power estimation at different boat speeds[7] 7
2.6 Different head form geometries (diameter 160 mm, length 400 mm)[7] 8
2.7 Velocity distribution around different head form geometries)[7] 8
2.8 Velocity distribution around different head form geometries[7] 8
2.9 A conventional outboard with combustion engine (left) and an electric outboard (right).[7] 9
2.10 Cross section of the Strut. Solid lines show the cross-section profiles and the dashed lines show the inner volume of these cross sections after considering the material thickness. Note that the x and y axis scales are not the same.[7] 9
2.11 Pressure distribution along two profiles. *Cp* is the *Pressure Coefficient.*[7] 9
2.12 Skeg cross section.[7] 9
2.13 Assembly of the pod system.[7] 10
2.14 Non-dimensional axial velocity distribution in around the electric outboard. Vertical structures in the flow are visualized using iso-surface of Q-criterion.[7] 11
2.15 Non-dimensional axial velocity distribution at the propeller upstream.[7] 11
2.16 Pressure distribution on the pod system.[7] 11
2.17 Time history of propeller thrust.[7] 11
2.18 Efficiency curves with and without Strut.[7] 12
2.19 Integration of Machine, gearbox, encoder and bearings.[7] 13
2.20 CAD diagram showing placement of inverter.[7] 14
2.21 Average temperature of the Aluminum backplate.[7] 14
2.22 Temperature in celsius at the surface and inside the aluminum-housing for 1 m/s.[7] 15

2.23 Temperature in celsius at the surface and inside the aluminum-housing for 14 m/s.[7] . . . 15
2.24 Inner and Outer temperature in celsius of the active components' housing for 12.5 m/s.[7] . . . 15
2.25 Inner and Outer temperature in celsius of the active components' housing for 0.5 m/s.[7] . . . 15
2.26 Actual geometry of the Gearbox housing.[7] . . . 16
2.27 Inner and Outer temperature in celsius of the gearbox housing for 12.5 m/s.[7] . . . 16
2.28 Inner and Outer temperature in celsius of the gearbox housing for 0.5 m/s.[7] . . . 16
2.29 CAD drawing of the designed prototype.[7] . . . 17
2.30 Image of the complete POD system that is manufactured.[7] . . . 18

3.1 Components in a PMSM Drive. . . . 19
3.2 Analogy between electric and magnetic circuits.[10] . . . 21
3.3 Force acting on a current carrying conductor placed in magnetic field. 23
3.4 Different rotor topologies for PM motors and reluctance motors and the amount of torque from reluctance and permanent magnets.[11] . . 24
3.5 Rotor of the PMSM manufactured as part of the project . . . 24
3.6 Placement of the magnets and reluctance gaps in the rotor . . . 25
3.7 2 pole stator with winding and resulting magnetic field. . . . 26
3.8 Illustration of slots, phase belts and repeatable groups with $m = 3$, $p = 4$, $q = 1$.[10] . . . 27
3.9 Illustration of Electrical and Mechanical cycles w.r.t repeatable groups with $m = 3$, $p = 4$, $q = 1$.[10] . . . 27
3.10 Star diagram for $m = 3$, $p = 4$, $q = 2$.[10] . . . 28
3.11 Star diagram for $m = 3$, $p = 4$, $q = 2$ and Short-pitch.[10] . . . 28
3.12 Star diagram for $m = 3$, $p = 4$, $q = 2$ and long-pitch.[10] . . . 28
3.13 Connections as per table 3.2. . . . 29
3.14 Vertical cross-sections of Stator of the PMSM to which the Propulsion system is designed in this thesis. . . . 30
3.15 Slots of the stator . . . 30
3.16 Block diagram representing a single phase rectifier. . . . 32
3.17 Output v_0 and i_0 waveforms.[13] . . . 32
3.18 4 quadrants of operation of a Single phase switch mode inverter. . . . 32
3.19 Waveforms showing $v_{control}$ and v_{tri}.[13] . . . 33
3.20 One-leg switch mode inverter. . . . 33
3.21 V_{A0} and Fundamental frequency as a result of switches T_{A+} and T_{A-} turning ON and OFF for one-leg switch mode inverter ($m_f = 15$ and $m_a = 0.8$).[13] . . . 34
3.22 Three phase inverter circuit with three legs. . . . 34
3.23 v_{tri} and three sinusoidal control voltages to obtain balanced three phase output voltages ($m_f = 15$). [13] . . . 34
3.24 Line voltage V_{AB} waveform. [13] . . . 35
3.25 Three phase inverter harmonic spectrum. [13] . . . 35

3.26 Waveforms showing ideal switching and with blanking time. [13] . . . 37
3.27 Effect of Blanking time on the sinusoidal input in a single phase PWM inverter. [13] . . . 37
3.28 $HybridPACK^{TM}DC6$. Source: Infineon - $HybridPACK^{TM}DC6$ module manual . . . 38
3.29 Module with the driver PCB. Source: Bronze technologies user manual. 38
3.30 Pins on driver PCB and their description. Source: Bronze technologies user manual. . . . 38

4.1 abc and $\alpha\beta$ co-ordinate system. . . . 40
4.2 abc to $\alpha\beta$ transformation of the Voltage space vector.[6] . . . 41
4.3 Separating each part of the transformation of the stator flux linkage.[6] 42
4.4 Voltage and Total flux linkage vectors in $\alpha\beta$ system. Ψ_m is the magnet flux linkage, L_s accounts for leakage and mutual inductance. [6] . . . 42
4.5 $\alpha\beta$ system to dq-representation.[6] . . . 43
4.6 dq voltages and inductances for perfect field orientation $\phi_r = \theta_r$.[6] . . 43
4.7 Electrical Torque from the Electrical power derivation with K=1.[6]. . 43
4.8 Equivalent circuit model of the PMSM in dq co-ordinate system, voltages and mechanical equations.[6] . . . 44
4.9 d and q currents for the process model . . . 44
4.10 The system for the current regulator.[6] . . . 45
4.11 The system for the current regulator with perfect feed-forward terms.[6] 45
4.12 Process equations . . . 45
4.13 Close-loop system.[6] . . . 46
4.14 Step response of a close-loop system.[6] . . . 46
4.15 Graphical representation of maximum current on dq-plane.[6] . . . 47
4.16 Voltage limit ellipse meets current limit circle. The black curve is MTPA line.[10] . . . 48
4.17 Current references' calculations . . . 48
4.18 Current controller with voltage limiter and antiwindup of the integrator (d-current).[6] . . . 49
4.19 Block system of Machine and its current controller with the current limiter.[6] . . . 49
4.20 Design of speed controller as per IMC. . . . 50
4.21 Speed controller with antiwindup.[6] . . . 50

5.1 3 Phase simulink model of a PMSM. . . . 54
5.2 State-space model of PMSM in dq co-ordintes implemented in Simulink. 54
5.3 Process model and controller block in Simulink. . . . 55
5.4 Tranformation blocks, current controller and speed controller. . . . 55
5.5 Current controller structure. . . . 55
5.6 Speed controller structure. . . . 56
5.7 Components in Hardware testing using DSpace. . . . 56
5.8 PWM generation with Up/Down counter using on board oscillator.[15] 57
5.9 TMS320F28379D used in the testing along with Encoder (Green PCB board). . . . 58
5.10 Image showing POD and the steel bucket. . . . 59

5.11 Image showing Torque transducer between the PMSM and the DC Motor. 59
5.12 Image showing PMSM connected to the DC Motor. 59

6.1 Graph showing Resistance vs. Frequency. 62
6.2 Graph showing Inductance vs. Frequency. 62
6.3 Line-to-line voltages and frequency for a propeller speed of 750 RPM. 62
6.4 Torque-Speed points achieved in *DSpace-Controldesk* environment . . 63

List of Tables

1.1 Few full electric boat models. [5] 2
1.2 Characteristics of the assumed boat in this study (Ryds 510GTI)[7] . 4

2.1 Propulsion system performance prediction.[7] 12
2.2 Suitable Machine's specifications decided for the project.[7] 13

3.1 Winding arrangement parameters 26
3.2 Connections of repeatable groups to form the example machine output.[10] 28

6.1 Line-to-line Resistance and Inductance measured in LCR-meter. . . . 61
6.2 Torque and speed levels reached with the available DC supply and in *DSpace-Controldesk* environment 62

1
Introduction

Electrification of boats has many advantages. Electric boats have zero emission, it is easy to start and operate, it is comfortable as there is no engine noise and vibration, it requires less maintenance, it is less bulky and creates possibility to access the protected areas forbidden to navigation with Internal Combustion (IC) engine[1]. Owing to these advantages and pollution caused by marine transportation, International Maritime Organization (IMO) has published an ambitious road-map for reducing overall marine sector emissions by 40% and 70% compared to 2008 levels in 2030 and 2050 respectively[1]. With stricter government schemes and IMO's regulations, the popularity of electric boats is increasing and currently there are many companies working towards development of electric leisure boats, electric boat taxis, electric hydrofoils, and electric sail boats.

This chapter gives a brief history of electric boats, recent developments towards electrification of boats based on a market analysis, aim, and scope of this thesis.

1.1 Background

1.1.1 History of Electric boats

The first electric boat was developed by Moritz von Jacobi in May 1834. This was a paddle boat which had an electric motor powered by zinc batteries. In September 1838, the boat made its first trip on the Neva River in St. Petersburg with 14 passengers on board. With the development of rechargeable, light and less bulky batteries, the commercial production of electric boats was started after 1880.[2]

By 1882, the *Electrical Power Storage Company* built and sold the first few electric boats on the Thames River in England. The first boat was a steel boat which was powered by batteries. These boats had a range of 6 hours when sailing at 13 kmph average. In 1887, Moritz Immisch together with Viscount Bury built electric boats and charging stations around the same location.[2]

By 1920s, IC engines started dominating and popularity of electric boats declined. However, electric boats were still built for environmentally sensitive areas like the Königssee Lake in Germany, where steam and motor boats were banned. Electric outboard motors for trolling and electric motors in submarines remained in use.[2]

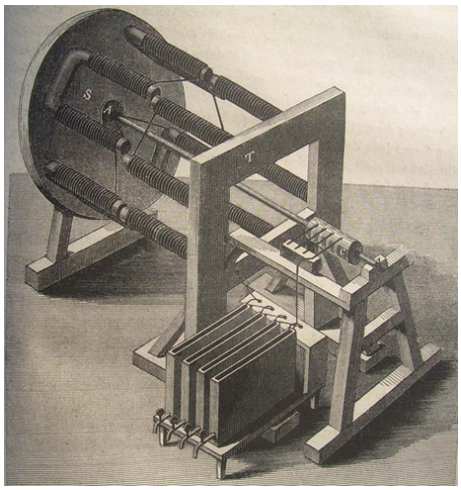

Figure 1.1: Jacobi's electromotor.[2]

Commercial electric boats experienced a revival in the latter decades of the 20th century. Duffy Electric Boat Company of California began mass producing small electric craft in 1968. Boats powered by solar panels emerged in the 1980s.[2]

1.1.2 Recent development in marine electrification

Market analysis has showed that in the last few years there has been major development in this field. [5] aims to present a survey on the state-of-the-art of commercial electric leisure boats. The review is based on companies attending some of the most important international boat shows, thus, it presents only a partial overview of this constantly changing market. In [5], commercial solutions have been analysed and presented considering two categories: Electric propulsion systems, which can be installed on existing boats as retrofit options, and Full Electric Boats. Few organizations that have completely dedicated to development of Electric propulsion systems for boats are Oceanvolt, Torqeedo, Aquawatt, Aquamot, and EPropulsion[5]. Table 1.1 shows the few new Full Electric Boats and their main specifications.

Table 1.1: Few full electric boat models. [5]

Brand	Model	Length (m)	Rated Power (kW)	Rated capacity (kWh)	Rated (Top) speed (km/h)	Range (km @ km/h)
XShore	Eelord 6000	5.8	220	90/120	45 (75)	-
XShore	Eelex 8000	8.0	220	90/120	33 (75)	-
Candela	C-7	7.7	55	45	40 (56)	90 @ 40
Neocean	Overboat	3.1	3	3.4	14(20)	40 @ 20
Hovercraft	Electricat	8	3.7/11.2	-	14/25(-)	100 @ 14/25

Few notable organizations have implemented cutting-edge technology to develop next generation fully electric boats. XShore has developed two boats: Eelord 6000 and Eelex 8000 (figure 1.2). These boats are both powered by a 220 kW inboard motor. The top speed is about 75 kmph, whereas the cruising speed is stated to be approximately 45 kmph and 33 kmph respectively. The lithium battery capacity can be either 90 kWh or 120 kWh and guarantees more than 180 km range when sailing slower than the cruising speed. Candela designs and produces high-performance

Figure 1.2: Eelex 8000.[3]

Figure 1.3: Candela C7.[4]

motorboat inspired by fighter jet and airplane design. Candela Seven (figure 1.3) is indeed extremely light but highly impact resistant as hull and deck are made up of carbon fibre. Contrary to the traditional boats, the hydrofoils provide a more efficient way of cruising as the drag decreases with the increase in speed. Candela Seven also mounts a 50 kW Torqeedo system (Deep Blue 50) and a 40 kWh battery, enabling the boat to sail for more than 90 km at 40 kmph.[5]

All these companies' common and ultimate aim is to reduce the size of the electric motor, reduce the size of the battery system, extend the range, reduce the wake caused by the boats, increase the efficiency of the boat's propulsion system, increase the comfort and safety of the passengers, and reduce the overall cost of the boat.

1.1.3 Research in Marine electrification at Chalmers

To promote research activities in marine electrification, the department of electric power engineering along with department of naval architecture have taken up a project in January 2018. The main objective of this project is to develop propeller-integrated motor drive concept in order to reduce CO_2 emission and improve harbor and marine environments. Various design topologies of submerged drive-train are to be investigated by analytical methods and advanced simulations. The models to be used include magnetic, electric, thermal, mechanical, and fluid dynamic models. One of the main technical challenges is to find compact motor solutions that will yield highest propeller efficiency. A submersible POD system is designed that will replace the existing combustion outboard IC engine in a medium-size leisure boat. The design dimensions are of Ryds 510GTI (figure 1.4). The aspects that are to be considered before finalizing the POD system's design is described in the further sections.[7]

1.2 Aim

The aim of this thesis is to develop a stable closed-loop speed controller for the prototype PMSM that is designed and manufactured as part of the project. The steps taken towards this can be divided in to following sub-aims:

1. Develop the process model of the PMSM covering most of the important fea-

Figure 1.4: Leisure boat for design consideration: Ryds 510GTI.[7]

Figure 1.5: Ryds 510GTI: Outboard IC removed.[7]

Table 1.2: Characteristics of the assumed boat in this study (Ryds 510GTI)[7]

Specification	Dimension
Weight	495 kg (including 2 people onboard)
LOA (Length Overall)	510 cm
Length of Waterline	380 cm
Breadth	200 cm
Draft (max in the aft)	38 cm
Draft (at max breadth)	8 cm

tures. Develop the closed-loop controller and verify it in *MATLAB-Simulink* environment. Record the input and output of the Controller to use in the later stages of verification.

2. Rig up the setup for hardware testing in *DSpace-Controldesk* environment. The inverter should be powered by a DC source and should be controlled by *DSpace*. The current sensors and speed sensors should be configured.
3. To have a chip system in the boat to control the machine, program the Texas Instrument DSP (Digital Signal Processor) *TMS320F28379D* and test if the control can be achieved. Necessary changes in the Hardware setup should be done.

1.3 Scope

The thesis work covers development of closed-loop controller and carryout hardware testing to verify control and machine's performance. Other aspects involved in design of the POD system is not covered in scope.

- As stated in the sub-aim, the controller is first verified in the *MATLAB-Simulink* environment and hardware testing is done using *DSpace-Controldesk* tools.
- The machine's performance is tested to the speed-torque trajectory followed for boat application. This is different for Electric Vehicle (EV) applications and does not need field weakening.

2

Aspects of POD design and its components

This chapter describes steps taken towards finalizing the POD system's prototype design as part of the project. In general, these are the steps to be followed to design electric POD system for a boat. But, the aspects are not limited to just the ones mentioned.

2.1 Hydrodynamics

When switching from a conventional combustion outboard to an electrical outboard, the system design is affected by increase in the overall weight and change in center of gravity mainly due to battery system. Thus, the boat design needs to be modified. Also, finding the thrust required, estimated power, and overall POD geometry are part of the design.[7]

The POD system can be either pulling or pushing type based on where the propeller is placed (front or behind respectively). Each of these configurations have different hydrodynamic characteristics, since the inflow to the propeller as well as the POD resistance will be different. The POD designed in this project is pushing type where the propeller sits downstream, but, both types were evaluated.[7]

The ratio of propeller to POD diameter for boat specifications needs to be determined. In order to deliver a certain power, it is more appealing to increase the electric machine's diameter. However, since propeller is placed behind the machine, the inflow to the propeller is directly influenced by the machine's diameter. On the other hand, a larger diameter of machine results in an increased resistance. Thus, there should be a compromise between the efficiency of the electric machine and propeller efficiency through adjusting their diameter ratio.[7]

Both Computational Fluid Dynamic (CFD) simulations and analytical formula has been employed to study the change in the propeller efficiency by varying the POD to propeller diameter ratio. Upon studying the velocity distribution in the wake of the two ellipsoidal PODs at the speed of 12.5 m/s (24.3 knots), the POD resistance and nominal wake information is extracted (figures 2.1 and 2.2). Adding the boat resistance to this will give the total required thrust. Assuming the propeller diameter to be a constant value, the propeller efficiency is estimated from an analytical

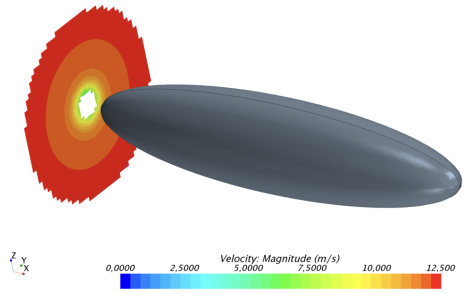

Figure 2.1: Velocity distribution in the wakes behind smaller POD diameter.[7]

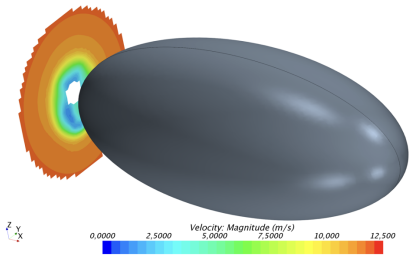

Figure 2.2: Velocity distribution in the wakes behind larger POD diameter.[7]

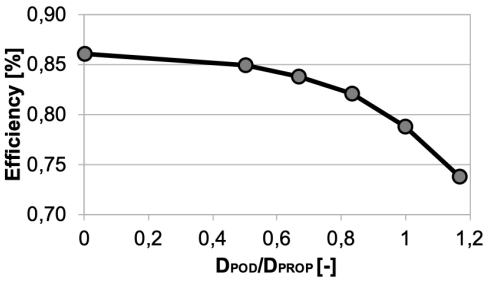

Figure 2.3: Propeller efficiency versus the POD to Propeller diameter ratio.[7]

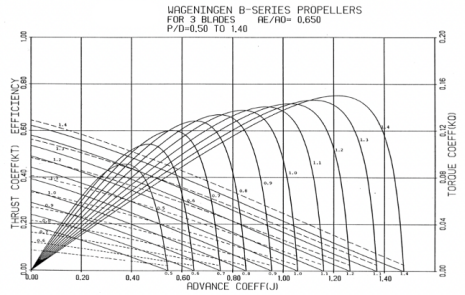

Figure 2.4: Propeller characteristics curve for a Wageningen B-series propeller.[7]

approach (actuator disk assumption) for each of the POD diameters.[7]

The propeller efficiency variation for different POD to propeller ratios are shown in Figure 2.3. It is seen that the propeller efficiency drops as the POD diameter increases. Since this method includes various rough assumptions and does not take the propeller-hull interaction effects into account, a rather large uncertainty is involved in the absolute value presented here. For instance, the 86% propeller efficiency, which is predicted for the propeller without any POD in front of it, is a very large number and should be at least about 10% lower in practice. Therefore, the propeller efficiency roughly varies in the range of 65% to 75% depending on the POD diameter size. In order to estimate the propeller revolution rate, the commercial Wageningen B-series curves were utilized (figure 2.4). For a 3 bladed propeller with blade area ratio of 0.65, propeller efficiency in the range of 65% to 75%, and different propeller pitch ratios, the propeller will have an advance ratio of 0.8 to 1.2. This means that the propeller rotation speed will vary within the range of 2100-3100 rpm.[7]

The required total power to run the boat at different speeds was estimated by means of an empirical tool which is widely being used by naval architects in early phase of designing planing boats (Savitsky method). For the design dimensions considered and 65% propeller efficiency, the dashed line in figure 2.5 shows the shaft power variation for different speeds. Assuming the accumulated efficiency (including efficiencies of engine, gearbox, hull, electronics etc.) of 75%, the total power consumed is shown in solid line. This curve can be used for estimation of the

battery life for a specific scenario and route.[7]

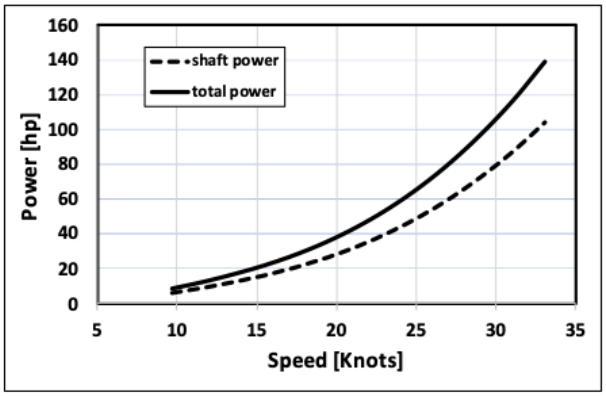

Figure 2.5: Power estimation at different boat speeds[7]

So far, the interaction effects between the POD propulsor and the hull is not included. The POD geometry contributes significantly to the system resistance as well as the characteristics of the hull. The POD geometry is optimized to obtain as low resistance as possible. While evaluating this, a series of head forms for the fore-part of the POD geometry is considered (figure 2.6). The computed velocity distribution around some of these head forms are shown in figure 2.7 and the respective exerted drag force on each of them is plotted in figure 2.8. The split between the pressure force and shear force components is also shown in this figure. Before deciding the geometry, aspects like pressure drag, shear drag, total resistance, and machine's accommodation should be balanced. It was concluded that the head form with the spherical (or semi-spherical) form is the winning alternative with nose lengths around 80, 90 and 100 mm. Risk of cavitation was also evaluated using CFD solver before finalizing the design. Since the aft-part of the POD also influences the system's resistance and more importantly on the flow into the propeller and its efficiency, aft-part's design should also be given importance. Also, the propeller's hub in the conventional fuel engine is used to expel exhaust gases of a combustion outboard engine. This is obviously not required in a electric outboard. Thus, hub geometry will be different between IC engine outboard and electric outboard. The two different geometries can be seen in the figure 2.9. By adopting a cap in the electric outboard, the hub vortex can be avoided and has been evaluated through simulations.[7]

To design Strut (the profile of the POD connecting part to the upper unit), a two-dimensional analysis of the cross section of Strut and upper unit connection has been carried out over two different designs (figure 2.10). The green box in the center of this figure shows the housing for the electronics. The Initial design is easier to manufacture and S1014Modified is supposed to have better hydrodynamical characteristics. S1014Modified is the modified version of standard S1014 airfoil section. The hydrodynamics of these wing sections are studied using *XFOIL* which is an interactive open source program for the design and analysis of subsonic isolated

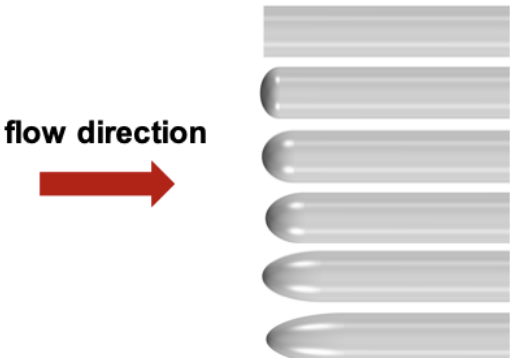

Figure 2.6: Different head form geometries (diameter 160 mm, length 400 mm)[7]

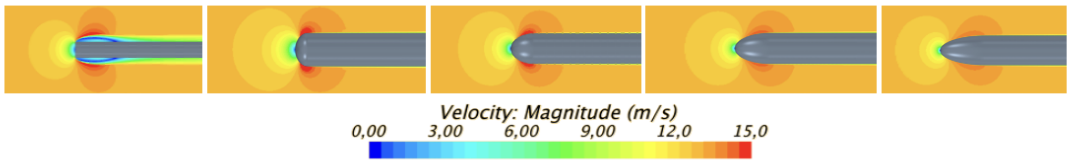

Figure 2.7: Velocity distribution around different head form geometries)[7]

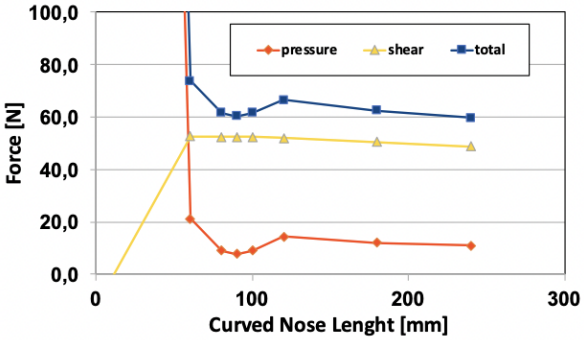

Figure 2.8: Velocity distribution around different head form geometries[7]

airfoils. After specifying *the shape of a 2D airfoil*, *Reynolds* and *Mach numbers*, the code can calculate the pressure distribution on the airfoil and hence lift and drag characteristics (figure 2.11).After studying the drag and lift coefficients for the foils for different angle of attacks, it was concluded that, S1014Modified offers lower drag in comparison to Initial design (only 20% of Initial design) and more or less produces the same lift when the angle of attack is below 3 degrees. After 3 degrees, the performance of modified S1014 drops rapidly. Even though the performance drops, the performance of S1014Modified is better than the Initial design. Therefore, S1014Modified design was finalized. For the Skeg, a wing profile which offers least resistance was chosen. Since it also protects the propeller from running to debris and ground, a slender standard NACA foil profile (NACA 0060) was decided (figure 2.12).[7]

A conventional propeller was decided to be used for demonstration purposes. High-

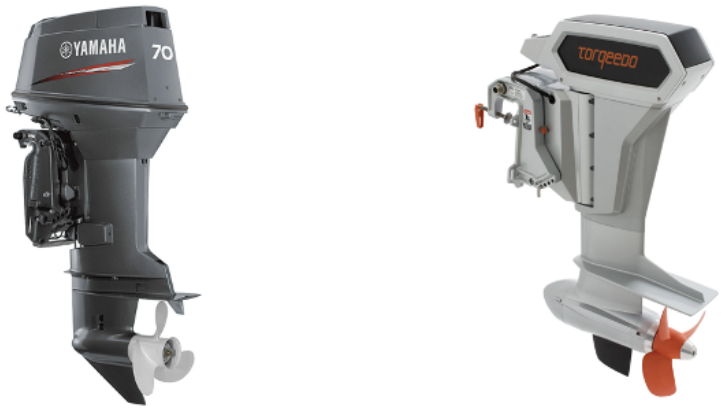

Figure 2.9: A conventional outboard with combustion engine (left) and an electric outboard (right).[7]

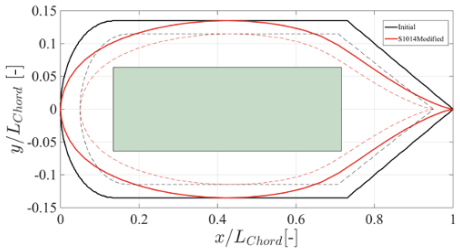

Figure 2.10: Cross section of the Strut. Solid lines show the cross-section profiles and the dashed lines show the inner volume of these cross sections after considering the material thickness. Note that the x and y axis scales are not the same.[7]

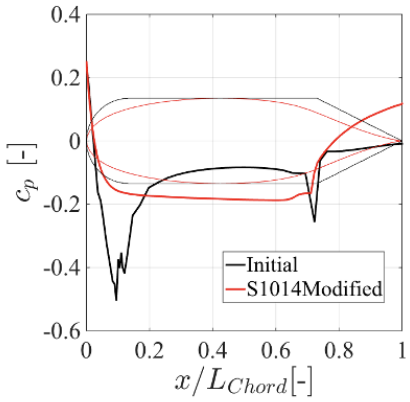

Figure 2.11: Pressure distribution along two profiles. *Cp* is the *Pressure Coefficient*.[7]

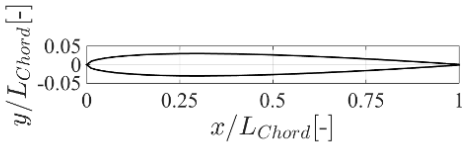

Figure 2.12: Skeg cross section.[7]

performance polyamide 4-bladed propeller which has an adjustable pitch angle was chosen. The assembly of the pod system with finalized Skeg, Strut, and Propeller is shown in figure 2.13. A cavitation plate (anti-ventilation plate) has also been added to this design.

Once the POD system's dimensions are finalized, its propulsion characteristics including the propeller thrust and power at different speeds had to be obtained more accurately. A series of high-fidelity CFD simulations were carried out using *STAR-CCM+*. This software uses a Finite Volume method to solve the mass and momen-

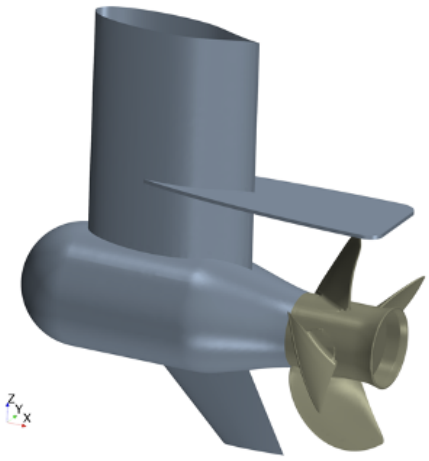

Figure 2.13: Assembly of the pod system.[7]

tum conservation equations in integral form. The Large Eddy Simulation (LES) is used for modeling turbulence. In order to model the propeller rotation, a sliding mesh approach has been used which actually takes the propeller rotation into account. The time step in the simulations is set to be equivalent to the time needed for 1° rotation of the propeller. Figures 2.14 to 2.15 show the extracted results with the undisturbed flow velocity (equivalent to boat velocity) set to 25 knots and the propeller rotation speed is set to be 1900 RPM. The flow shedding is detected behind strut (figure 2.14). The instantaneous inflow to the propeller is also shown in Figure 2.16. This figure also shows that the propeller tip is heavily loaded which causes the formation of a strong tip vortex. A prominent hub vortex is also captured in this simulation. Both these cause energy losses and can be minimized by adding a cone shape hub to close the exhaust opening. The force history of the propeller thrust, shown in figure 2.17, reveals that the variation of propeller thrust is about 2% of the mean thrust. From the results, it was deduced that the blades operate in rather uniform flow throughout one complete revolution and thus, the blade vibrations due to varying force is deemed to be small.[7]

A series of simulations were carried out to calculate the system performance curves. For these simulations, the inflow speed (boat speed) has been kept constant (equivalent to 25 knots) but the propeller rotation speed was increased gradually to obtain different advance coefficients. The resultant advance coefficients (J), propeller torque and thrust as well as predicted powers were obtained as given in Table 2.1. The simulations were carried out with and without the strut and fin to investigate the change in propeller efficiency due to the disturbed wake with strut. It can be seen from the graph (figure 2.18) that the maximum propeller efficiency drops by about 3% in presence of the strut and fin. The propeller efficiency for the pod with strut and fin remains almost constant (60%) between advance coefficient of 1.05 and 1.25. This interval is recommended for propeller operation.[7]

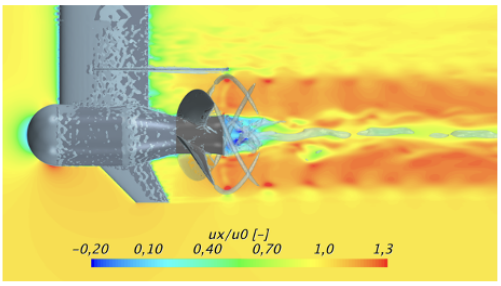

Figure 2.14: Non-dimensional axial velocity distribution in around the electric outboard. Vertical structures in the flow are visualized using iso-surface of Q-criterion.[7]

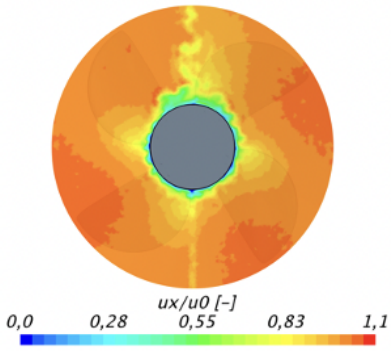

Figure 2.15: Non-dimensional axial velocity distribution at the propeller upstream.[7]

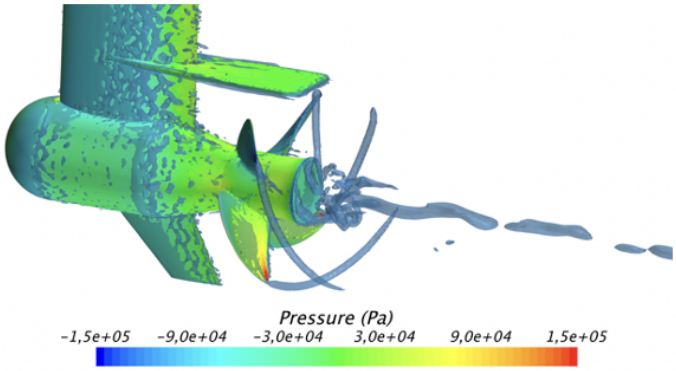

Figure 2.16: Pressure distribution on the pod system.[7]

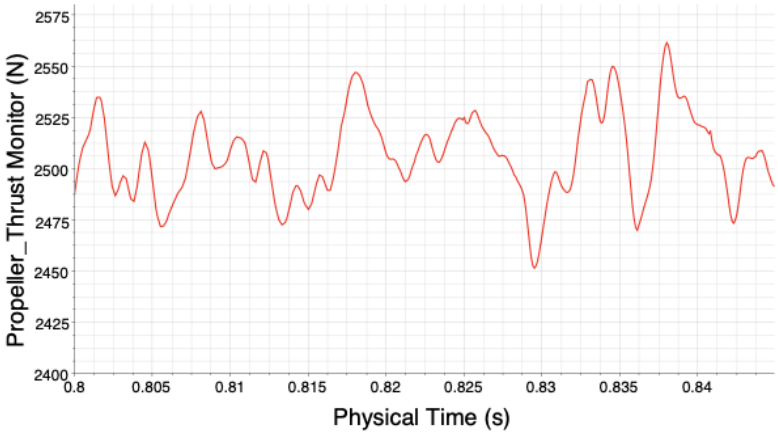

Figure 2.17: Time history of propeller thrust.[7]

2.2 Drivetrain

Based on the knowledge from earlier projects in the automotive and sea-based power generation industry, the drivetrain design is implemented. A PMSM is suitable for

Table 2.1: Propulsion system performance prediction.[7]

Propeller speed	Advance co-efficient	Torque (Nm)	Thrust	Power (Hp)
1500	1.55	93.4	533	19.67
1650	1.41	151.4	1171	35.08
1750	1.33	197	1700	48.41
1900	1.22	262	2504	69.91
2000	1.16	310	3107	87.07
2250	1.03	442	4780	139.66
2500	0.93	587	6577	206.08

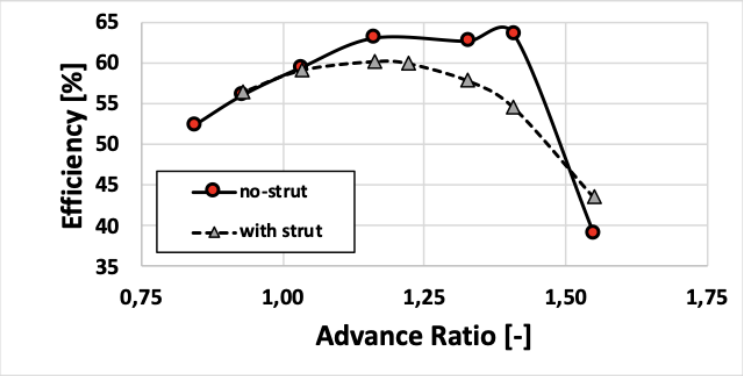

Figure 2.18: Efficiency curves with and without Strut.[7]

boat propulsion due to its robust rotor structure, high power density, and high efficiency. A submersed PMSM is presented in recent publications([8][9]). It is lighter and smaller in size as it does not require a dedicated cooling system. This enables increased motor torque density and saves on-board space for passengers and other equipment. Also, usage of environmentally hazardous coolant, glycol, is avoided[7]. This concept is implemented in the project and is done by placing the electrical machine under the water level in axial direction of the propeller. The speed of the machine was increased to reduce the radius [7]. The speed of the machine is lower than the propeller's speed and the propeller is coupled axially. Thus, a planetary gearbox is needed[7]. To control the thrust of the propeller, the electrical machine needs to be controlled and for this, an inverter is needed. The cooling of the inverter is also taken care by the surrounding water as it is placed in the POD system under the water[7].

Since the torque demand of the propeller is increasing along with speed, no field weakening is necessary. The electrical machine is an Interior Permanent Magnet (IPM) machine with the properties shown in Table 2.2. The integration of the electrical machine together with the gearbox, bearing and positioning sensor can be seen in figure 2.19. To decrease cost and production time, a transistor module together with an off the shelf gate driver board was decided to be used. The voltage was decided to be increased closer to the automotive standards of today to lower the losses of the system.[7]

Table 2.2: Suitable Machine's specifications decided for the project.[7]

Specification	Dimension
Stator outer diameter	150 mm
Stator length with end winding	130 mm
Nominal power	50 kW
Peak power	80 kW
Nominal torque	30 Nm
Peak torque	48 Nm
Rated speed (no field weakening)	16000 RPM
Weight	10 kg
Nominal power density	4.9 kW/kg
Peak power density	7.9 kW/kg

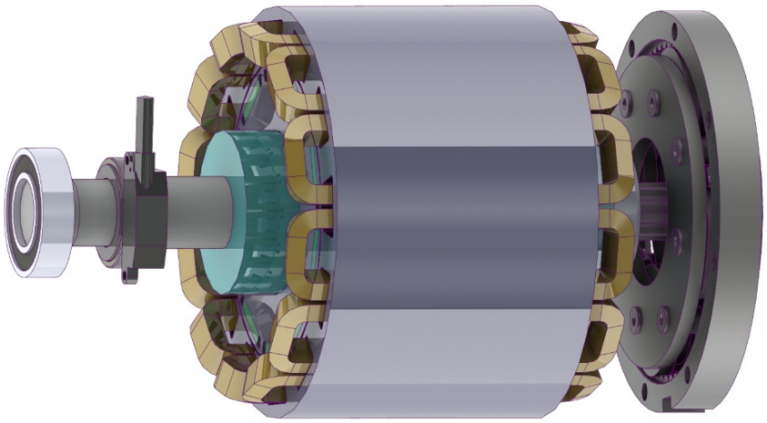

Figure 2.19: Integration of Machine, gearbox, encoder and bearings.[7]

2.3 Thermal evaluation

Since the idea is to place the inverter in the POD (as shown in the figure 2.20), the efficiency of the IGBT module cooling was evaluated using FEM simulations in *COMSOL Multiphysics* environment. *Aluminum 6063-T83* which has thermal characteristics of the one used in the prototype (*Aluminum 6082*), is used as the material. The water velocity is assumed to be the speed of the boat and the water temperature is set to 20° C[7]. For water's speed 1 to 14 m/s (changed in the steps of 1 m/s), the resulting average temperature of the thermal plate of the IGBT is plotted against the boat's speed in the figure 2.21. The temperature at the surface and inside the aluminum-housing can be seen in the figures 2.22 and 2.23. The flow analysis was also carried out during the process. From the results, it was concluded that the thermal capability of the inverter housing is sufficient to handle

the maximum temperature the IGBT module can bear before breaking from internal stress[7].

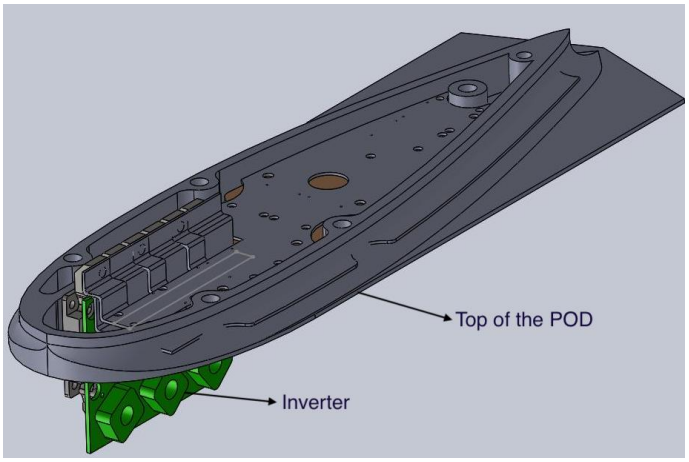

Figure 2.20: CAD diagram showing placement of inverter.[7]

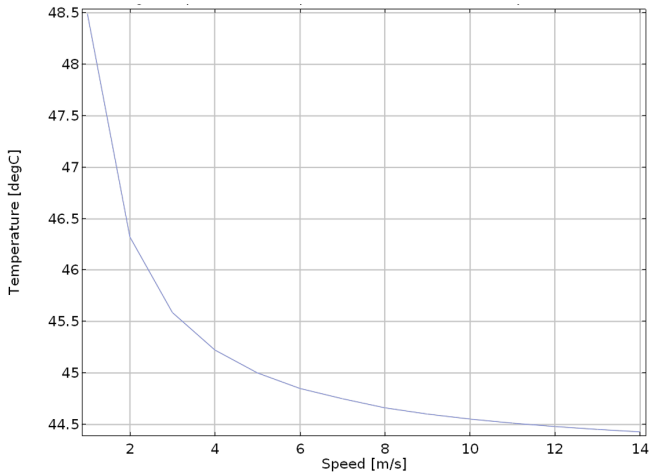

Figure 2.21: Average temperature of the Aluminum backplate.[7]

To verify the cooling of electrical machine and the gearbox, FEM simulation of its housing is done by assuming a laminar flow. To define the heat source, all the losses have been seen to be originating from the machine into the inner surface of the housing[7]. The losses are calculated at the input peak power and is equal to 4.25 kW[7]. The housing has been defined as a rectangle of dimension equal to its thickness. A large water geometry is added such that the outer surface is in contact with the housing. The material is *Aluminum alloy 6063* which has the lowest thermal conductivity. When simulated with water's temperature to be 20° C and the water flow speed of 12.5 m/s (24.3 knots), the inner temperature of the housing is 23° C (shown in the figure 2.24). When the water flow is set to 0.5 m/s, the inner housing temperature is 24.5° C and the outer temperature is 20.6° C (shown in the figure 2.25)[7].

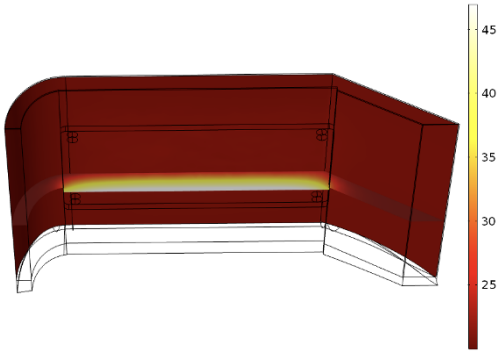

Figure 2.22: Temperature in celsius at the surface and inside the aluminum-housing for 1 m/s.[7]

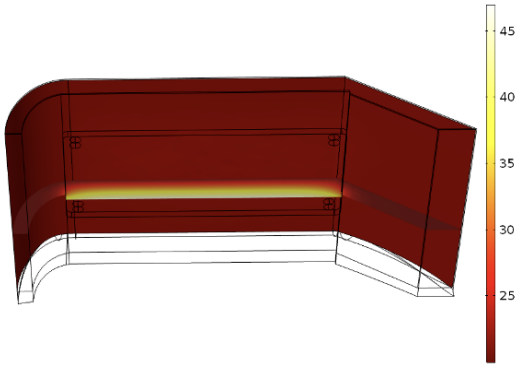

Figure 2.23: Temperature in celsius at the surface and inside the aluminum-housing for 14 m/s.[7]

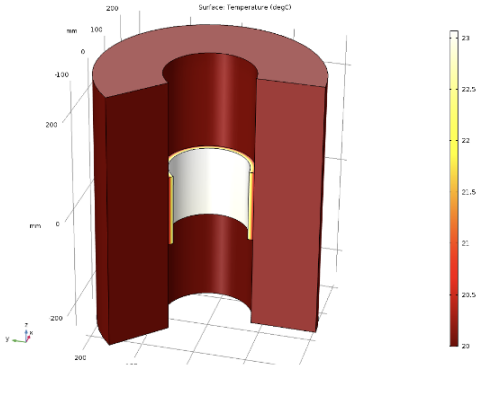

Figure 2.24: Inner and Outer temperature in celsius of the active components' housing for 12.5 m/s.[7]

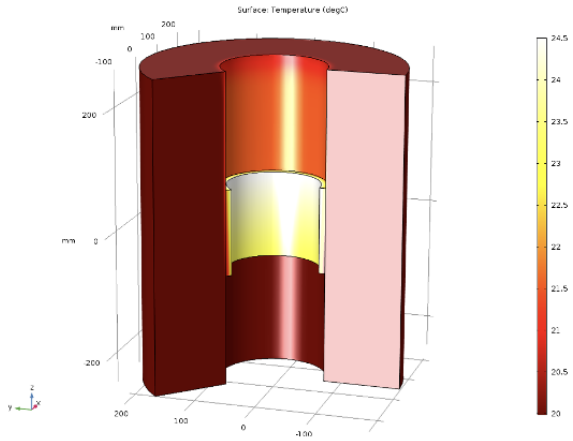

Figure 2.25: Inner and Outer temperature in celsius of the active components' housing for 0.5 m/s.[7]

To verify the cooling of the gearbox housing, the losses have been seen to be traveling from the gearbox and oil into the inner surface of the housing, similar to how it was done for the machine's housing. The losses have been estimated to be maximum 3% of the input power, and for 80 kW this becomes 2.4 kW[7]. The actual geometry of the gearbox housing is as in the figure 2.26. This geometry is simplified to a rectangle for calculations. This simplification gives a lower surface area which gives a lower thermal dissipation[7]. All other settings including geometry and material for the simulation is same as for the machine housing's. With water's temperature 20° C and the water flow to be 12.5 m/s (24.3 knots), the inner temperature on the housing is seen to be 25.3° C and the outer temperature is 20.1° C (as seen in figure 2.27) from the simulations. When water flow is set to 0.5 m/s, the inner housing temperature is 26.1° C and the outer temperature is 21.0° C (as seen in figure 2.28)[7].

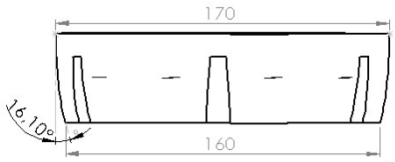

Figure 2.26: Actual geometry of the Gearbox housing.[7]

The thermal calculations are done with both housing placed on top of each other as in the POD assembly and the losses is added to each of the setups. It was concluded that the thermal capability of the machine and gearbox housing is sufficient to handle the peak overall losses.[7]

2.4 Gearbox Calculations

The project team has also calculated the values for the gearbox as part of the project. The gear ratio is decided by a discrete number of teeth to have the gear

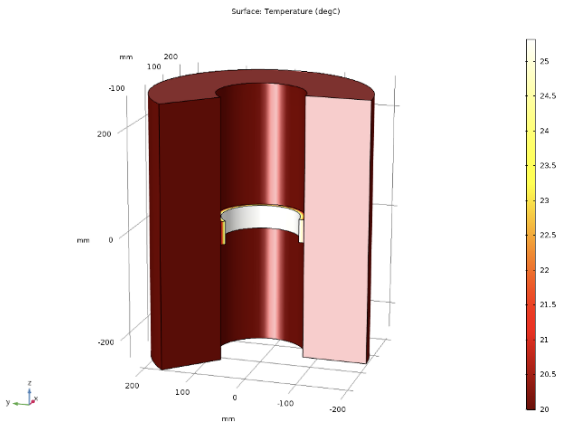

Figure 2.27: Inner and Outer temperature in celsius of the gearbox housing for 12.5 m/s.[7]

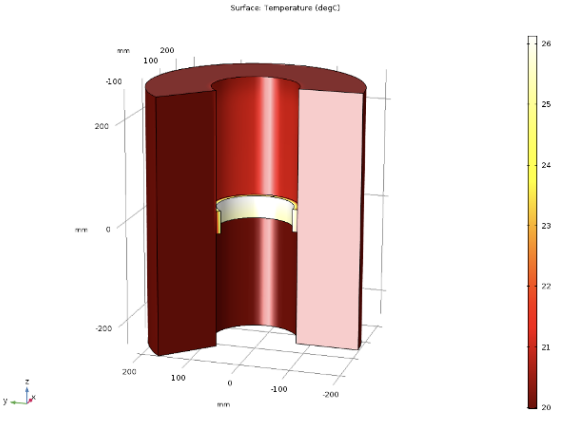

Figure 2.28: Inner and Outer temperature in celsius of the gearbox housing for 0.5 m/s.[7]

ratio more like a guidance number than the specific gear ratio that needs to be the result. The calculations have been done by approximating the cog as a beam for the bending stress and for the contact stress calculation, the two gears have been approximated as two spheres to consider uneven surfaces on the teeth. The forces have been assumed to be loading on one teeth even though there are 4 planet gears that are able to withstand any misalignment. The calculations does not consider the losses, speed dependency, and lubrication. From the calculations on bending and contact stress, *146-5MEF* planetary gear set is found to work with the machine's torque (343 Nm).[7]

2.5 Prototype

Finally, the prototype drawing of the POD system including motor, gearbox, propeller, and inverter is as in the figures 2.29 and 2.30. The prototype is now manufactured and the drive unit requires a speed control system developed. This thesis is about designing a control system for the manufactured PMSM motor and carrying out hardware testing.

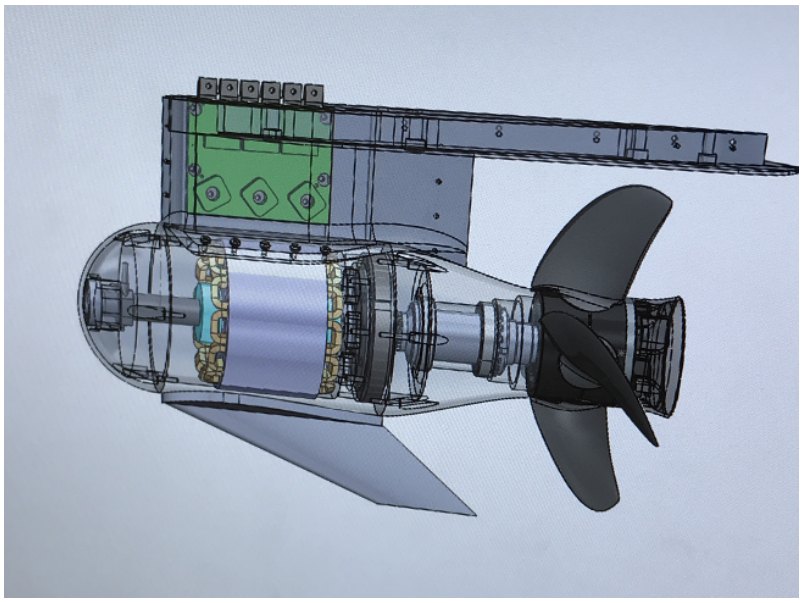

Figure 2.29: CAD drawing of the designed prototype.[7]

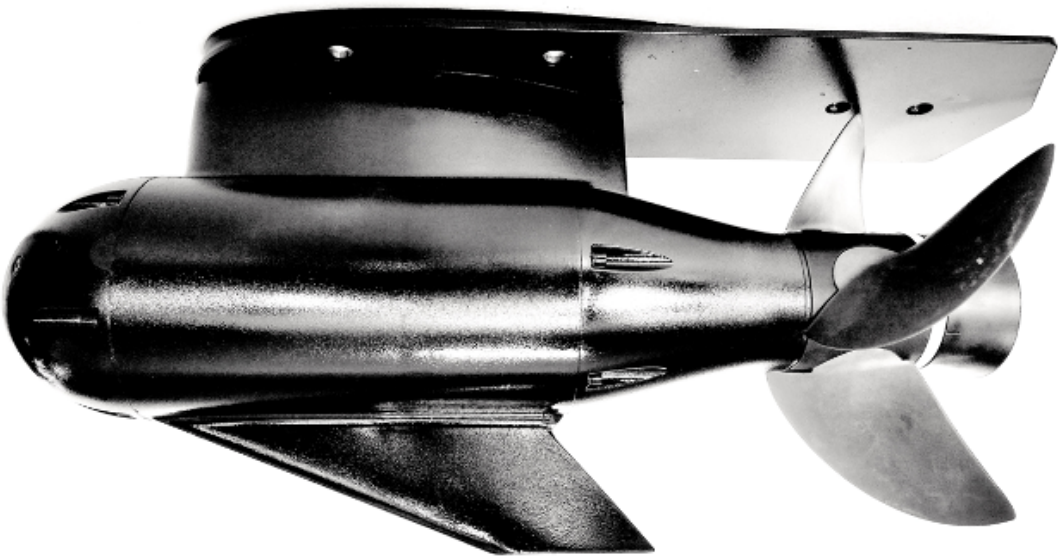

Figure 2.30: Image of the complete POD system that is manufactured.[7]

3

Components in PMSM drivetrain

Figure 3.1 shows the components in a PMSM drivetrain. A PMSM is driven by a DC/AC converter which is fed by a DC source. For the boat's propulsion system, the DC source is a Li-ion battery system. The testing is carried-out using a DC source. The converter receives the time (Duty cycles) for which the six switches should be ON/OFF. In our testing, these signals are given by PWM module in the *DSpace* and Texas instruments DSP *TMS320F28379D*. These signals are based on the output values of the controller. The output values are result of calculations based on the reference values and the actual values. Thus, sensors are needed to measure the actual values (current, speed, position etc.). Since, these sensors measure the analog values and the processor needs the digital equivalents, Analog to Digital interfaces are involved. We will look in the future the importance of co-ordinate transformation blocks in the figure. In this chapter, we will start describing the PMSM, its properties that are critical to model it and design a controller, followed by working and control of inverter.

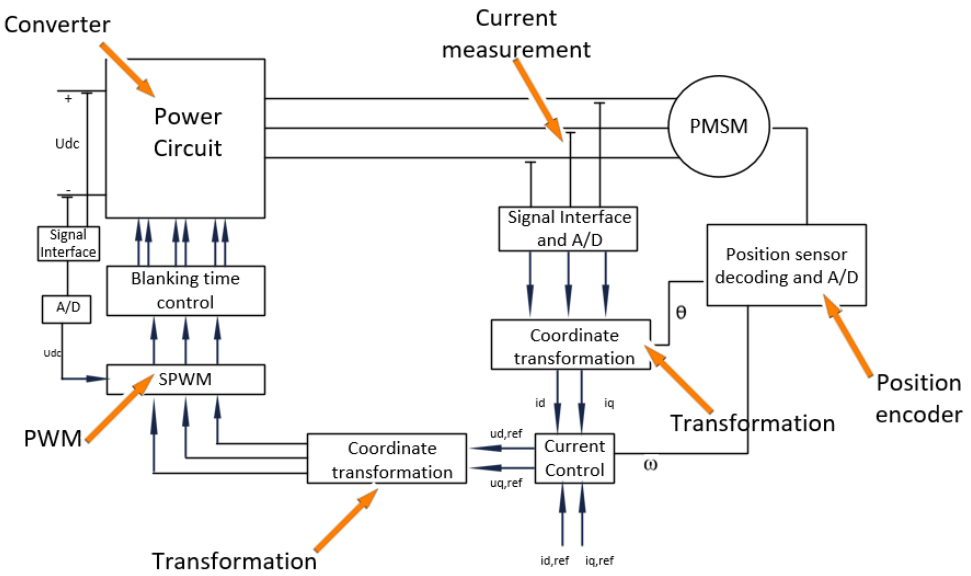

Figure 3.1: Components in a PMSM Drive.

3.1 PMSM

Electrical machines can be broadly classified in to AC Machines and DC Machines. AC Machines are further classified to Synchronous machines and Asynchronous machines. Synchronous machines are further divided in to Permanent Magnet (PM) Machines and non-PM Machines. This section mainly concentrates on the PMSMs as the control is developed for a 50 kW PMSM. We start by describing the electromagnetic properties required for working of a PMSM and main parts in a PMSM. The section also covers different losses involved in a PMSM.

3.1.1 Fundamental Electromagnetic Equations

The fundamental electromagnetic theory and definitions are necessary to understand the working principle of a PMSM. As we know magnetic circuit is analogous to electric circuit as shown in the fig. 3.2. The magnetic field will help in the conversion of electric power to the mechanical power. The magnetic field can be created by current in a coil or permanent magnets and is described by the Ampere's law as in the equation 3.1. I_{encl} is the free enclosed current of the line integral, N is the number of turns in a coil and I is the current through the coil. The product NI is called the *Magneto Motive Force* (MMF). If I_{encl} is an alternating current, then the resulting magnetic field will also be alternating. The direction of the magnetic field is given by right hand thumb rule which states that *if the current is in the direction of the thumb then the magnetic field is in direction of the fingers of a closed right hand.*[10]

$$\oint_l \mathbf{H} \cdot \, dl = I_{encl} = NI \tag{3.1}$$

MMF due to a permanent magnet can be given by the equation 3.2. Where, H_{mag} is the magnetizing force or magnetic field intensity (A/m) of the magnet t_{mag} is the thickness of magnet in the direction of magnet polarization. The reluctance described in the analogy is the level of difficulty experienced by a magnetic flux to flow in a magnetic circuit similar to resistance offered to current in an electric circuit. It is given by the equation 3.3. Where, l is the length of the circuit in metres μ_0 is the magnetic permeability in vacuum equal to $4\pi\times10^{-7}$, μ_r is the relative permeability of the material and A is the cross-sectional area of the magnetic circuit in m^2. The permeability of the material μ is the product.[10]

$$\mathcal{F} = H_{mag} t_{mag} \tag{3.2}$$

$$\mathcal{R} = \frac{l}{\mu_0 \mu_r A} = \frac{l}{\mu A} \tag{3.3}$$

Magnetic flux density corresponding to the produced magnetic field is given by the equation 3.4. Here, the variation of permeability is usually strongly non-linear for magnetic material.[10]

$$\mathbf{B} = \mu_0 \mu_r \mathbf{H} = \mu \mathbf{H} \tag{3.4}$$

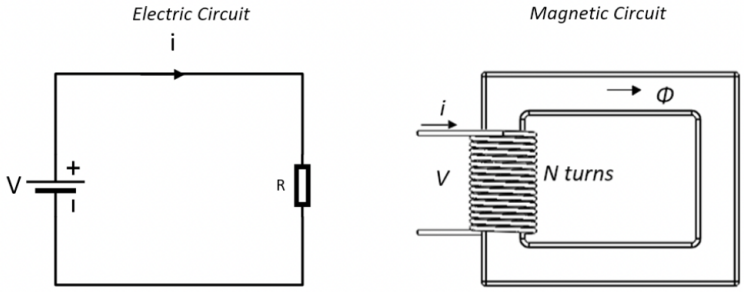

$V = IR$	$\mathscr{F} = \Phi\Re$
V = electromotive force (emf) [V]	$\mathscr{F}$ = magneto motive force (mmf) [A-turns]
I = current [A]	Φ = magnetic flux [Wb]
R = resistance [Ω]	$\Re$ = reluctance
$V = \oint_l E \cdot dl$	$\mathscr{F} = \oint_l H \cdot dl$
$I = \iint_S J \cdot ds$	$\Phi = \iint_S B \cdot ds$
$R = \rho\frac{l}{A}$	$\Re = \frac{l}{\mu A}$

Figure 3.2: Analogy between electric and magnetic circuits.[10]

Also, the corresponding magnetic flux is given by the equation 3.5. This is derived from the Gauss's law of magnetic field. The amount of magnetic flux is decided by the strength of the source of the magnetic field as per Ampere's law. It is limited by the reluctance of the medium in which it flows. In this equation **B** is the Magnetic flux density.[10]

$$\Phi = \int_A \mathbf{B} \cdot \, dA \tag{3.5}$$

The magnetic field and the electric field is given by the combination of Faraday's law and Lenz's law as in the equation 3.6.[10]

$$\nabla \times \mathbf{E} = -\frac{d\mathbf{B}}{dt} \tag{3.6}$$

For calculations, Faraday's law can be simplified to equation 3.7. $\mathcal{E}$ is the Electromotive Force (EMF) and Ψ is the flux linkage. The Flux linkage is the magnetic flux that flows through a coil of N turns if the magnetic flux passes all turns. The minus symbol is as per Lenz' law which states that *the induced EMF is such that the resulting current always opposes the cause producing it.* Thus, the induced EMF is proportional to the rate of change of flux linkage. Using the equations 3.5 and 3.7, the induced EMF can be written as in 3.8. This means that, the EMF can be induced in a coil if the magnetic field is time varying (AC excitation) or the coil cross-section changes with time (DC excitation).[10]

$$\mathcal{E} = -N\frac{d\Phi}{dt} = -\frac{d\Psi}{dt} \tag{3.7}$$

$$\mathcal{E} = -\frac{d(BA)}{dt} = -A\frac{dB}{dt} - B\frac{dA}{dt} \tag{3.8}$$

When the source of the magnetic field is a permanent magnet, the equation 3.8 can be written as in equation 3.9. Where, *A(t)* is the varying cross-section with respect to time. If the rotational frequency is ω then the cross-section, *A(t)* can be expressed as in the equation 3.10. Where, A is the cross-section of the coil when it is perpendicular to the magnetic field ($\omega t = 90°$). Also, the reference direction for calculating the angle of rotation is along the magnetic field. Therefore, the induced voltage will be as in the equation 3.11. Thus, the induced voltage is directly proportional to the frequency of the rotation.[10]

$$\mathcal{E} = -B\frac{dA(t)}{dt} \tag{3.9}$$

$$A(t) = A\sin\omega t \tag{3.10}$$

$$\mathcal{E} = -BA\omega\cos\omega t \tag{3.11}$$

The force acting on an infinitely small charge dQ moving with a speed v in an electromagnetic field is called *Lorentz force* and is given by the equation 3.12. The second part of the equation represents the force acting on a conductor placed in magnetic field. Figure 3.3 shows a conductor carrying current in a magnetic field with the intensity B. f_{em} is the stress created by the changing magnetic field around the conductor. This force on a small length dl can be calculated by using the equation 3.13.[10]

$$dF = dQ(E + v \times B) = (dQ)E + \frac{dQ}{dt}dl \times B = (dQ)E + idl \times B \tag{3.12}$$

$$df_{em} = idl \times B \tag{3.13}$$

Integrating the force over the complete length of the conductor l will give the equation 3.14. Where, $\mathrm{i} = (\mathrm{i_x},\mathrm{i_y},\mathrm{i_z}) = (0,0,\mathrm{i})$ and $\mathrm{B} = (\mathrm{B_x},\mathrm{B_y},\mathrm{B_z}) = (0,\mathrm{B},0)$.[10] The direction of the force is given by the *Fleming's right hand rule*. This force acts in each limb of the coil in opposite direction. Therefore, the torque on the coil is given by the equation 3.15. Here, r is the distance of the limb from centre of rotation, w is the width of the coil and A is the cross-section. If there are N turns in the coil, then the total torque is given by the equation 3.16.

$$f_{em} = li \times B = Bil \tag{3.14}$$

$$T_{em} = 2Bilr = Bilw = BiA = \phi A \tag{3.15}$$

$$T_{em} = N\phi A = \psi A \tag{3.16}$$

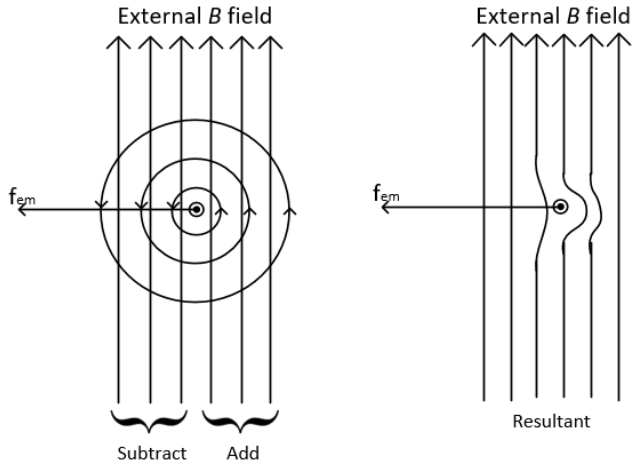

Figure 3.3: Force acting on a current carrying conductor placed in magnetic field.

3.1.2 Rotor

The rotor in a PM Machine is either *round* or *salient*. Round rotor synchronous machines are used in applications with higher speeds (eg: turbo-generators in coal fired or nuclear power plants). Such machines have low pole numbers, typically two or four. Salient synchronous machines are developed for low speed applications and have higher pole numbers (eg: in hydro-electric power plants as generators and rolling mills as motors).[12]
A round rotor synchronous machine has a smooth air-gap i.e., the mutual inductance between the stator and the rotor is constant. Whereas, in salient rotor synchronous machine, the airgap width is minimal at the poles and maximal in between the poles. Hence, the mutual inductance is maximal at the poles and minimal in between. The difference in air-gap will also affect the airgap flux.[12]
Figure 3.4 shows different types of rotors and their corresponding torque characteristics. We concentrate on round-rotor PMSM since that is the one tested as part of this thesis. The rotor should have the same number of poles as stator to latch the magnetic fields produced by the stator and rotor. For a machine with a number of pole pairs as p, it takes the rotor to rotate for $1/p$ revolution to get to the same electrical position as before. The electrical and mechanical angle and speed, electrical frequency are related as in the equations 3.17 to 3.19.

$$\theta_{elec} = p \cdot \Theta_{mech} \tag{3.17}$$

$$\omega_{elec} = p \cdot \Omega_{mech} \tag{3.18}$$

$$f_{elec} = \frac{p \cdot \Omega_{mech.rpm}}{60} \tag{3.19}$$

Figure 3.5 is the rotor of the manufactured PMSM which should be tested and the propulsion system requires to be developed. This is the drawing shared by the

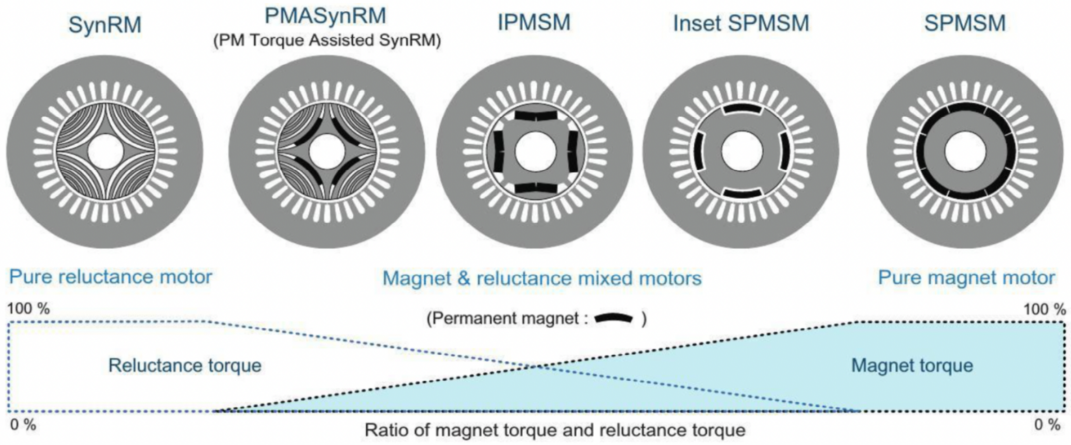

Figure 3.4: Different rotor topologies for PM motors and reluctance motors and the amount of torque from reluctance and permanent magnets.[11]

manufacturer. Figure 3.6 shows the placement of magnets and reluctance gaps in the rotor.

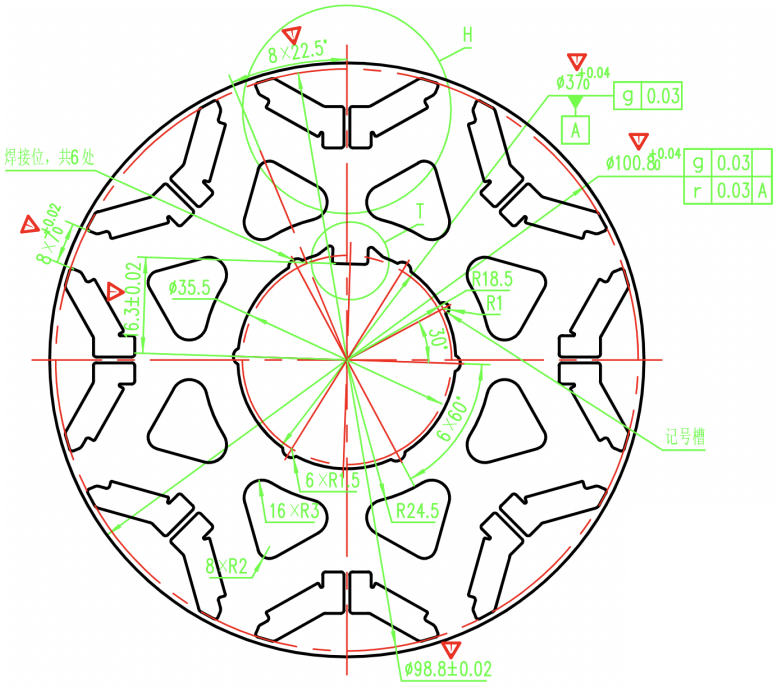

Figure 3.5: Rotor of the PMSM manufactured as part of the project

3.1.3 Stator

Let's consider a 2-pole stator of an electric machine for simplicity as in figure 3.7. The windings of phases A, B and C are separated 120° spatially. The primes A', B' and C' represent the returning of the coils where the current flows in the opposite direction. The current in A, B, C is sinusoidal with the direction in to the paper for

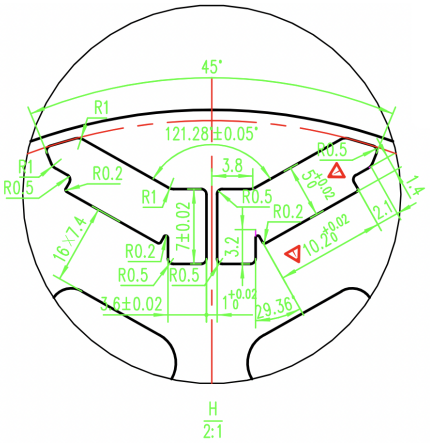

Figure 3.6: Placement of the magnets and reluctance gaps in the rotor

positive quadrants and is also shifted 120° in time between phases. The magnetic field due to alternating current in these winding will be in the direction according to *Right hand thumb* rule as discussed earlier. Accordingly, the pole pair A-A' will produce the magnetic field along the blue line as in the figure 3.7. This is similar to other pole pairs. The flux generated by the pole pairs A, B and C are given by the equations 3.20 to 3.21.[11]

$$\Phi_A = \Phi \sin(\omega t) \cos(\alpha) \tag{3.20}$$

$$\Phi_B = \Phi \sin(\omega t - \frac{2}{3}\pi) \cos(\alpha \frac{2}{3} - \pi) \tag{3.21}$$

$$\Phi_B = \Phi \sin(\omega t + \frac{2}{3}\pi) \cos(\alpha \frac{2}{3} + \pi) \tag{3.22}$$

Φ is the magnitude of the flux and is same for all the phases if the coils are symmetrical. The sine expression represents the current time shift. The cosine represents the geometrical position of the coordinate system where α is the the angle between phase A and the defined coordinate system. If these three vectors are added, the time shift of phases and the positions of the windings will create a rotating magnetic field vector with constant amplitude as in the equation 3.23. The same equation can be scaled for higher number of slots per phase and higher number of poles. [11]

$$\Phi_A + \Phi_B + \Phi_C = \frac{3}{2}\Phi \sin(\omega t - \alpha) \tag{3.23}$$

The total number of slots in a stator is given by the equation 3.24. Where the parameters are described in the table 3.1. A single layer winding arrangement can have concentrated winding and distributed winding based on number of slots per pole per phase. In a concentrated winding, $q = 1$. In that case, $Q = 24$. The coil repeats in the intervals of $2mq$. In this way, the slots under one pole pair form a repeatable group. The Q slots in total are therefore divided into p repeatable groups, and each repeatable group, with $2mq$ slots, covers an electrical angle of 2π. Hence

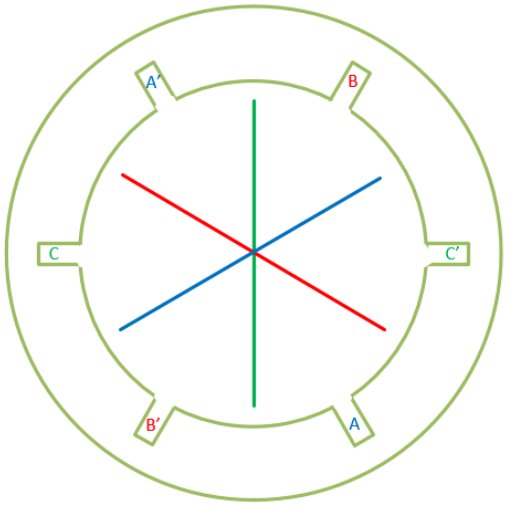

Figure 3.7: 2 pole stator with winding and resulting magnetic field.

in half a repeatable group, mq slots are under one pole and cover an electrical angle of π. The group of adjacent coil-sides belonging to a phase is defined as a phase belt, or named as a phase band. This can be seen in the figure 3.8. Phase belts of A, B and C are marked respectively. As can be noticed, each phase belt covers 60 electrical degrees, and this type of winding arrangement is named as 60° phase belt winding. The 60° phase belt winding is a most common winding arrangement.[10]

$$Q = 2 \cdot m \cdot p \cdot q \tag{3.24}$$

Table 3.1: Winding arrangement parameters

Symbol	Description
m	Number of phases
p	Number of pole pairs
q	Number of slots per pole per phase
Q	Number of total slots

The distance between poles are defined as pole pitch and is denoted by τ. τ is given by the equation 3.25. The distance covered by the coil i.e., distance between A and $A+$ conductors is defined as a coil pitch. It is denoted by y_1. And in concentrated winding arrangement, the winding is always full-pitch, which means the coil pitch y_1 equals the pole pitch τ. The EMF induced in the coils with respect to slots and difference in electrical and mechanical cycles can be visualized with the help of figure 3.9. In addition to full-pitch windings, there are short-pitch and long-pitch windings. A distributed winding is when the q>1. Figure 3.10 shows distributed winding when q=2. Figures 3.11 and 3.12 show the difference between short-pitch and long-pitch winding.[10]

$$\tau = \frac{Q}{2 \cdot p} = m \cdot q \tag{3.25}$$

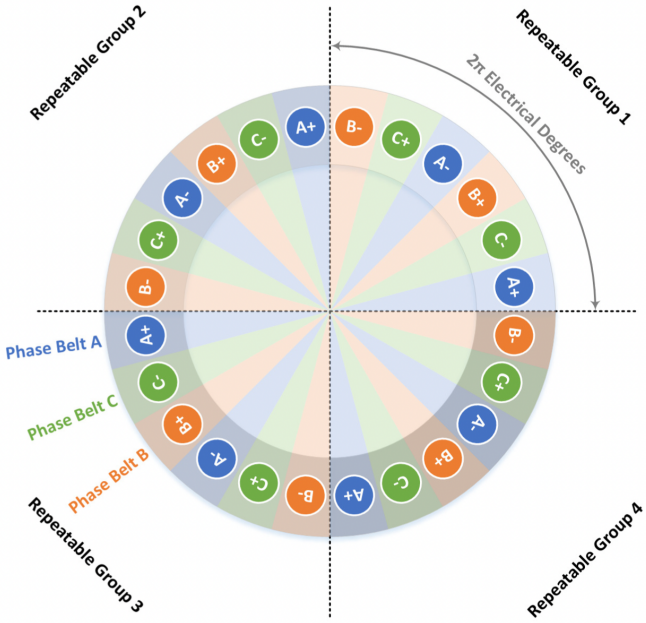

Figure 3.8: Illustration of slots, phase belts and repeatable groups with $m = 3$, $p = 4$, $q = 1$.[10]

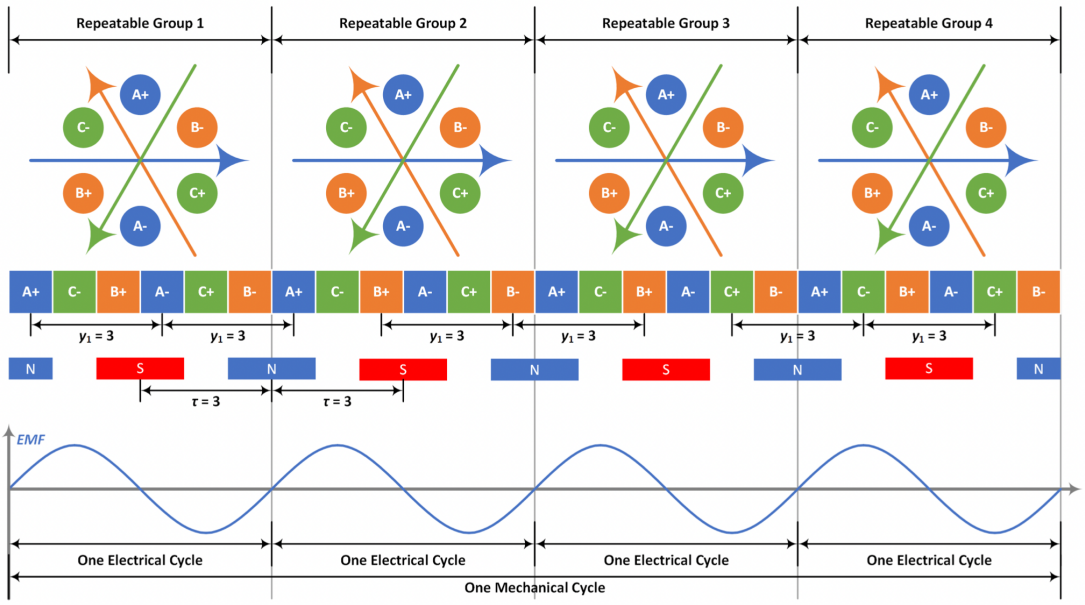

Figure 3.9: Illustration of Electrical and Mechanical cycles w.r.t repeatable groups with $m = 3$, $p = 4$, $q = 1$.[10]

Connection of the repeatable group can be connected as per machine output requirement. Table 3.2 and figure 3.13 shows one such example. The total $2p$ half-repeatable groups are therefore distributed into series branches and parallel branches. And this means that number of series branches N_{series} multiplying the number of parallel branches $N_{parallel}$ gives the total number of poles $2p$.[10]

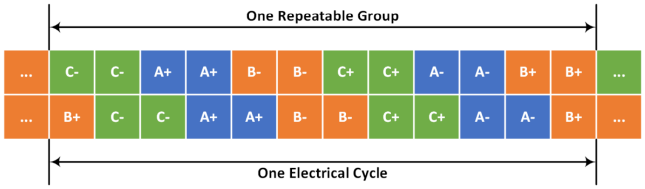

Figure 3.10: Star diagram for $m = 3$, $p = 4$, $q = 2$.[10]

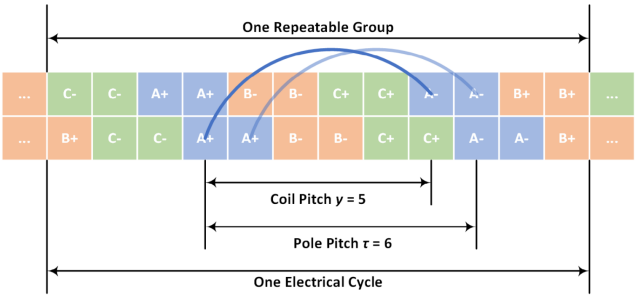

Figure 3.11: Star diagram for $m = 3$, $p = 4$, $q = 2$ and Short-pitch.[10]

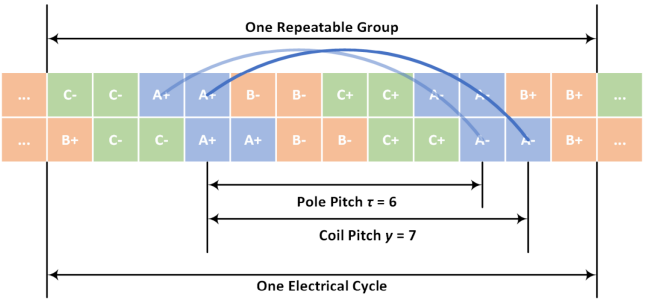

Figure 3.12: Star diagram for $m = 3$, $p = 4$, $q = 2$ and long-pitch.[10]

Table 3.2: Connections of repeatable groups to form the example machine output.[10]

N_{series}	$N_{parallel}$	Connection type
8	1	All-Series
4	2	Series and Parallel
2	4	Series and Parallel
1	8	All-Parallel

Figure 3.14 shows the vertical cross-sections of the stator of the PMSM that was manufactured as part of the project. Figure 3.15 shows the shape and dimension of the slots in the stator. These drawings were shared by the manufacturer.

3.1.4 Losses and efficiency

Losses in machines can be divided in to electrical and mechanical losses. Losses are important to be understood since they affect the temperature and lifetime of the machine. The total losses are constituted by the following:[10]

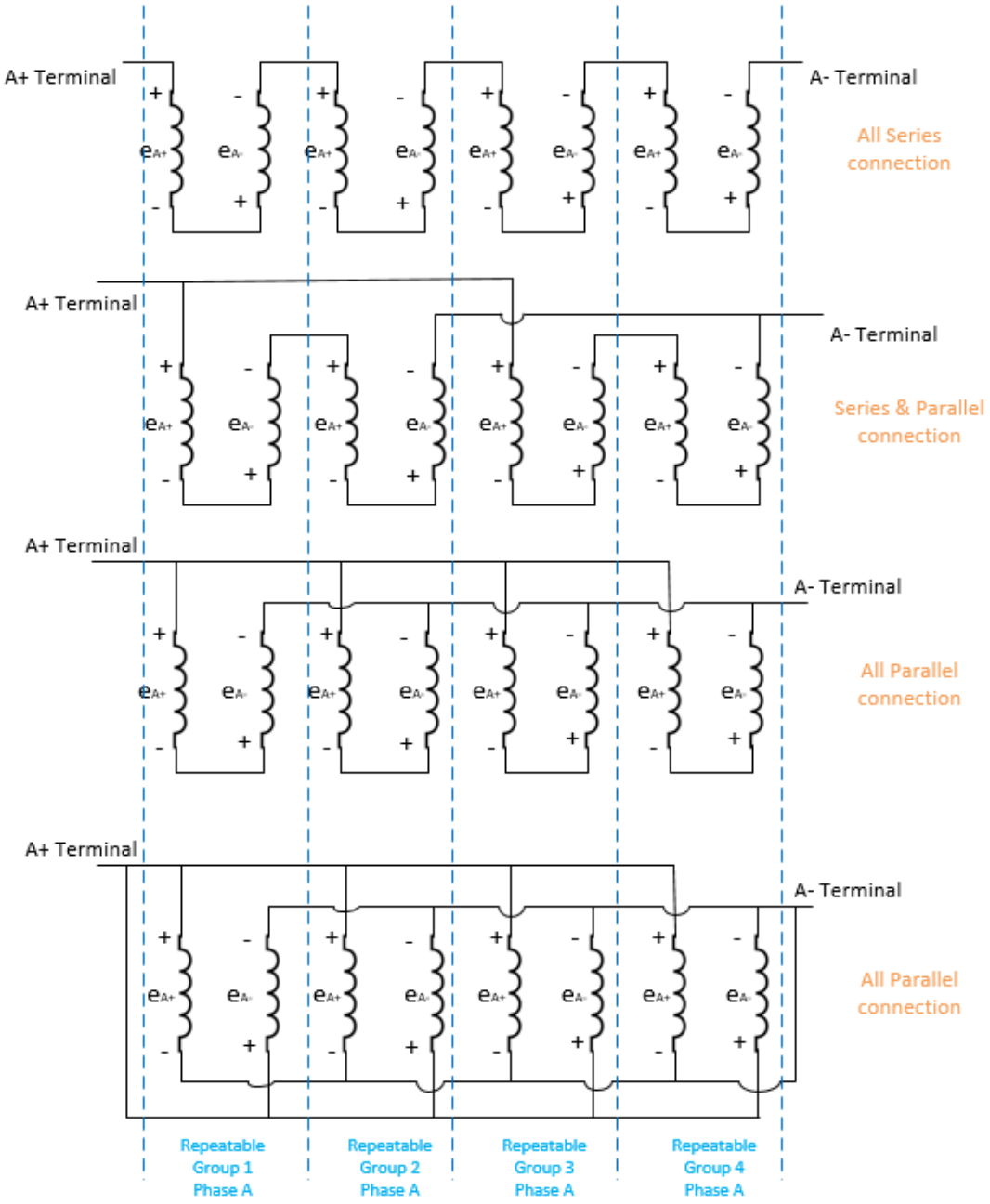

Figure 3.13: Connections as per table 3.2.

- Copper losses in the stator windings
- Iron losses in the core and all electromagnetic materials
- Frictional losses including mechanical losses in the air flow and bearings

3.1.4.1 Copper losses

The copper losses in the stator winding is given by the equation 3.26. Where, r_s is the phase resistance of the stator winding and I_s is the rms value of the stator phase current. For the PMSM in question in this thesis, the resistance was measured using LRC-meter and the values can be found in the table in the results section. These

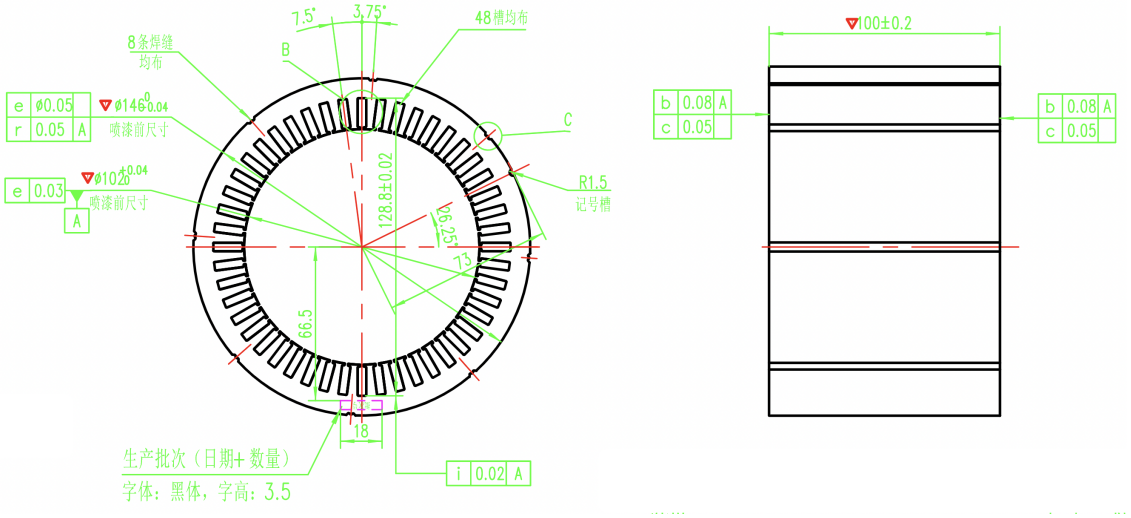

Figure 3.14: Vertical cross-sections of Stator of the PMSM to which the Propulsion system is designed in this thesis.

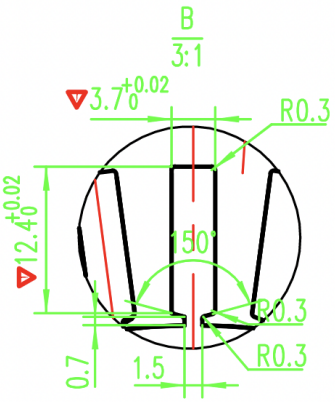

Figure 3.15: Slots of the stator

values are used as the parameters in the process model and also to calculate the total losses and its heat/temperature values for FEM simulations of the machine, POD system and its components'. When the windings of the stator are carrying AC current, it is affected by skin effect, proximity effect, and circulating currents. These losses should also be accounted for the total losses and can be again found out using FEM simulations.[10]

$$P_{Cu} = 3r_s I_s^2 \tag{3.26}$$

3.1.4.2 Iron losses

Iron loss in a PMSM is accounted by hysteresis losses, eddy current losses, and excess losses in the electric sheets (lamination). As we know, the hysterisis losses are the frictional losses when magnetic field changes the polarization direction in the magnetic field. The hysteresis losses depend on the material micro-structure and components properties. The eddy current losses are caused by the eddy cur-

rents induced in the lamination when the flux is alternating in the electromagnetic material. This can be avoided by building the core of the machine with stack of thin electric sheets. These sheets are sandwitched between insulation material. The thickness and conductivity of the electric sheets are the most important parameters for the eddy current losses. Excess losses are losses apart from the hysteresis and eddy current losses. These losses are usually low and are neglected.[10]

3.1.4.3 Efficiency

Efficiency of any machine is defined as the ratio of the output power to input power. The output power is the mechanical power out of the shaft and the input power is the electric power (real power and not the apparent power) into the stator terminals. The equation 3.27 holds good for efficiency calculation. Where, T is the Torque of the machine, Ω_{mech} is the speed of rotor's rotation, P_{fric} is the losses caused by airflow and bearing, and P_{Cu} is the copper loss of the machine and P_{Fe} is the iron loss of the machine.[10]

$$\eta = \frac{Output\,Power}{Input\,Power} = \frac{T\Omega_{mech} - P_{fric}}{T\Omega_{mech} + P_{Cu} + P_{Fe}} \tag{3.27}$$

3.2 DC/AC Inverter

Switch-mode DC/AC inverters are used in AC motor drives and uninterruptible AC power supplies to produce a sinusoidal AC output whose magnitude and frequency can both be varied. The switch-mode inverter is a converter through which the power flow is reversible. But mostly, the direction of power flow is from DC-side to the motor (AC-side). To slow down the AC motor, the kinetic energy of the motor and its load is recovered and the AC motor acts as a generator. During this time of braking, the power flows from the AC-side to the DC-side and the motor works as a generator and the inverter works in the rectifier mode. This power can either be dissipated through a resistor or can be stored in the battery system. In our case, this is not often. In this section we will concentrate on inverters with three-phase AC outputs. Since the DC voltage source is used, these inverters are referred to as voltage source inverters (VSIs). The VSIs can be further divided in to following categories.[13]

- Pulse-width-modulated inverters.
- Square-wave inverters.
- Single-phase inverters with voltage cancellation.

In PWM inverters, the input DC voltage is essentially constant in magnitude. Therefore, the inverter must control the magnitude and the frequency of the AC output voltages. This is achieved by PWM of the inverter switches and hence the name. There are various schemes to pulse-width modulate the inverter switches in order to shape the output AC voltages to be as close to a sine wave as possible. We will concentrate on sinusoidal PWM as this is used in the boat's propulsion system. Other types of VSIs are not discussed.[13]
Let us consider a single-phase inverter's block diagram as in figure 3.16 to understand

the different modes of operation. Here, the output voltage is filtered and v_0 is sinusoidal. Since the motor load is inductive, the current i_0 lags the voltage v_0 as shown in figure 3.17. The output waveforms show that during first interval, v_0, and i_0, are both positive, whereas during third interval, v_0, and i_0, are both negative. Therefore, during these intervals, the instantaneous power flow ($p_0 = v_0 i_0$) is from the DC-side to the AC-side, corresponding to an inverter mode of operation. In the other two intervals, v_0, and i_0 are of opposite sign and p_0 flows from AC-side to the DC-side corresponding to the rectifier mode of operation. Therefore, the switch mode inverter operates in all four quadrants of i_0-v_0 plane (figure 3.18) during each cycle of AC-output. Let us now describe about the a 3-phase inverter and aspects involved in it.[13]

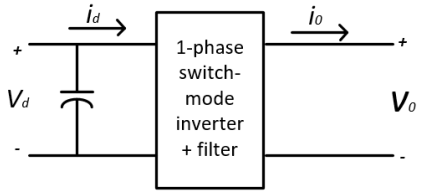

Figure 3.16: Block diagram representing a single phase rectifier.

3.2.1 Three Phase Inverter

In order to produce a sinusoidal output voltage waveform at a desired frequency, a sinusoidal control signal at the desired frequency is compared with a triangular waveform as shown in figure 3.19. The frequency of the triangular waveform (v_{tri}) determines the inverter switching frequency and is generally kept constant along with its amplitude $\hat{V}_{tri}$. The switching frequency of v_{tri} is carrier frequency (f_s). The control signal $v_{control}$ is used to modulate the switch duty ratio and has a frequency f_1, which is the desired fundamental frequency of the inverter voltage output. f_1 is called the modulating frequency. The inverter output voltage will not be a perfect sine wave and will contain voltage components at harmonic frequencies

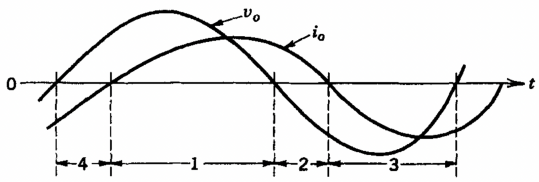

Figure 3.17: Output v_0 and i_0 waveforms.[13]

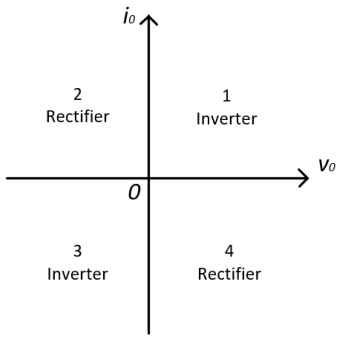

Figure 3.18: 4 quadrants of operation of a Single phase switch mode inverter.

of f_1. The modulation index is the ratio of the $\hat{V}_{control}$ to $\hat{V}_{tri}$ (eqn. 3.28). $\hat{V}_{tri}$ is usually kept constant. The frequency modulation ratio is defined as ratio of carrier frequency to modulating frequency (eqn. 3.29).[13]

$$m_a = \frac{\hat{V}_{control}}{\hat{V}_{tri}} \tag{3.28}$$

$$m_f = \frac{f_s}{f_1} \tag{3.29}$$

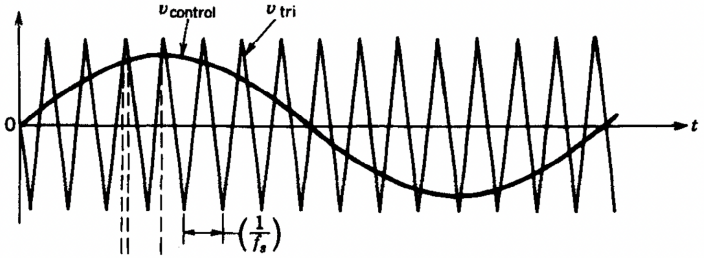

Figure 3.19: Waveforms showing $v_{control}$ and v_{tri}.[13]

To understand the switching pattern of the switches based on the carrier wave and the control signal, let us consider an one-leg switch mode inverter as in the figure 3.21. We assume that the midpoint of the DC-voltage available (this is not the case in most inverters) and the DC voltage is constant. In this inverter, when $v_{control} > v_{tri}$, T_{A+} is ON and $V_{A0} = V_d/2$. When $v_{control} < v_{tri}$, T_{A-} is ON and $V_{A0} = -V_d/2$. Since, the switches are never OFF at the same time, the V_{A0} fluctuates between $V_d/2$ and $-V_d/2$. V_{A0} and its fundamental frequency component (in dashed curve) are as in the figure 3.20.[13]

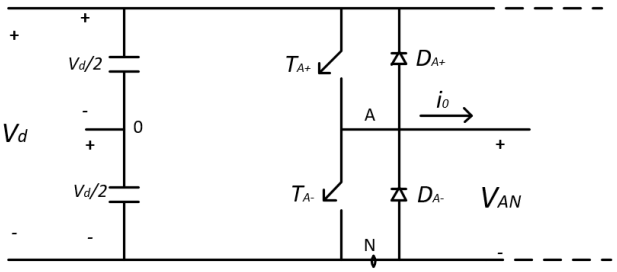

Figure 3.20: One-leg switch mode inverter.

The most frequently used three-phase inverter circuit consists of three legs, one for each phase, as shown in 3.22. This is the extension of the one-leg inverter discussed above. The output of each leg with respect to negative DC-bus, V_{An}, depends only on V_d and the switch status. The output voltage is independent of the output load current since one of the two switches in a leg is always ON at any instant. In three phase inverter, the triangular voltage waveform is compared with three sinusoidal

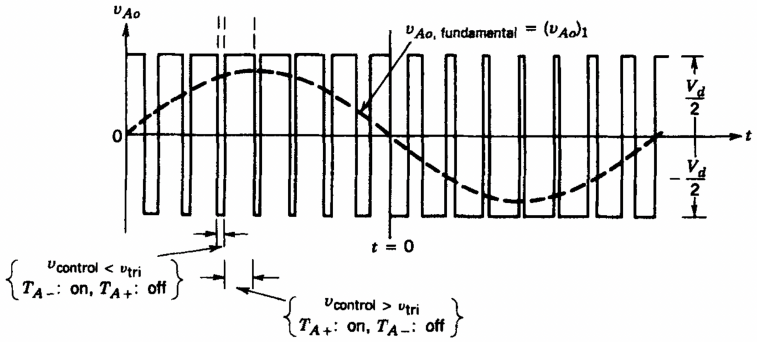

Figure 3.21: V_{A0} and Fundamental frequency as a result of switches T_{A+} and T_{A-} turning ON and OFF for one-leg switch mode inverter ($m_f = 15$ and $m_a = 0.8$).[13]

control voltages that are 120° out of phase as shown in the figure 3.23. The line-to-line voltages after similar DC-components getting cancelled out is seen in the figure 3.24.

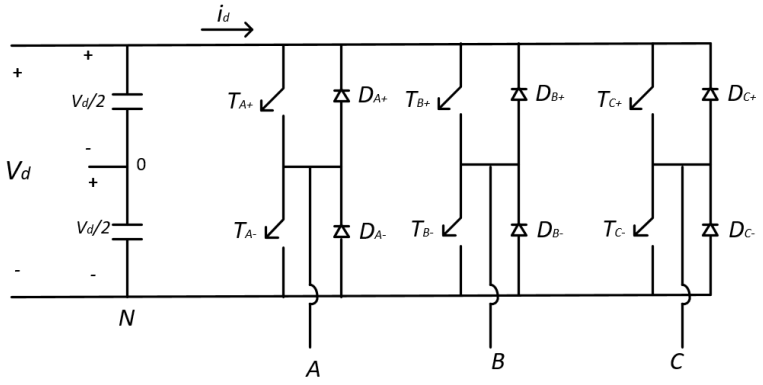

Figure 3.22: Three phase inverter circuit with three legs.

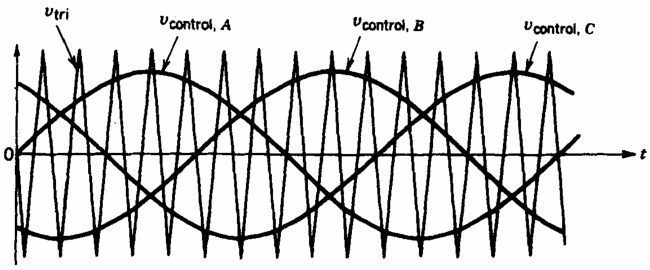

Figure 3.23: v_{tri} and three sinusoidal control voltages to obtain balanced three phase output voltages ($m_f = 15$). [13]

In the three-phase inverters, only the harmonics in the line-to-line voltages are of concern. The harmonics in the output of any one of the legs (V_{AN}) are identical to the harmonics in V_{A0} (figure 3.25). Only the odd harmonics exist as sidebands which are centered around m_f and its multiples when m_f is odd. Only considering the harmonic at m_f (the same applies to its odd multiples), the phase difference between the m_f harmonic in V_{AN} and V_{BN} is $(120 \cdot m_f)°$. This phase difference will

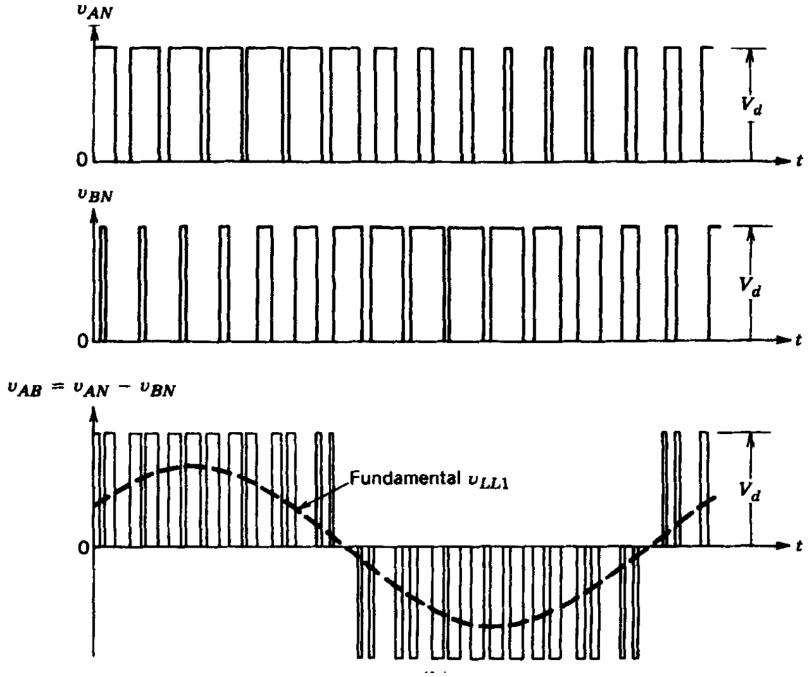

Figure 3.24: Line voltage V_{AB} waveform. [13]

be equivalent to zero (a multiple of 360°) if m_f is odd and a multiple of 3. As a consequence, the harmonic at m_f is suppressed in the line-to-line voltage V_{AB}. The same argument applies in the suppression of harmonics at the odd multiples of m_f if m_f is chosen to be an odd multiple of 3 (the reason for choosing m_f to be an odd multiple of 3 is to keep m_f odd and, hence, eliminate even harmonics). Thus, some of the dominant harmonics in the one-leg inverter can be eliminated from the line-to-line voltage of a three-phase inverter.[13]
The following PWM considerations are to be made:

- A synchronised PWM must be used with m_f being odd integer for low values of m_f and to eliminate even harmonics.
- For AC motor load applications, asynchronous PWM should be avoided.
- During overmodulation ($m_a > 1$), regardless of the value of m_f, the conditions pertinent to a small m_f should be observed.

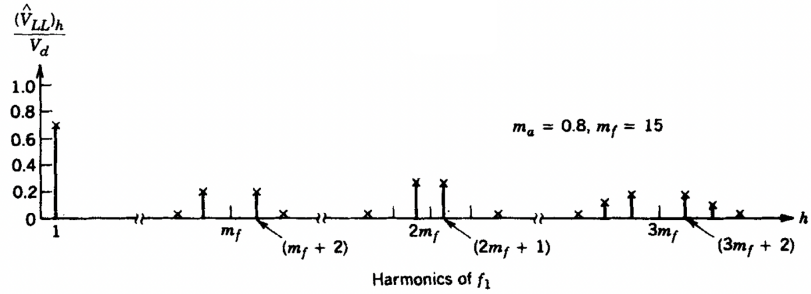

Figure 3.25: Three phase inverter harmonic spectrum. [13]

For Linear Modulation ($m_f \leq 1.0$), the peak value of the fundamental frequency component in one of the inverter legs is given by the equation 3.30. The line-to-line

RMS voltage at the fundamental frequency, due to 120° phase displacement between phase voltages, can be written as in the equation 3.31. The case of over-modulation is not studied here.[13]

$$(\hat{V}_{AN})_1 = m_a \frac{V_d}{2} \tag{3.30}$$

$$\begin{aligned} V_{LL1} &= \frac{\sqrt{3}}{\sqrt{2}}(\hat{V}_{AN})_1 \\ &= \frac{\sqrt{3}}{2\sqrt{2}} m_a V_d \\ &\simeq 0.612 m_a V_d \end{aligned} \tag{3.31}$$

In practice, because of the finite turn-OFF and turn-ON times associated with any type of switch, a switch is turned OFF at the switching time instant. However, the turn-ON of the other switch in that inverter leg is delayed by a blanking time t_Δ as shown in the figure 3.26. This is conservatively chosen to avoid a "shoot through" or cross-conduction current through the leg. This is usually microseconds for MOSFETs and larger for slower switching devices. For higher switching frequencies, faster switching devices that allow blanking time to be small should be used. Figure 3.27 shows average output voltage $V_0(t)$ and the load current i_o which is lagging for a single phase PWM inverter. The distortion in $V_0(t)$ at the current zero crossings due to blanking time results in low order harmonics such as third, fifth, seventh, and so on, of the fundamental frequency in the inverter output. Similar distortions can be seen in line-to-line voltage in a three phase PWM inverter, where the low-order harmonics are of the order $6m \pm 1$ (m = 1, 2, 3, ...) of the fundamental frequency.[13]
The switches used in our inverter are Insulated Gate Bipolar Transistors (IGBT). They have some advantages of the MOSFET, the GTO, and the BJT combined. It requires small amount of energy to switch the device. The IGBT has a small ON-state voltage even in devices with large blocking voltage ratings. It can be designed to block negative voltages. IGBTs have turn-ON and turn-OFF times on the order of $10^{-6}s$.[13]
For the boat's propulsion, infeneon's $HybridPACK^{TM}DC6$ module which has IGBT switches is used. This is mainly designed for automotive applications and is currently being used in hybrid and electric buses. Its main features include low switching losses, high junction operating temperature, high thermal and power cycling capability, high reliability for mild hybrid inverter and generator applications, and high mechanical robustness. The driver stage PCB can be soldered on top of the module. The driver stage PCB contains driver and snubber circuits, inout and output capacitors, inductors and power supply units that are required for the module to function. Figure 3.28 and 3.29 shows the $HybridPACK^{TM}DC6$ module and the driver PCB. Figure 3.30 shows the pins and the corresponding description on the Q driver PCB. We can see that the PCB requires 6 PWM signals each for 6 IGBT switches, 5V DC and Ground supply, 15V DC (VCC) and ground. The PCB measures the three phase currents (IW, IV and IU) and trips for over-current protection.

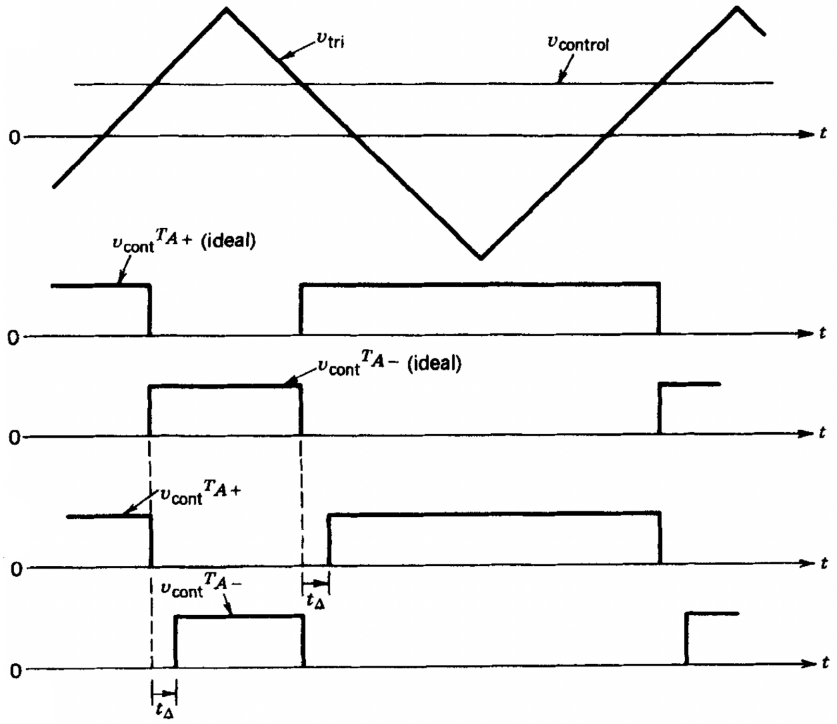

Figure 3.26: Waveforms showing ideal switching and with blanking time. [13]

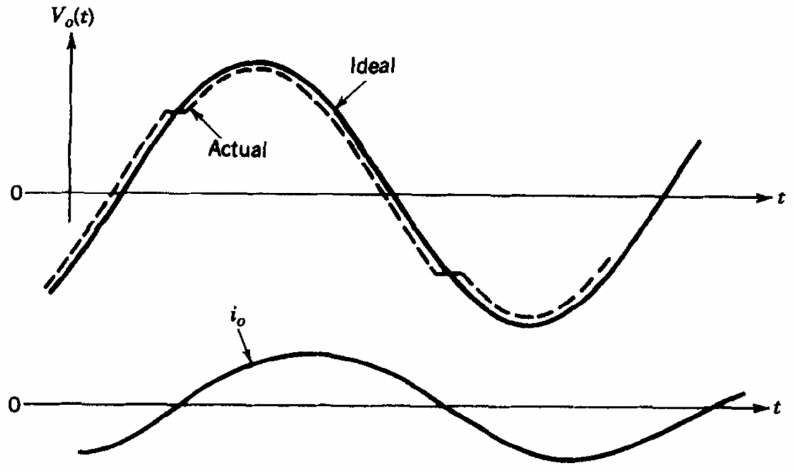

Figure 3.27: Effect of Blanking time on the sinusoidal input in a single phase PWM inverter. [13]

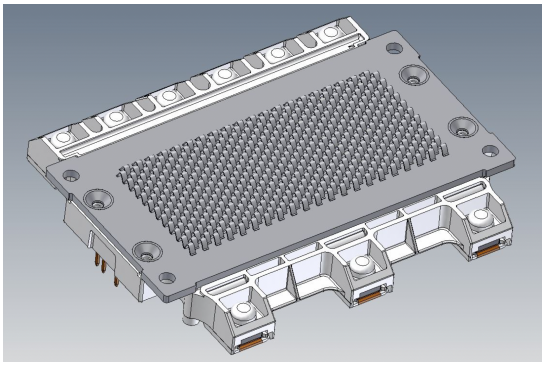

Figure 3.28: $HybridPACK^{TM}DC6$. Source: Infineon - $HybridPACK^{TM}DC6$ module manual

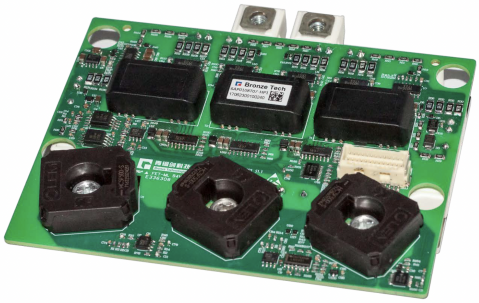

Figure 3.29: Module with the driver PCB. Source: Bronze technologies user manual.

Pin number	Description	Pin number	Description
1	GNDA	14	Sfault_res
2	GNDA	15	IPM_E2
3	AD_IW	16	IPM_E1
4	UDC	17	5V_GND
5	AD_IV	18	5V_GND
6	R_Temp	19	5V+
7	AD_IU	20	5V+
8	PWM_WB	21	GND
9	PWM_WT	22	VCC
10	PWM_VB	23	GND
11	PWM_VT	24	VCC
12	PWM_UB	25	GND
13	PWM_UT	26	VCC

Figure 3.30: Pins on driver PCB and their description. Source: Bronze technologies user manual.

4

Controller design for a PMSM

In this chapter we will see how dynamic modeling of a PMSM is done and the aspects involved int it.

4.1 Modeling a PMSM

The following assumptions are made while modeling and designing a controller.

- No zero-sequence component in the three-phase quantities.
- Sinusoidal distribution of the stator windings.
- Linear magnetization characteristics.
- No losses in the iron.
- Resistances independent of temperature and frequency.

4.1.1 Flux linkage in a PMSM

The flux linkages are given by the equations below. These equations are result of insertion of self and mutual inductance equations (obtained by approximating due to saliency) in the flux linkages for the 3-phases. 3-phase model can be used for simulation purpose but it may not be a suitable model for control derivation purpose. Hence the model is derived in the rotor frame so that the control can be achieved by calculating the reference DC currents.

$$\Psi_a = (L_{aa0} + L_{ab0} + \frac{3}{2}L_{aa2}\cos(2\phi_r))i_a + \frac{\sqrt{3}}{2}L_{aa2}\sin(2\phi_r)(i_b - i_c) + \Psi_m\cos(\phi_r)$$

$$\Psi_b = (L_{aa0} + L_{ab0} + \frac{3}{2}L_{aa2}\cos(2(\phi_r - 120)))i_b + \frac{\sqrt{3}}{2}L_{aa2}\sin(2(\phi_r - 120))(i_c - i_a) + \Psi_m\cos(\phi_r - 120)$$

$$\Psi_c = (L_{aa0} + L_{ab0} + \frac{3}{2}L_{aa2}\cos(2(\phi_r + 120)))i_a + \frac{\sqrt{3}}{2}L_{aa2}\sin(2(\phi_r + 120))(i_a - i_b) + \Psi_m\cos(\phi_r + 120)$$

4.1.2 Space Vectors and Alpha-Beta Coordinates

In order to illustrate the relationship between different quantities in electric machines, space vectors are defined. The idea of Space Vector is to convert all the electric and magnetic quantities into rotating vectors in space. In a three phase

system, the flux is rotating and it cannot be fully described by a scalar. In order to describe the direction of the flux, the flux needs to be expressed by a vector instead of a scalar as in the equation 4.1. Since the stator winding arrangement of an electric machine is repeated from one pole pair to another, in the analysis of electric machines, the space vector is drawn in one pole-pair, i.e. 360 electrical degrees. The inductance L should be a scalar, and the direction of the current vector $\vec{i}$ is therefore defined by the direction of flux linkage $\vec{\Psi}$, and the direction of the flux linkage $\vec{\Psi}$ is defined as the location where the peak of the flux occurs.

$$\vec{\Psi} = L\vec{i} \tag{4.1}$$

Accordingly, in order to express a vector in a 2D plane, coordinates are necessary to be applied. An α-axis is defined as aligned with a-axis, whereas a β-axis is defined as leading α-axis by 90 degrees as shown in the figure 4.1.

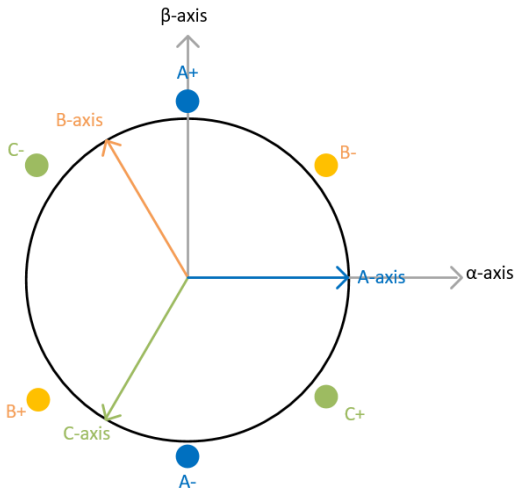

Figure 4.1: abc and $\alpha\beta$ co-ordinate system.

In the complex format, the relationship can be expressed as in the equation 4.2

$$\Psi_\alpha + j\Psi_\beta = \vec{\Psi} = L\vec{i} = L(i_\alpha + ji_\beta) \tag{4.2}$$

Thereafter, in order for voltage equation to make sense, voltage vector is defined as well, in a synchronous generator as (eq. 4.3)

$$\vec{u_s} = \vec{i_s} \cdot R_s + \omega \cdot \vec{\Psi_s} \tag{4.3}$$

The quantities are expressed in space vectors by two coordinates, α and β. However, the three-phase currents and voltages are in abc in reality. The following transformation can be used to convert the 2-phase to 3-phase and vice-versa. This transformation is called Clarke's transformation (Eqn. 4.4 and 4.5). If there is no zero-sequence, no information is lost when transforming from three-phase to two-phase.

$$\begin{bmatrix} S_\alpha \\ S_\beta \end{bmatrix} = K \begin{bmatrix} \frac{2}{3} & -\frac{1}{3} & -\frac{1}{3} \\ 0 & \frac{1}{\sqrt{3}} & -\frac{1}{\sqrt{3}} \end{bmatrix} \begin{bmatrix} S_a \\ S_b \\ S_c \end{bmatrix} \tag{4.4}$$

$$\begin{bmatrix} S_a \\ S_b \\ S_c \end{bmatrix} = \frac{1}{K} \begin{bmatrix} 1 & 0 \\ -\frac{1}{2} & \frac{\sqrt{3}}{2} \\ -\frac{1}{2} & -\frac{\sqrt{3}}{2} \end{bmatrix} \begin{bmatrix} S_\alpha \\ S_\beta \end{bmatrix} \tag{4.5}$$

The instantaneous active and reactive power can be derived as in equations below.

$$\begin{aligned} p(t) = (u_a(t)i_a(t) + u_b(t)i_b(t) + u_c(t)i_c(t)) &= \frac{3}{2K^2}(u_\alpha(t)i_\alpha(t) + u_\beta(t)i_\beta(t)) \\ &= \frac{3}{2K^2} Re[\vec{u^s}\vec{i^{s*}}] \\ q(t) = \frac{1}{\sqrt{3}}(u_a(t)(i_c(t) - i_b(t)) + u_b(t)(i_a(t) - i_c(t)) + u_c(t)(i_b(t) - i_a(t))) \\ = \frac{3}{2K^2}(u_\beta(t)i_\alpha(t) - u_\alpha(t)i_\beta(t)) &= \frac{3}{2K^2} Im[\vec{u^s}\vec{i^s}*] \\ P = Avg[p(t)] \\ Q = Avg[q(t)] \end{aligned}$$

The scaling constant K can be selected arbitrarily. For amplitude invariant scaling, we choose $K = 1$. The space vectors can be moved between stationary and rotating form (eqns. 4.6 and 4.7). For a random xy-system, θ can be arbitrarily selected. For a dq system, rotor flux is oriented in x-direction (d-direction).

$$\vec{u}^{xy} = \vec{u}^s e^{-j\theta} \text{ (\textbf{Stationary to Rotating})} \tag{4.6}$$

$$\vec{u}^s = \vec{u}^{xy} e^{j\theta} \text{ (\textbf{Rotating to Stationary})} \tag{4.7}$$

The 3-phase model can be transformed to $\alpha\beta$ model as in figure 4.2 by neglecting the zero sequence and using amplitude invariant transformation.

$$\underline{u}_s^s = u_{s\alpha} + j u_{s\beta} = \frac{2}{3}\left(u_a + u_b e^{j\frac{2\pi}{3}} + u_c e^{j\frac{4\pi}{3}}\right) = \frac{2}{3}\left(\underbrace{R_a i_a + \frac{d\psi_a}{dt}}_{u_a} + \underbrace{\left(R_b i_b + \frac{d\psi_b}{dt}\right)}_{u_b} e^{j\frac{2\pi}{3}} + \underbrace{\left(R_c i_c + \frac{d\psi_c}{dt}\right)}_{u_c} e^{j\frac{4\pi}{3}}\right) =$$

$$= R_s \underbrace{\frac{2}{3}\left(i_a + i_b e^{j\frac{2\pi}{3}} + i_c e^{j\frac{4\pi}{3}}\right)}_{\underline{i}_s^s} + \frac{d}{dt}\underbrace{\left(\frac{2}{3}\left(\psi_a + \psi_b e^{j\frac{2\pi}{3}} + \psi_c e^{j\frac{4\pi}{3}}\right)\right)}_{\underline{\psi}_s^s} = R_s \underline{i}_s^s + \frac{d\underline{\psi}_s^s}{dt}$$

Figure 4.2: abc to $\alpha\beta$ transformation of the Voltage space vector.[6]

Using the equations describing the flux linkages for three phases described before, each part of the transformation of the stator flux linkage can be done as in the figure

$$\underline{\psi}^s_{s,1} = \frac{2}{3}\left((L_{aa0} + L_{ab0}) i_a + (L_{aa0} + L_{ab0}) i_b e^{j\frac{2\pi}{3}} + (L_{aa0} + L_{ab0}) i_c e^{j\frac{4\pi}{3}} \right) = (L_{aa0} + L_{ab0}) \underline{i}^s_s$$

$$\underline{\psi}^s_{s,2} = \frac{2}{3}\left(\frac{3}{2} L_{aa2} \cos(2\phi_r) i_a + \frac{3}{2} L_{aa2} \cos\left(2(\phi_r - 120^\circ)\right) i_b e^{j\frac{2\pi}{3}} + \frac{3}{2} L_{aa2} \cos\left(2(\phi_r + 120^\circ)\right) i_c e^{j\frac{4\pi}{3}} \right) =$$

$$= \frac{3}{4} L_{aa2} e^{j2\phi_r} \frac{2}{3}\left(i_a + i_b e^{-j\frac{2\pi}{3}} + i_c e^{j\frac{2\pi}{3}} \right) = \frac{3}{4} L_{aa2} e^{j2\phi_r} \underline{i}^{s*}_s$$

$$\underline{\psi}^s_{s,3} = \frac{2}{3}\left(\frac{\sqrt{3}}{2} L_{aa2} \sin(2\phi_r)(i_b - i_c) + \frac{\sqrt{3}}{2} L_{aa2} \sin\left(2(\phi_r - 120^\circ)\right)(i_c - i_a) e^{j\frac{2\pi}{3}} + \frac{\sqrt{3}}{2} L_{aa2} \sin\left(2(\phi_r + 120^\circ)\right)(i_a - i_b) e^{j\frac{4\pi}{3}} \right) =$$

$$= L_{aa2} e^{j2\phi_r} \underbrace{\frac{\sqrt{3}}{2} \frac{e^{j\frac{2\pi}{3}} - e^{-j\frac{2\pi}{3}}}{2j}}_{\sin\left(\frac{2\pi}{3}\right) = \frac{\sqrt{3}}{2}} \underline{i}^{s*}_s = \frac{3}{4} L_{aa2} e^{j2\phi_r} \underline{i}^{s*}_s$$

$$\underline{\psi}^s_{s,4} = \frac{2}{3}\left(\Psi_m \cos(\phi_r) + \Psi_m \cos\left(\phi_r - 120^\circ\right) e^{j\frac{2\pi}{3}} + \Psi_m \cos\left(\phi_r + 120^\circ\right) e^{j\frac{4\pi}{3}} \right) = \frac{2}{3}\frac{3}{2} \Psi_m e^{j\phi_r} = \Psi_m e^{j\phi_r}$$

Figure 4.3: Separating each part of the transformation of the stator flux linkage.[6]

$$\underline{u}^s_s = R_s \underline{i}^s_s + \frac{d\underline{\psi}^s_s}{dt}$$

$$\underline{\psi}^s_s = \underline{\psi}^s_{s,1} + \underline{\psi}^s_{s,2} + \underline{\psi}^s_{s,3} + \underline{\psi}^s_{s,4} =$$

$$= (L_{aa0} + L_{ab0}) \underline{i}^s_s + \frac{3}{2} L_{aa2} e^{j2\phi_r} \underline{i}^{s*}_s + \Psi_m e^{j\phi_r}$$

$$\underline{\psi}^s_s = \text{"} \underline{L}_s \underline{i}^s_s \text{"} + \Psi_m e^{j\phi_r}$$

Figure 4.4: Voltage and Total flux linkage vectors in $\alpha\beta$ system. Ψ_m is the magnet flux linkage, L_s accounts for leakage and mutual inductance. [6]

4.3. Thus, the voltage and flux linkage vectors is of the form of equations in figure 4.4.

Now, the vectors should be moved from $\alpha\beta$ system to a rotating system (rotor reference) by using the equation 4.6. The θ is chosen to be in the direction of rotor flux direction (d-direction). Thus, the transformed system is called dq system. Any other coordinate system (xy-frame) may result in a more complex model than the dq-model. The stationary to rotating system can be seen in the figure 4.5. The θ used to move to dq co-ordinates is called the dq-transformation angle. So, for a perfect field orientation $\phi_r = \theta_r$ (figure 4.6).

The torque can be derived from the electric power equation as shown in the figure 4.7. Since we're using the amplitude invariant scaling, K=1.

Thus, equivalent circuit model of the PMSM in dq co-ordinate system, voltages and mechanical equations are as in the figure 4.8. Where, n_p is the number of pole-pairs, Φ_r is the mechanical rotor position, ϕ_r is the electrical rotor position, Ω_r is the mechanical rotor speed, ω_r is the electrical rotor speed, T_e is the electrodynamical torque, T_l is the load torque, J is the inertia of the machine, i_{sd} and i_{sq} are the d and

Stator voltage equation in stationary form:

electrical rotor angle

$$\underline{\psi}_s^s = (L_{aa0} + L_{ab0})\underline{i}_s^s + \frac{3}{2}L_{aa2}e^{j2\phi_r}\underline{i}_s^{s*} + \Psi_m e^{j\phi_r}$$

$$\underline{u}_s^s = R_s\underline{i}_s^s + \frac{d\underline{\psi}_s^s}{dt}$$

Gives in rotating coordinates:

$$\underline{u}_s e^{j\theta_r} = R_s\underline{i}_s e^{j\theta_r} + \frac{d\underline{\psi}_s}{dt}e^{j\theta_r} + j\omega_r\underline{\psi}_s e^{j\theta_r}$$

$$\underline{\psi}_s^s = \underline{\psi}_s e^{j\theta_r} = (L_{aa0} + L_{ab0})\underline{i}_s e^{j\theta_r} + \frac{3}{2}L_{aa2}e^{j2\phi_r}\left(\underline{i}_s e^{j\theta_r}\right)^* + \Psi_m e^{j\phi_r} \quad \Rightarrow$$

$$\underline{\psi}_s = (L_{aa0} + L_{ab0})\underline{i}_s + \frac{3}{2}L_{aa2}e^{j(2\phi_r - 2\theta_r)}\underline{i}_s^* + \Psi_m e^{j(\phi_r - \theta_r)}$$

Figure 4.5: $\alpha\beta$ system to dq-representation.[6]

$$\underline{u}_s = R_s\underline{i}_s + \frac{d\underline{\psi}_s}{dt} + j\omega_r\underline{\psi}_s$$

$$\underline{\psi}_s = (L_{aa0} + L_{ab0})\underline{i}_s + \frac{3}{2}L_{aa2}\underbrace{e^{j(2\phi_r - 2\theta_r)}}_{=1}\underline{i}_s^* + \Psi_m\underbrace{e^{j(\phi_r - \theta_r)}}_{=1} \quad \Rightarrow$$

$$\underline{\psi}_s = \underbrace{\left(L_{aa0} + L_{ab0} + \frac{3}{2}L_{aa2}\right)}_{L_{sd}}\underline{i}_{sd} + j\underbrace{\left(L_{aa0} + L_{ab0} - \frac{3}{2}L_{aa2}\right)}_{L_{sq}}\underline{i}_{sq} + \Psi_m = L_{sd}\underline{i}_{sd} + jL_{sq}\underline{i}_{sq} + \Psi_m$$

$$u_{sd} = R_s i_{sd} + L_{sd}\frac{di_{sd}}{dt} - \omega_r L_{sq} i_{sq}$$

$$u_{sq} = R_s i_{sq} + L_{sq}\frac{di_{sq}}{dt} + \omega_r L_{sd} i_{sd} + \omega_r \Psi_m$$

Figure 4.6: dq voltages and inductances for perfect field orientation $\phi_r = \theta_r$.[6]

Shaft power:

$$P_e = \frac{3}{2K^2}\mathrm{Re}\left\{j\omega_r\underline{\psi}_s\underline{i}_s^*\right\} = \left[\mathrm{Re}\{j\underline{z}\} = -\mathrm{Im}\{\underline{z}\}\right] = -\frac{3\omega_r}{2K^2}\mathrm{Im}\left\{\underline{\psi}_s\underline{i}_s^*\right\} = \frac{3\omega_r}{2K^2}\mathrm{Im}\left\{\underline{\psi}_s^*\underline{i}_s\right\}$$

Torque:

$$T_e = \frac{P_e}{\Omega_r} = \frac{n_p P_e}{\omega_r} = \frac{3\omega_r n_p}{2\omega_r K^2}\mathrm{Im}\left\{\underline{\psi}_s^{s*}\underline{i}_s^s\right\} = \frac{3n_p}{2K^2}\mathrm{Im}\left\{\underline{\psi}_s^{s*}\underline{i}_s^s\right\} =$$

$$= \frac{3n_p}{2K^2}\mathrm{Im}\left\{\left(L_{sd}i_{sd} + jL_{sq}i_{sq} + \Psi_m\right)^*\underline{i}_s\right\} = \frac{3n_p}{2K^2}\mathrm{Im}\left\{\left(L_{sd}i_{sd} - jL_{sq}i_{sq}\right)\left(i_{sd} + ji_{sq}\right) + \Psi_m\underline{i}_s\right\} =$$

$$= \frac{3n_p}{2K^2}\left(L_{sd}i_{sd}i_{sq} - L_{sq}i_{sq}i_{sd} + \Psi_m i_{sq}\right) = \frac{3n_p}{2K^2}\left(\Psi_m i_{sq} + \left(L_{sd} - L_{sq}\right)i_{sd}i_{sq}\right)$$

Figure 4.7: Electrical Torque from the Electrical power derivation with K=1.[6].

q currents (equivalently flux and torque currents), L_{sd} and L_{sq} are the equivalent d and q inductances, u_{sd} and u_{sq} are the d and q voltages, R_s is the equivalent series resistance, and Ψ_m is the magnetic flux linkage.

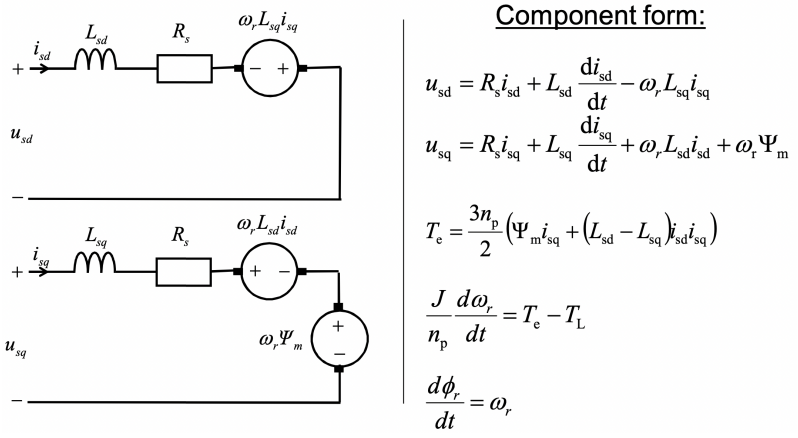

Figure 4.8: Equivalent circuit model of the PMSM in dq co-ordinate system, voltages and mechanical equations.[6]

4.1.3 Process model

Now we have the PMSM's electromechanical equations. This can be used to develop the process model. The controller is implemented in the dq-frame so that currents and voltages are DC-values and we know how to design controllers for the DC-machine. d and q currents for the process model are derived from the equations for d and q voltages (figure 4.9). The system for the current regulator with the blocks looks as in the figure 4.10.

$$i_{sd} = \frac{1}{L_{sd}s + R_s}(u_{sd} + \omega_r L_{sq} i_{sq})$$
$$i_{sq} = \frac{1}{L_{sq}s + R_s}(u_{sq} - \omega_r L_{sd} i_{sd} - \omega_r \Psi_m)$$

Figure 4.9: d and q currents for the process model

This model is not suitable for controller derivation. It will be convenient if $\omega_r L_{sq} i_{sq}$ and $\omega_r L_{sd} i_{sd}$ and $\omega_r \Psi_m$ are compensated using the estimated values. The inductances are the estimated values as it changes. The changes in resistance due to change in temperature is neglected here. In order to reduce the disturbance from the back-emf, active damping is implemented. The block is as in the figure 4.11 with the feed-forward and active damping. With the perfect feed-forward, the controller sees the process equations as in figure 4.12.

4.2 Controller design

This section describes how the current, speed and position controllers are designed and the aspects involved in it.

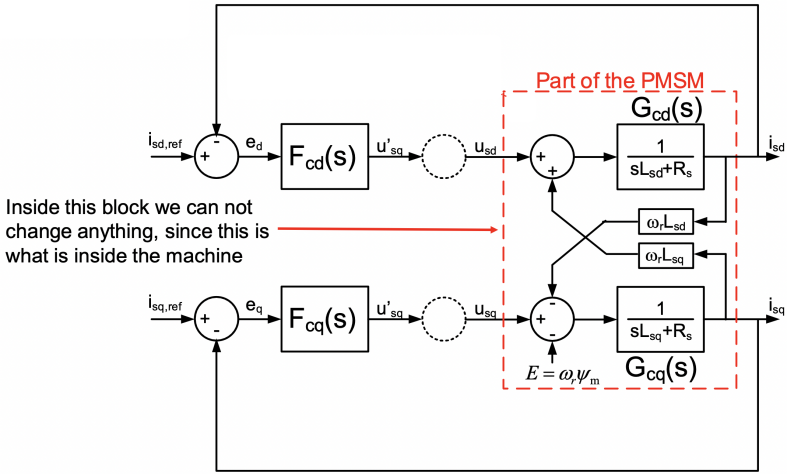

Figure 4.10: The system for the current regulator.[6]

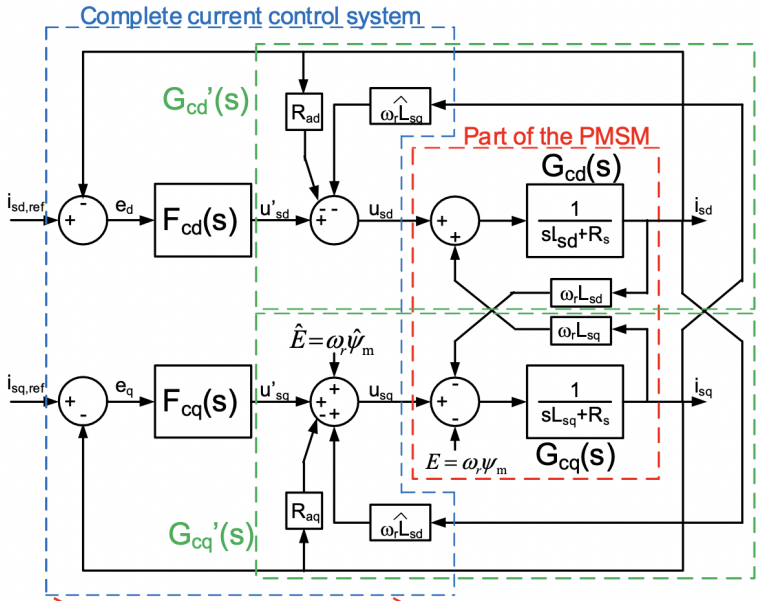

Figure 4.11: The system for the current regulator with perfect feed-forward terms.[6]

$$i_{sd} = \frac{1}{L_{sd}s + R_s + R_{ad}} u'_{sd} = G'_{cd}(s)u'_{sd}$$
$$i_{sq} = \frac{1}{L_{sq}s + R_s + R_{aq}} u'_{sq} = G'_{cq}(s)u'_{sq}$$

Figure 4.12: Process equations

4.2.1 Current Controller according to IMC

Now with the process model, regulator parameters are to be determined. This can be achieved by making the closed loop system $G_{cl}(s)$ to be first order low pass filter. The Step response of close-loop system for various rise times is as in the figure 4.14. Equations 4.8 to 4.10 shows how to derive the regulator parameters by making the close-loop system a first order low pass filter.

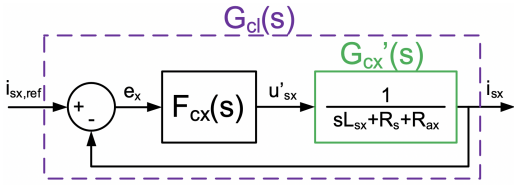

Figure 4.13: Close-loop system.[6]

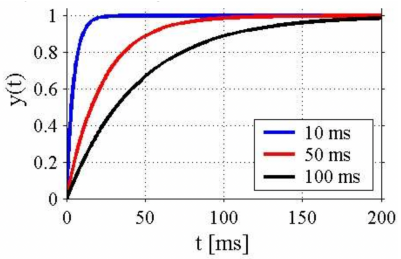

Figure 4.14: Step response of a close-loop system.[6]

$$G_{cl}(s) = \frac{i_{sx}}{i_{sx,ref}} = \frac{\alpha_c/s}{1+\alpha_c/s} = \frac{F_{cx}(s)G'_{cx}(s)}{1+F_{cx}(s)G'_{cx}(s)} \tag{4.8}$$

$$\textbf{IMC} \implies F_{cx}(s) = \frac{\alpha_c}{s}{G'_{cx}}^{-1}(s) = \frac{\alpha_c}{s}(s\hat{L}_{sx} + \hat{R}_s + R_{ax}) = \alpha_c\hat{L}_{sx} + \frac{\alpha_c(\hat{R}_s + R_{ax})}{s} \tag{4.9}$$

$$F_{cx}(s) = k_{pcx} + \frac{k_{icx}}{s} \tag{4.10}$$

We want $G'_{cx}(s)$ to have the same bandwidth as the current regulator. Using this, the parameters can be found using the equations 4.12 to 4.14. Where, g is the gain.

$$G'_{cx}(s) = \frac{1}{\hat{L}_{sx} + \hat{R}_s + R_{ax}} = \frac{1/\hat{L}_{sx}}{s + (\hat{R}_s + R_{ax})/\hat{L}_{sx}} = \frac{g\alpha_c}{s+\alpha_c} \tag{4.11}$$

$$R_{ax} = \alpha_c\hat{L}_{sx} - \hat{R}_s \tag{4.12}$$

$$k_{pcx} = \alpha_c\hat{L}_{sx} \tag{4.13}$$

$$k_{icx} = \alpha_c(\hat{R}_s + R_{ax}) \tag{4.14}$$

4.2.2 Maximum Torque Per Ampere (MTPA), Current and Voltage limit

As discussed, the losses in a PMSM is accounted by Copper loss in the stator winding and Iron losses in the stator core. The iron loss is negligible at low frequencies (low speeds) and is dominated by copper loss. The copper loss is given by the equation 4.15. It is obvious that at low frequencies, the stator current determines the total loss of the PMSM. MTPA is a method for the motor to generate maximum torque with a given stator current.[10]

$$P_{cu} = \frac{3}{2}r_s|i_s|^2 \tag{4.15}$$

We know that the stator current can be expressed in terms of d and q currents as in the equations 4.16 through 4.19. Where, θ is the current angle.[10]

$$i_d = i_s \cos\theta \tag{4.16}$$
$$i_q = i_s \sin\theta \tag{4.17}$$
$$\sqrt{i_d^2 + i_q^2} = i_s \tag{4.18}$$

If the maximum stator current is $i_{s,max}$, then i_d and i_q can be selected within the circle obtained by the equation 4.19.[10]

$$\sqrt{i_d^2 + i_q^2} \leq i_{s,max} \tag{4.19}$$

With $L_{sd} < L_{sq}$, the electrodynamical torque can be plotted with respect to currents. From equation 4.19 the maximum current is demonstrated graphically in the dq-plane as in figure 4.15, where it can be seen that $i_{s,max}$ takes the shape of a circle with a center in origin.[10]

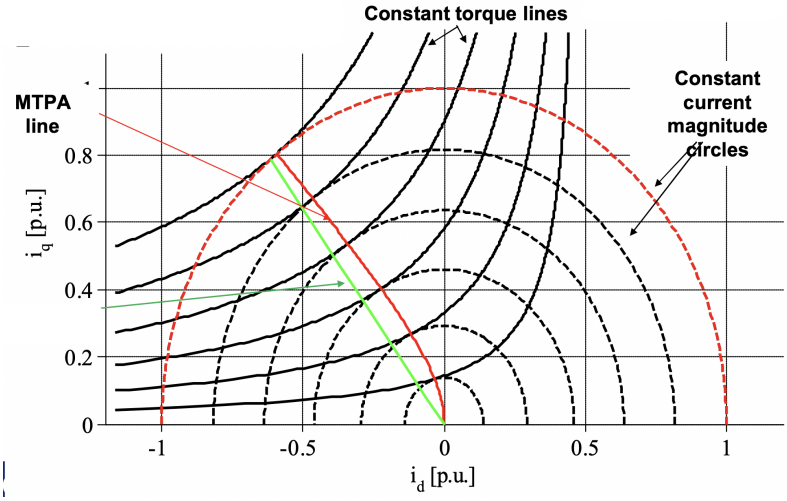

Figure 4.15: Graphical representation of maximum current on dq-plane.[6]

The voltage limit of a PMSM can be derived by neglecting the voltage drop of the stator winding resistance r_s and squaring and adding the d and q voltage equations. An equation for ellipse is obtained. The maximum voltage (maximum ellipse) is obtained from the equation 4.20. the maximum stator voltage $u_{s,max} = u_{dc}/3$. Where, u_{dc} is the DC link voltage. On the dq-plane the voltage limiting ellipse is centered around $(\Psi_{PM}/L_d,0)$, as can be seen in figure 4.16. The voltage limit coupled with the current limit forms a boundary condition for the operation region which cannot be exceeded to not damage the machine. The motor speed corresponding to the meet point of the current limit and the maximum voltage limit is called the *base speed*. As the rotor speed goes higher, the ellipse will shrink and then reduce to its center. The current limit and voltage limit are the two constraints for PMSM operation. The operation points should be in the common area of the current limit circle and the voltage limit ellipse.[10]

$$\frac{(i_d + \frac{\Psi_{PM}}{L_d})^2}{L_q^2} + \frac{i_q^2}{L_d^2} \leq (\frac{u_{s,max}}{\omega_r L_d L_q})^2 \tag{4.20}$$

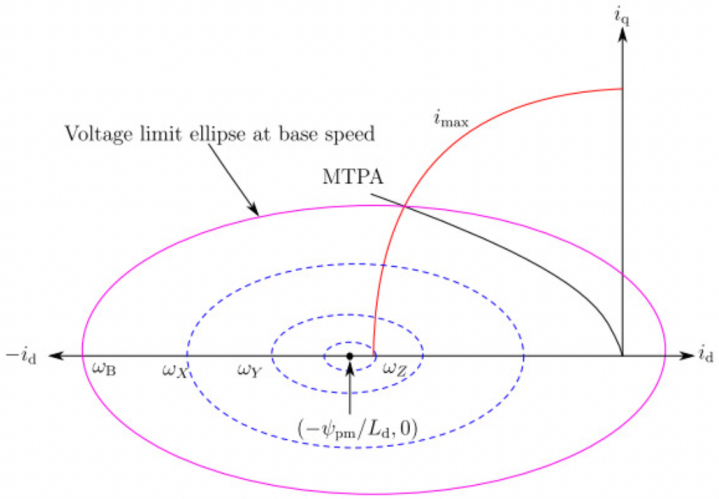

Figure 4.16: Voltage limit ellipse meets current limit circle. The black curve is MTPA line.[10]

The i_d and i_q reference values (for the controller) for MTPA is derived from the Torque equation expressed in flux linkages and currents. Currents i_d and i_q are inserted in the Torque equation in terms of i_s. Now the Torque equation is a current angle dependent equation. The obtained equation is differentiated with respect to current angle and equated to 0 (standard way of obtaining the maximum and the minimum point) to obtain the roots of a equation quadratic in cosine of current angle. The roots of the equation are derived and by fixing a current angle and substituting i_{sd} and i_{sq}, the torque equation is as in equation shown in the figure 4.17. This torque equation is solved for current magnitude $I_{mag,ref}$. If the voltage hits the limit, field weakening should be applied. This is the case when large speed window is required. In our case, the propeller speed will not increase the limit and we will not describe more about how it is done. [10]

$$\theta = \arccos\left(-\frac{\Psi_{PM}}{4(L_{sd}-L_{sq})I_{mag}} - \sqrt{\frac{1}{2}+\left(\frac{\Psi_{PM}}{4(L_{sd}-L_{sq})I_{mag}}\right)^2}\right)$$

$$T_e = \frac{3n_p}{2}(\Psi_{PM} I_{mag}\sin\theta + (L_d - L_q) I_{mag}^2 \sin\theta\cos\theta)$$

$$I_{mag,ref} = -\frac{\Psi_{PM}}{2(L_{sd}-L_{sq})\cos\theta} + \sqrt{\frac{2}{3n_p(L_{sd}-L_{sq})\sin\theta\cos\theta}T_{e,ref} + \left(\frac{\Psi_{PM}}{2(L_{sd}-L_{sq})\cos\theta}\right)^2}$$

$$i_{sd,ref} = I_{mag,ref}\cos\theta$$
$$i_{sq,ref} = I_{mag,ref}\sin\theta$$

Figure 4.17: Current references' calculations

On the output of the current controller a voltage magnitude limiter is used (the length of the voltage vector is limited). The limiter is set to the maximum value

the converter can produce, i.e. $V_{dc}/\sqrt{3}$, since amplitude invariant transformation is used. When this is implemented, there are chances of integrator part getting over-charged due to the limited response in i_s. Thus, we feed another error signal into the integrator which when $u_{s,ref} = u_{s,lim}$, limits the integration. Also, the gain H in the anti-windup loop is chosen to be $1/k_{pcd}$. The current controller with voltage limiter and antiwindup of the integrator is as in the figure 4.18. This is shown for d-current. The q-current controller block will be similar.

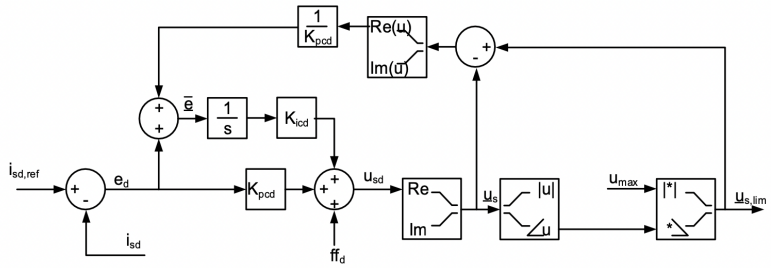

Figure 4.18: Current controller with voltage limiter and antiwindup of the integrator (d-current).[6]

In the current reference calculation block, a current magnitude limiter is used. It limits the continuous current magnitude to the rated current of the machine to protect it from overheating. The limiter is set to $I_{s,rated} \cdot \sqrt{2}$. But to have a better acceleration of the system the maximum converter current can be temporarily used. Figure 4.19 shows the implementation of a current limiter and voltage limiter. The figure also shows where the current transformation is implemented.

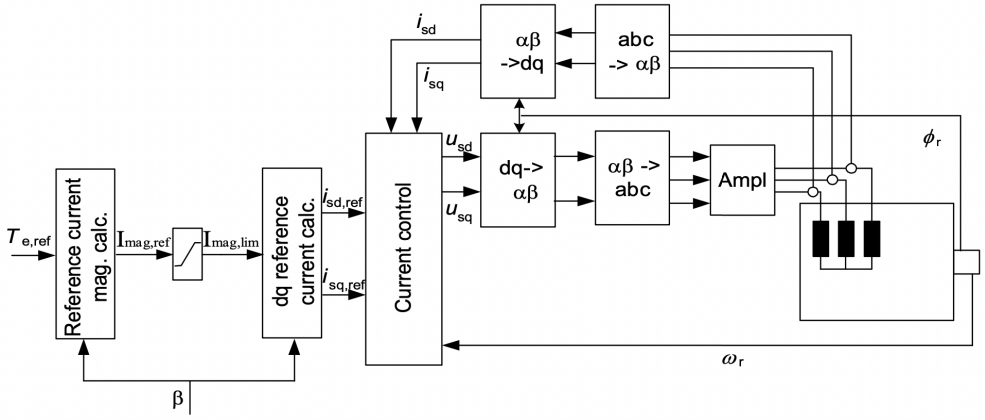

Figure 4.19: Block system of Machine and its current controller with the current limiter.[6]

4.2.3 Speed and position controller

When designing an outer controller, we assume that the inner controller is ideal, where, the actual state is equal to the reference. Active damping is implemented to reduce the impact of the disturbance T_l as done while designing a current controller. The active damping is implemented so that $G'_\omega(s)$ gets the same bandwidth (α_ω)

as the speed controller. The speed controller is also designed with IMC (equations 4.20). The block diagram of the speed controller with the antiwindup is as in the figure 4.21.

$$\textbf{Put}, T_{e,ref} = T'_{e,ref} - B_a\Omega_r \implies G'_\omega(s) = \frac{\Omega_r}{T'_{e,ref}} = \frac{1}{Js + B + B_a}$$

$$G_{cl,\omega}(s) = \frac{\Omega_r}{\Omega_{r,ref}} = \frac{\alpha_\omega/s}{1 + \alpha_\omega/s} = \frac{F_\omega(s)G'_\omega(s)}{1 + F_\omega(s)G'_\omega(s)}$$

$$\textbf{IMC} \implies F_\omega(s) = \frac{\alpha_\omega}{s}{G'_\omega}^{-1}(s) = \frac{\alpha_\omega}{s}(Js + B + B_a) = \alpha_\omega J + \frac{\alpha_\omega(B + B_a)}{s} = k_{p\omega} + \frac{k_{i\omega}}{s}$$

$$B_a = \alpha_\omega J - B$$

$$K_{p\omega} = \alpha_\omega J$$

$$K_{i\omega} = \alpha_\omega(B + B_a) = \alpha_\omega(B + J\alpha_\omega - B) = J_\omega^2$$

$$T_{e,ref} = (K_{p\omega} + \frac{K_{i\omega}}{s})(\Omega_{r,ref} - \Omega_r) - B_a\Omega_r$$

Figure 4.20: Design of speed controller as per IMC.

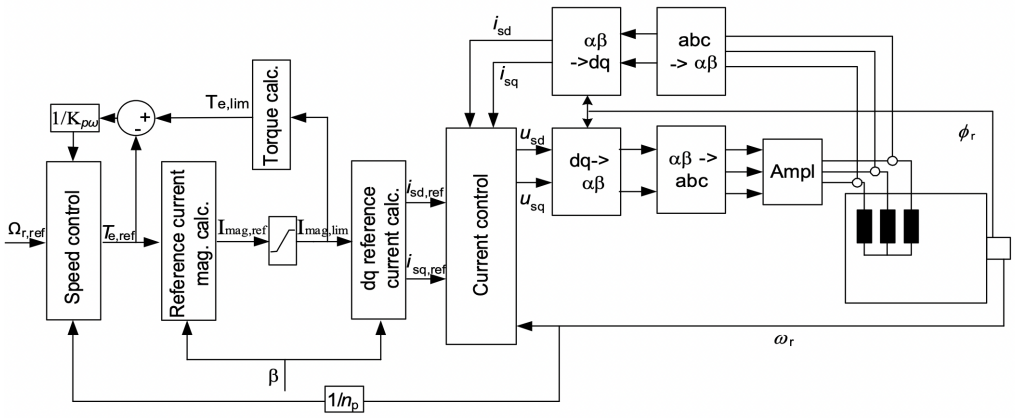

Figure 4.21: Speed controller with antiwindup.[6]

For the design of position controller, we again assume that the actual speed is equal to the speed reference. i.e., the inner control loop is much faster than the outer. A rule of thumb is a factor of 3 to 10. This gives $\alpha_\theta = 0.1\alpha_\omega$ and $\alpha_\omega = 0.1\alpha_c$. The outer controller shall not "see" the inner controller. The parameters can be derived similarly (eqns. 4.21 to 4.26).

$$\textbf{Put}, \Omega_{r,ref} = \Omega'_{r,ref} - D_a\Theta_r \implies G'_\theta(s) = \frac{\Theta_r}{\Omega'_{r,ref}} = \frac{1}{s + D_a} \tag{4.21}$$

$$\textbf{IMC} \implies F_\theta(s) = \frac{\alpha_\theta}{s} G_\theta^{-1}(s) = \frac{\alpha_\theta}{s}(s + D_a) = \alpha_\theta + \frac{\alpha_\theta D_a}{s} = K_{p\theta} + \frac{K_{i\theta}}{s} \tag{4.22}$$

$$D_a = \alpha_\theta \implies \tag{4.23}$$

$$K_{p\theta} = \alpha_\theta \tag{4.24}$$

$$K_{i\theta} = \alpha_\theta D_a = \alpha_\theta^2 \tag{4.25}$$

$$\Omega_{r,ref} = (K_{p\theta} + \frac{K_{i\theta}}{s})(\Theta_{r,ref} - \Theta_r) - D_a\Theta_r \tag{4.26}$$

5

Testing and tuning the controller

After recognizing the requirement of the component/system in a Model-based design approach, the verification steps should be undertaken before implementing it in the actual hardware. This chapter describes different verification steps in various environment.

5.1 MATLAB-Simulink environment

So far, we have developed the plant model of the PMSM and a controller on a paper. The developed model and the controller can be verified in a simulation environment to check if they're behaving as per the requirement. If the Controller works as desired, the input and output of the Controller is recorded, which will be used in the later stages of verification. This step is done in the MATLAB-Simulink environment and the steps involved is described below.

Once we have the dynamic model of the PMSM, the state-space equations of the model is derived to be able to implement in the MATLAB environment. The d and q components of the stator current, electrical rotor speed and electrical rotor position are chosen to be the states. The model should be implemented using Amplitude invariant transformation. The load torque should consist of speed dependent part and extra load torque. The inputs to the model should be d and q components of the stator voltage (transformed from a three phase voltage input) and extra load torque. The outputs of the model should be d and q components of the stator current (which is then transformed to three phase values), Torque component from the magnetic flux linkage T_{em}, Torque component from the reluctance T_{er}, Load torque T_L, mechanical rotor speed and the mechanical rotor position. The PMSM parameters to be used are in the Results part of this report. Figures 5.1 and 5.2 shows the Simulink models of the PMSM and state-space in dq co-ordinates. The flux linkage that can be used for calculations can be found by using the back-EMF of the machine. This is described in the Results section. The parameters are defined in a MATLAB file.

From the MTPA function derived earlier, the MTPA dq-currents that generates positive torque for current magnitudes 0 to rated current can be plotted using MATLAB-Simulink. This can be used to find the current angle for the rated current. This current angle in the Torque equation gives the analytical equation for calculating the needed current magnitude to generate a specific torque if the current angle is known.

Once we have the MTPA angle, the current controller can be implemented in the

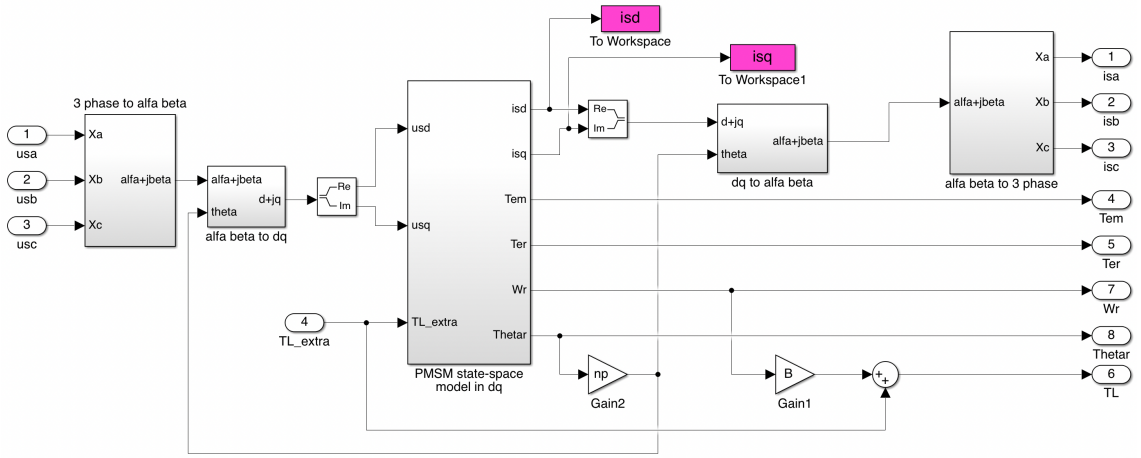

Figure 5.1: 3 Phase simulink model of a PMSM.

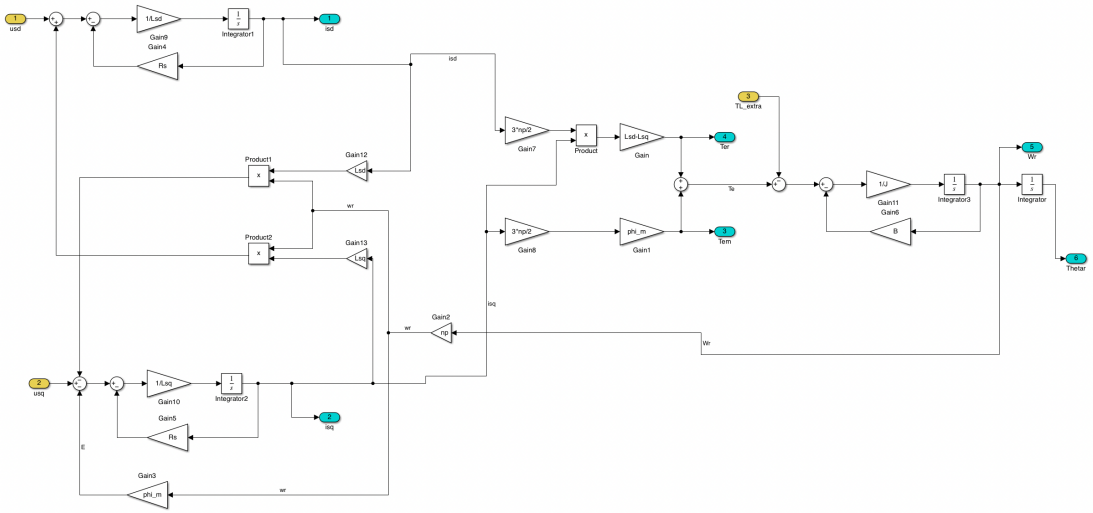

Figure 5.2: State-space model of PMSM in dq co-ordintes implemented in Simulink.

Simulink. The inputs should be Torque reference and the current angle. The feedforward of the back-EMF, Decoupling, Active damping, voltage magnitude limitation and anti-windup derived earlier should also be included. The mechanical angle should be converted to electrical angle for transformation. By doing this, the direction of the flux is oriented in the d-direction and the d-current is the flux current. The analytical equation derived is used to calculate the current magnitude from the torque reference and the current angle. Figure 5.3 shows the PMSM's process model block and the controller block. The speed controller can also be implemented in the same way which calculates the torque reference from the speed reference given. Figure 5.4 shows the transformations blocks (from 3-phase to *dq*-coordinates) of the measured values, current controller, and speed controller block inside the controller block. Figure 5.5 shows the structure of the current controller and 5.6 shows the structure of the speed controller.

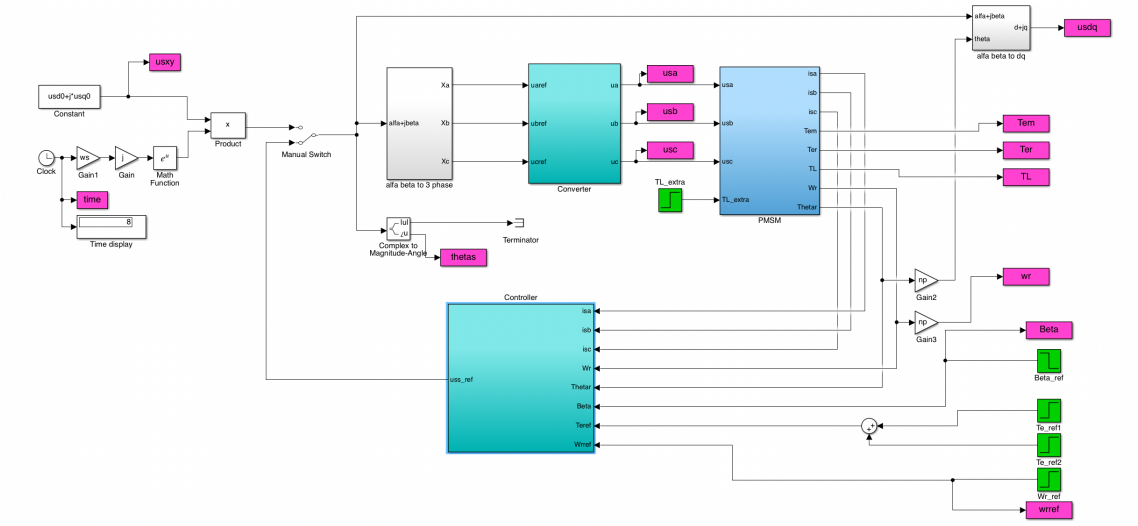

Figure 5.3: Process model and controller block in Simulink.

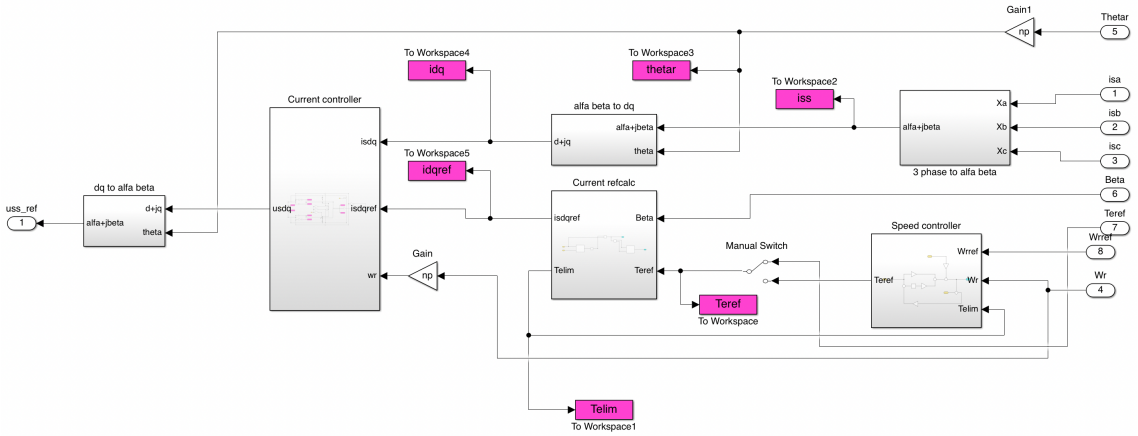

Figure 5.4: Tranformation blocks, current controller and speed controller.

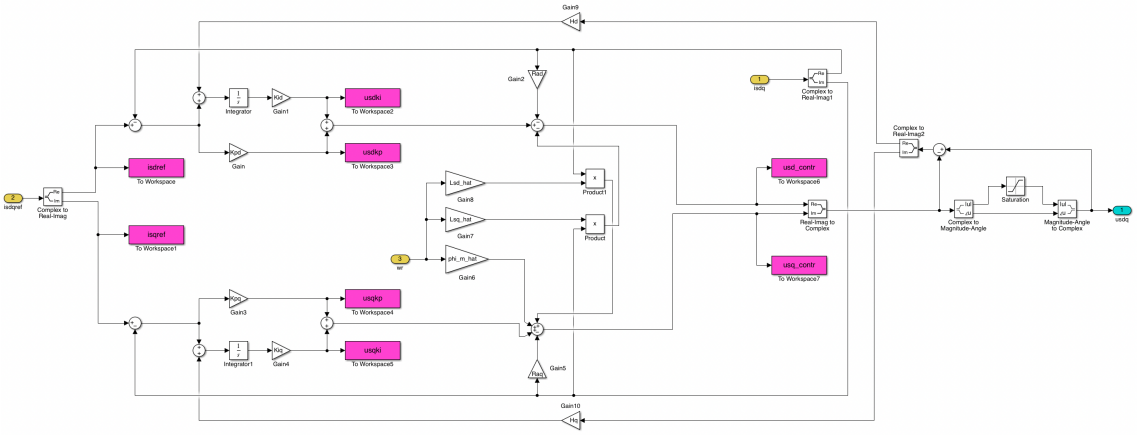

Figure 5.5: Current controller structure.

5.2 DSpace-Controldesk environment

High-performance control brings the difficulty to verify it through experiments because of its complexity. The hardware testing in *DSpace* acts as a bridge between

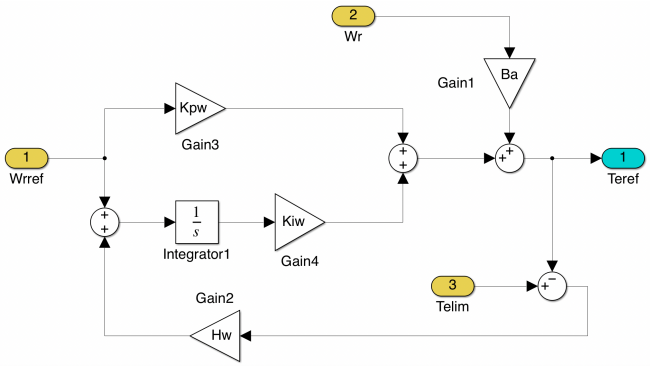

Figure 5.6: Speed controller structure.

the pure digital simulation and the experiment. It has been widely used in electric drives in different research. The system consists of DSpace system, computer, power circuit, interface circuits, and sensors. The system's main components can be seen in the figure 5.7. The Power circuit consists of a 2-way DC supply, a capacitor, and three phase inverter power module described earlier. The fault protection circuit is in the PCB mounted on the power module.

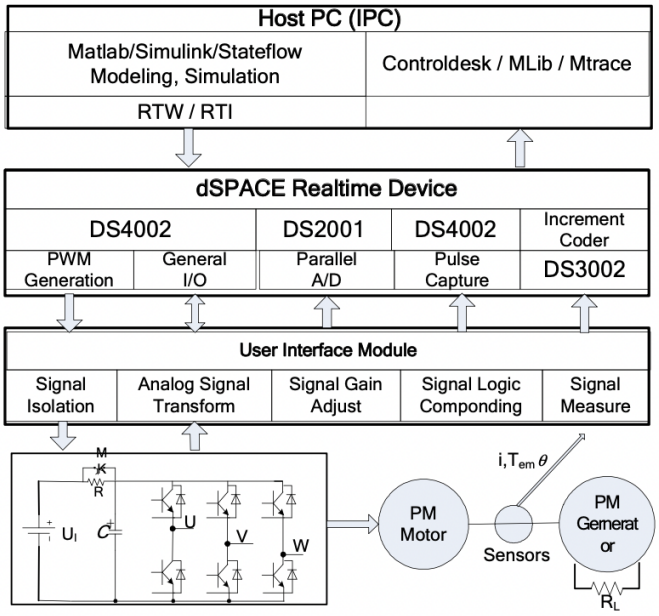

Figure 5.7: Components in Hardware testing using DSpace.

5.3 DSP-Code Composer Studio (CCS) environment

As discussed earlier, PWM is a control technique used in DC/AC inverters to regulate power supplied from DC power source to PMSM. Duty cycle is the output

variable which decides the PWM voltage depending on control function. In digital control, generating PWM signal is quite easy and writing programme can change the control signal pattern effectively. In digital domain, advanced algorithm implementation is relatively easy and faster. Thus, application of micro-controller and DSPs are increasing in inverter control. Sine-triangle PWM and Space Vector Pulse Width Modulated (SVPWM) technique are widely used for controlling complex inverter topologies. This section describes how a low cost *Delfino TMS320F28379D development board* is used for generating complex PWM signal for inverter operation and testing the control algorithm developed.[15]
EPWM channels on *TMS320F28379D* can be effectively utilized for high resolution PWM generation. Simple digital input/output can be programmed for PWM with limited switching frequency typically 2-5 kHz in this board. The *LAUNCHXL-F28379D* is a *C2000 Delfino MCU F28379D* launchpad development kit. This Launchpad C2000 development board has TMS320F28379D MCU which provides 800MIPS of total system performance between dual 200MHz C28x CPUs and dual 200MHz real time control co-processors (CLA). This microcontroller contains 1MB of on-board flash and includes highly differentiated peripherals such as *16bit/12bit ADCs, comparators, 12bit DACs, delta sigma sinc filters, HRPWMs, eCAPs, eQEPs, CANs* and more. The Launchpad development kit supports *12bit ADC* mode through the header pins and *16bit* mode can be driven with external differential signals.[15]
For example, to access *EPWM channels* for port A is pin *P16* for positive and *P56* to ground pin. Probes and Oscilloscope can be connected to this pin to check digital pulse of 3.3-5 volt before use. +5V external power supply is required to *F28379D development board* after flashing the programme to RAM to work independently. Hardware-in-loop in also possible with CAN support in this development board. CCS of Texas instruments is used as a software package to write and download the programme.[15]

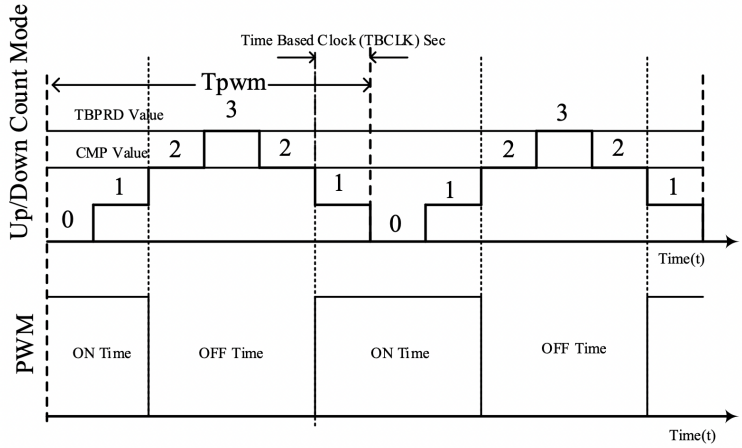

Figure 5.8: PWM generation with Up/Down counter using on board oscillator.[15]

Figure 5.9 shows the DSP used for testing as part of this thesis. The green board is the Encoder board which is used to measure the speed and position of the rotor. The chip system is enclosed in the Aluminum board to avoid the effect of EMI on

the signals. The signals are transferred between inverter and DSP through D-sub cable. The program to this chip is in the Appendix section of this report.

Figure 5.9: TMS320F28379D used in the testing along with Encoder (Green PCB board).

5.4 Test Setup

The test setup was made in the Electric Power Engineering department laboratory. An ABB DC motor was used as a constant speed load. The POD was immersed in a steel bucket so that cooling by natural water can be verified as a next step. A torque transducer was placed in between the PMSM and the DC motor for torque measurement. The PMSM coupled with DC motor can be seen in the figures 5.10, 5.11, and 5.12.

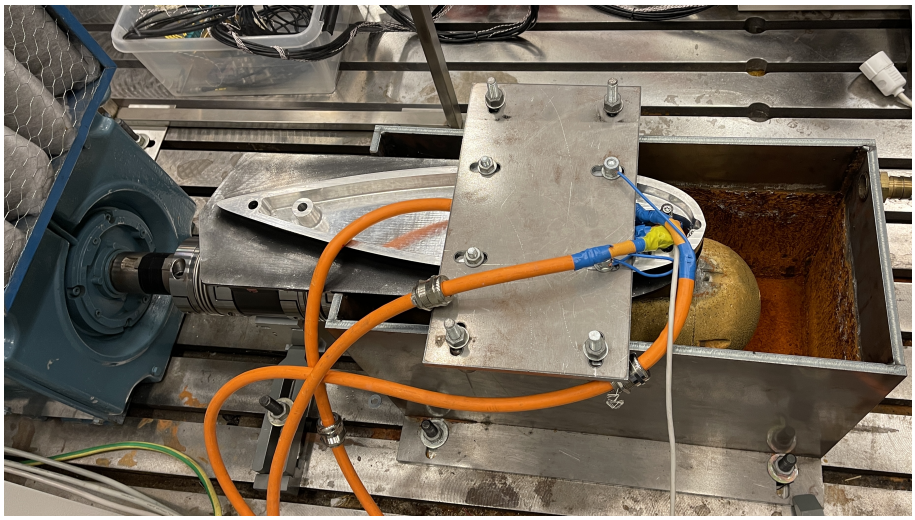

Figure 5.10: Image showing POD and the steel bucket.

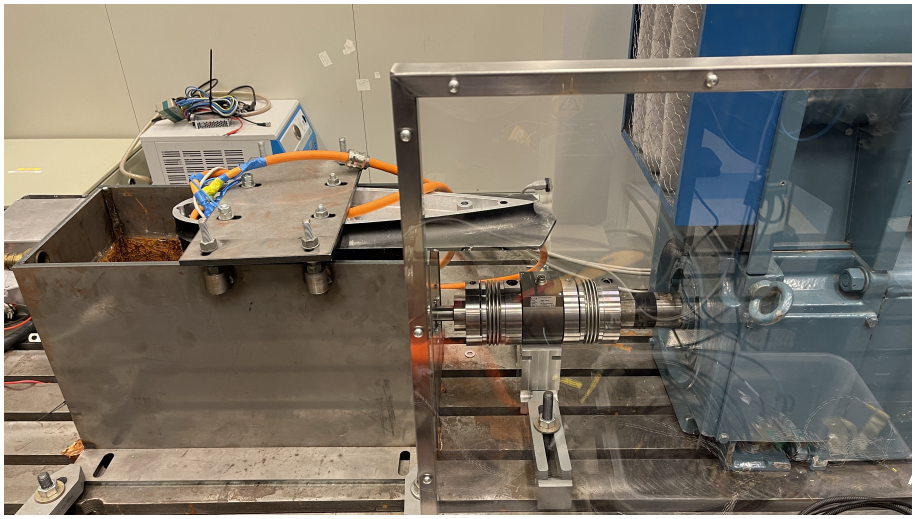

Figure 5.11: Image showing Torque transducer between the PMSM and the DC Motor.

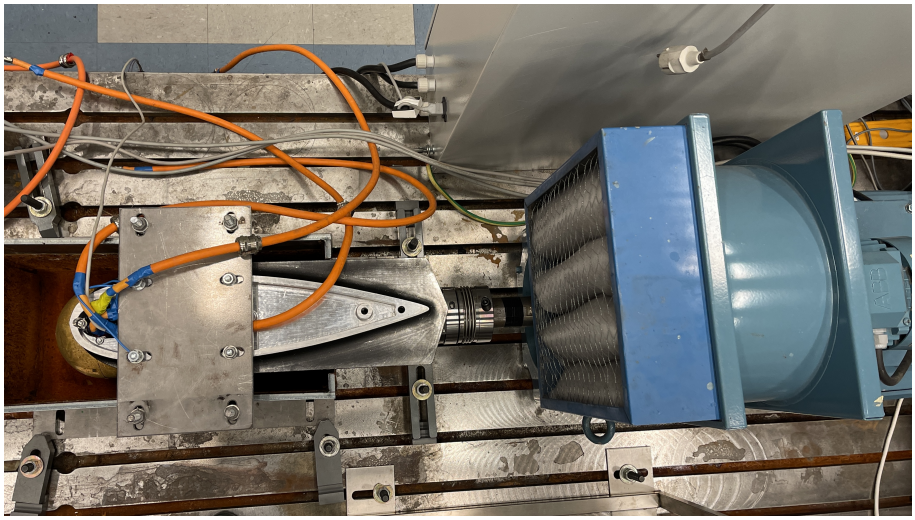

Figure 5.12: Image showing PMSM connected to the DC Motor.

6
Results and Conclusion

Before the verification was started, the PMSM parameters were measured. The table 6.1 shows the Series Resistance and Inductance values for different frequencies. The values are line-to-line but phase values are used. The graphs in figures 6.1 and 6.2 show the variation of Resistance and Inductance with respect to frequency.
For the calculations, we need the flux linkage. This can be found out by finding the back-EMF of the PMSM. The PMSM is coupled to a speed controlled DC-machine. When the speed of the DC machine (propeller's speed) was set to 750 RPM (Ω_{pp}), the line voltages (RMS) were noted. Figure 6.3 shows the waveforms of the three line voltages and its frequency ($f_{EM} = 285.9Hz$) as noted by the Oscilloscope. The electrical speed ($\omega_{EM} = 2\pi f_{EM}$) is found out to be 1796.36 rad/s. Using the line voltages, the amplitude of the phase voltage was found using equation 6.1. Thus, the flux linkage can be found using the equation 6.2. The exact gear ratio can be found using $k_{gear} = \Omega_{EM}/\Omega_{pp}$ and is equal to 5.72.

$$U_{ph,amp} = U_{line}\frac{\sqrt{2}}{\sqrt{3}} \tag{6.1}$$

$$\Psi_{PM} = \frac{U_{ph,amp}}{\Omega_{EM}} \tag{6.2}$$

After the electrical and electronic rigging was done in the *D-space* environment, a torque current (i_d) reference was given. For higher references, the PWM signals were disturbed. The 3-phase wires going from the converter module were suspected to be

Table 6.1: Line-to-line Resistance and Inductance measured in LCR-meter.

Frequency (Hz)	AB		BC		CA	
	R (m-ohm)	L (uH)	R (m-ohm)	L (uH)	R (m-ohm)	L (uH)
100	17.75	173.068	17.31	204.52	17.81	343.157
200	18.56	170.335	19.34	206.161	21.74	349.55
300	21.20	170.850	22.79	207.462	27.87	350.579
400	24.59	170.659	27.2	207.202	35.86	350.301
500	28.71	170.393	36.14	207.272	45.65	348.892
600	33.45	170.417	38.82	206.966	57.02	348.892
700	39.04	170.169	46.1	206.638	70.2	348.356
800	45.25	169.914	54.2	206.294	84.9	347.794
900	52.07	169.647	62.85	206.007	100.82	347.184
1000	59.48	169.417	72.71	205.333	118.24	346.956

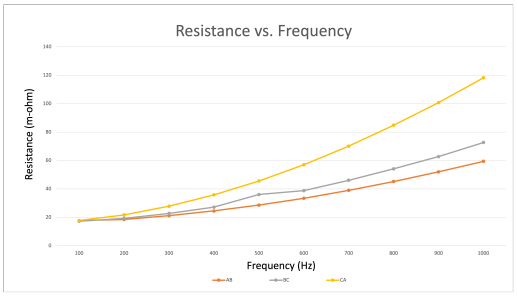

Figure 6.1: Graph showing Resistance vs. Frequency.

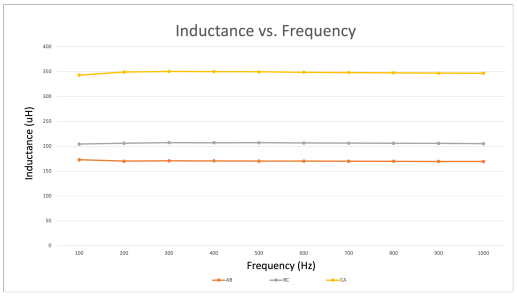

Figure 6.2: Graph showing Inductance vs. Frequency.

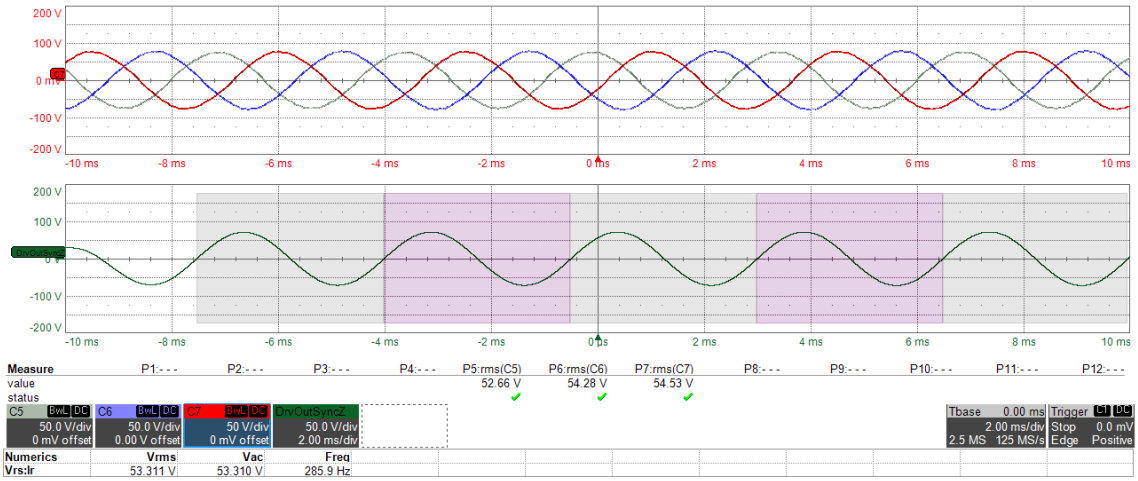

Figure 6.3: Line-to-line voltages and frequency for a propeller speed of 750 RPM.

creating the disturbance to the PWM signals near the module. This was observed in the Oscilloscope. Initially, these 3 phase wires were not sheathed. They were replaced with sheathed cables and properly grounded. This was found to be helpful in avoiding the disturbances. But we were not able to run the higher currents due to the limitation in the DC supply. We were able to reach these points on the Torque-Speed curve (Table 6.2 and figure 6.4).

As mentioned earlier, in order to test the POD system on-board a boat, a chip system was planned to be used to control the motor. After rigging the system in the *DSP-CCS* environment, for lower reference torque currents, the machine ran as expected. As we increased the current, the control was being lost. When this

Table 6.2: Torque and speed levels reached with the available DC supply and in *DSpace-Controldesk* environment

EM Speed (RPM)	Torque (Nm)
750	10
750	20
750	30
1500	10
2250	10

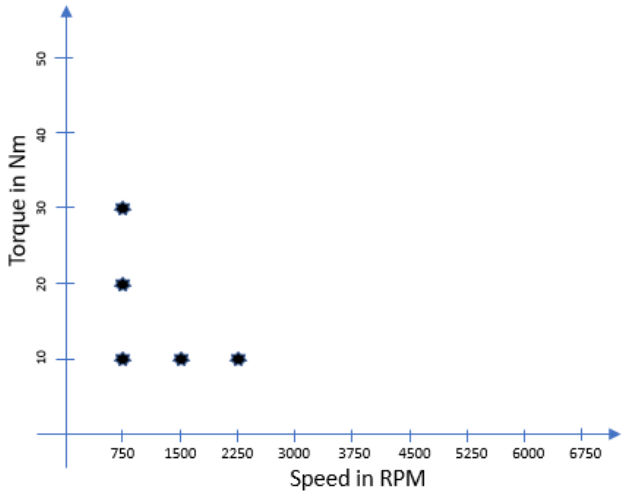

Figure 6.4: Torque-Speed points achieved in *DSpace-Controldesk* environment

happened, the chips (DSP and speed-position encoder) were exposed. Suspecting that there could be disturbances causing it, an Aluminum enclosure was created as shown in the figure 5.9. *D-sub* cables were used for measurements and PWM signals going to the module. This was not helpful to run the motor for higher currents.
Since the measurements were fluctuating a lot, we decided to use moving average for the measurement with slower bandwidth on the controller. Even this was not useful. A filter was also implemented on the current measurement signals. Which did not help as well. It was concluded from this that, a more sophisticated converter module which cannot be affected by the disturbances, should be used to conduct on-board testing. A module which is being used in the industries with effective metal housing should be used with a higher capable DC supply.
The future work can be summarized as follows. By replacing the current converter module and the DC supply, the motor should be tested for higher currents. The tuning of the controller should be done. Once this is achieved, Torque mapping of the motor should be done in the lab environment. Further, the DC supply should be replaced with Li-ion battery system and tested before we proceed with on-board testing.

Bibliography

[1] Truls Tveitdal, *Market barriers towards electric boats*, Department of Design, Norwegian University of Science and Technology - 2017.

[2] ETHW, *Electric boats*, Today's Engineer, Sept. 2013. [Online]. Available: `https://ethw.org/Electric_Boats`

[3] Company website. Available: `https://www.xshore.com/`

[4] Company website. Available: `https://candela.com/`

[5] Mario Porru, Marco Pisano, Alessandro Serpi, and Fabrizio Pilo, *Electrification of Leisure Boats: a commercial State-of-the-Art*, Novel Electric Propulsion Systems and Department of Electrical and Electronic Engineering, Cagliari, Italy - 2020

[6] *Electric Drives Lecture Slides* by Stefan Lundberg, Chalmers University of Technology, Gothenburg, Sweden.

[7] Yujing Liu, Jonas Ringsberg, Arash Eslamdoost, Felix Mannerhagen, and Stefan Lundberg, *Technical report - Propeller-integrated motor drive for electric medium size boats*, Department of Electric Power Engineering and Department of Marine Technology, Chalmers University of Technology, Göteborg - 2019.

[8] S. Bolognani and A. Faggion, *High efficiency multi-drive system for a hybrid electric catamaran with submersed PM synchronous motors* in 18th International Conference on Electrical Machines, lCEM'08, sept. 2008, pp. 1-5.

[9] R. Mecke, *Permanent magnet synchronous motor for passenger ship propulsion* in 13th European Conference on Power Electronics and Applications, EPE'09, sept. 2009, pp. 1-10.

[10] Yujing Liu, Junfei Tang, Nimananda Sharma, Artem Rodionov *Electrical Machines - Compendium, 1st edition*. Electric Power Engineering Department, Chalmers University of Technology, October - 2019

[11] Kim Sang-Hoon *Electric Motor Control: DC, AC, and BLDC Motors*. 1st. Amsterdam: Elsevier, 2017. isbn: 9780128123195.

[12] Lennart Harnefors *Control of Variable-Speed Drives*. Applied Signal Processing and Control, Sweden - 1 September 2002

[13] Mohan, Undeland, Robbins *Power Electronics - Converters, applications and design*. Wiley 2003, 3rd ed.

[14] Ke Song, Weiguo Liu, Guangzhao Luo *Permanent Magnet Synchronous Motor Field Oriented Control and HIL Simulation.* College of Automation, Northwestern Polytechnical University, Shaanxi Province, P. R. China. IEEE Vehicle Power and Propulsion Conference (VPPC), September 3-5, 2008, Harbin, China.

[15] Subhendu Bikash Santra, Krishnatreya Bhattacharya, Tanmoy Roy Chudhury *Generation of PWM Schemes for Power Electronic Converters.*

A

Appendix 1

A.1 Main file

```
// Included Files
#include <stdio.h>
#include <string.h>
#include <math.h>

#include "F28x_Project.h"

#include "API/Declaration_Constant_Values.h"
#include "API/Declaration_Class.h"
#include "API/Filter.h"

#include "main.h"

//===========================================================================
// Instance of objects
ADC_DataManager ADC_DataManager1   = ADC_DATAMANAGER_DEFAULT;
AL_Manager AL_Manager1 = AL_MANAGER_DEFAULT;
Control_Administrator ControlAdmin = CONTROL_ADMIN_DEFAULT;


//===========================================================================
// Main

void main(void)
{

// Step 1. Initialize System Control:
// PLL, WatchDog, enable Peripheral Clocks
    InitSysCtrl();

    parameter_initialization();

// Step 2. Initialize GPIO:
```

```
    InitGpio();

    GPIO_SetupPinMux(10, GPIO_MUX_CPU1, 0);
    GPIO_SetupPinOptions(10, GPIO_OUTPUT, GPIO_PUSHPULL);

    GPIO_SetupPinMux(31, GPIO_MUX_CPU1, 0);
    GPIO_SetupPinOptions(31, GPIO_OUTPUT, GPIO_PUSHPULL);

    GPIO_SetupPinMux(34, GPIO_MUX_CPU1, 0);
    GPIO_SetupPinOptions(34, GPIO_OUTPUT, GPIO_PUSHPULL);

// For this case just init GPIO pins for eQEP2 , ePWM1, ePWM2, ePWM3, ePWM4, ePWM5
// These functions are in the F2837xD_EPwm.c file

    InitEPwm1Gpio();
    InitEPwm2Gpio();
    InitEPwm3Gpio();
    InitEPwmTZGpio();
    InitEQep2Gpio();

// Step 3. Clear all interrupts and initialize PIE vector table:
// Disable CPU interrupts

    DINT;

// Initialize the PIE control registers to their default state.
// The default state is all PIE interrupts disabled and flags
// are cleared.
// This function is found in the F2837xD_PieCtrl.c file.
//
    InitPieCtrl();

// Disable CPU interrupts and clear all CPU interrupt flags:

    IER = 0x0000;
    IFR = 0x0000;

// Initialize the PIE vector table with pointers to the shell Interrupt

    InitPieVectTable();

// ISR functions found within this file.

    EALLOW;

    PieVectTable.ADCB1_INT = &ISR_ADC;
```

```
    PieVectTable.PIE16_RESERVED_INT = &ISR_MonitorLoop;  //function for reserved in
    EDIS;

    EALLOW;
    CpuSysRegs.PCLKCR0.bit.TBCLKSYNC = 0;
    Init_EPwm1();
    Init_EPwm2();
    Init_EPwm3();
    CpuSysRegs.PCLKCR0.bit.TBCLKSYNC = 1;
    EDIS;

    Init_EQEP();

    Init_DAC();

    PWM_off();

    LPF_OD1_Init(&LPF_OD1_i_s_d, _2_pi*500, 10e3, NEW);
    LPF_OD1_Init(&LPF_OD1_i_s_q, _2_pi*500, 10e3, NEW);
    LPF_OD1_Init(&LPF_OD1_omega, _2_pi*100, 10e3, NEW);


// Step 4. User specific code, enable interrupts:

    //--- Enable EPWM interrupt in the PIE: interrupt INT1.3
    //  PieCtrlRegs.PIEIER3.bit.INTx1 = 1;
    //  IER |= M_INT3;

    // ADC INT
    PieCtrlRegs.PIEIER1.bit.INTx2 = 1;
    IER |= M_INT1;

    // 2ms INT, use reserved interrupt INT5.4
    PieCtrlRegs.PIEIER5.bit.INTx4 = 1;
    IER |= M_INT5;

    EINT; // Enable Global interrupt INTM
    ERTM; // Enable Global real time interrupt DBGM

// Step 5. IDLE loop. Just sit and loop forever (optional):

    //--- Main Loop
    while (1)  // endless loop - wait for an interrupt
    {
        asm(" NOP");
    }
```

```
}

void parameter_initialization(void)
{

    /* -- PMSM Parameters -- */
    EM.N_pole_pair =   4;
    EM.R_s         =   9    * 1e-3;    // [Ohm]
    EM.L_d         = 120.12 * 1e-6;    // [H]
    EM.L_q         = 120.12 * 1e-6;    // [H]
    EM.psi_m       =  24.5  * 1e-3;    // [Wb]

    /* -- PMSM & Inverter Quantities -- */
    // DC-Link Voltage
    u_dc = 320;
    limit.u_s_amp = u_dc / _sqrt_3;
    limit.i_s_amp = 300;

    // Flux_Linkage_Calculation
    // See CalcMode_Flux in Declaration_Class.h
    ControlAdmin.UserCmd.Calc_Flux_Linkage = Flux_Const_L;

    // Stator Current Control Strategy Selection
    // See CtrlMode_I_stator in Declaration_Class.h
    ControlAdmin.UserCmd.Ctrl_Stator_Current = Is_Vref_Mod_Index;

    // PWM Algorithm Selection
    // See CalcMode_PWM in Declaration_Class.h
    ControlAdmin.UserCmd.Calc_PWM = PWM_Sine_Pwm_TriInject;

    // DC Link Voltage Measurement
    // See MeasMode_Vdc in Declaration_Class.h
    ControlAdmin.UserCmd.Meas_DC_Link_Voltage = Vdc_Assumption;

    // DAC Information
    // See DAC_MyFavorite in Declaration_Class.h
    ControlAdmin.UserCmd.DAC_MyFavorite_A = DAC_i_s_d;
    ControlAdmin.UserCmd.DAC_MyFavorite_B = DAC_i_s_q;

    /* -- PI Controller -- */
    stator_PI.alpha_c = _2_pi * 5;

    ControlAdmin.UserCmd.activation_stator.Active_Damping_Term = OFF;
    ControlAdmin.UserCmd.activation_stator.Anti_Windup_Term    = ON;
    ControlAdmin.UserCmd.activation_stator.Feed_Forward_Term   = ON;
```

```
ControlAdmin.UserCmd.activation_speed.Active_Damping_Term = OFF;
ControlAdmin.UserCmd.activation_speed.Anti_Windup_Term    = OFF;
ControlAdmin.UserCmd.activation_speed.Feed_Forward_Term   = OFF;

/* -- ADC -- */

ADC_DataManager1.ptr_Cmd_ADC_Calibration = (int*)&ControlAdmin.UserCmd.ADCCalib
ADC_DataManager1.Init(&ADC_DataManager1);

/* -- PWM -- */
// Frequency
f.fundamental   = 100;          // [Hz]
f.sw_abc        =  10 * 1e3;    // [Hz]

// Sampling
F_s = f.sw_abc;
T_s = 1 / F_s;

// Modulation index
m.a = 0;
m.f = f.sw_abc / f.fundamental;

// Period
period_decimal.abc  = 1 / f.sw_abc;
period_integer.abc  = round(100e6 / f.sw_abc / 4);

// Duty Cycle
duty_decimal.a  = 0;
duty_decimal.b  = 0;
duty_decimal.c  = 0;
duty_integer.a  = round(duty_decimal.a * period_integer.abc);
duty_integer.b  = round(duty_decimal.b * period_integer.abc);
duty_integer.c  = round(duty_decimal.c * period_integer.abc);

// Dead Band
dead_band_decimal.abc   = 1000 * 1e-9;  // [s]
dead_band_integer.abc   = round(100e6 * dead_band_decimal.abc / 2);
N_three_phase_deadband = 500 [ns] * 100 [MHz] / 2 = 25
N_three_phase_deadband = 100 [ns] * 100 [MHz] / 2 =  5

/* -- ADC -- */
// Flag_Calibration = 1;
// length_ADC_Data  = LENGTH_ADC_AVG_DATA;

/* -- Reference Update  -- */
```

```
    ref_update.rate_m_a         = 1.0e-5;
    ref_update.rate_i_s_d_ref   = 1.0e-3;
    ref_update.rate_i_s_q_ref   = 1.0e-3;

    ref_update.value_m_a        = 0;
    ref_update.value_i_s_d_ref  = 0;
    ref_update.value_i_s_q_ref  = 0;

    // Alarm manager initialization
    AL_Manager1.ptr_Cmd_ResetAlarm = (int *)&ControlAdmin.UserCmd.ResetAlarm;
    // Link to user's command
    AL_Manager1.Init(&AL_Manager1);

    // Start ADC calibration
    ControlAdmin.UserCmd.ADCCalibration = 1;

}
```

A.2 Interrupt function

```
#include <math.h>

#include "F28x_Project.h"

#include "API/Declaration_Constant_Values.h"
#include "API/Declaration_Class.h"
#include "API/Filter.h"
#include "API/MovingAverage.h"

#include "ISR.h"

//#define NUM  1000
//float Buffer[NUM];
//int index = 0;

interrupt void ISR_ADC(void)
{
/* -- Set GPIO 10 to indicate ISR start -- */
GPIO_WritePin(10,1);

    /* Trigger for ISR_MonitorLoop every demanded time,
    but it will be serviced after ISR_ADC is completed */
    Trigger_ISR_MonitorLoop();

/* -- EQEP -- */
```

```
    Calc_EQEP();

/* -- ADC -- */
    Update_ADC_Data();

    LPF_OD1_New_Calc(&LPF_OD1_i_s_d);
    LPF_OD1_New_Calc(&LPF_OD1_i_s_q);
    i_s.d = LPF_OD1_i_s_d.Out;
    i_s.q = LPF_OD1_i_s_q.Out;

//MovingAverage( &movavg_i_s_d );
//MovingAverage( &movavg_i_s_q );
//i_s.d = movavg_i_s_d.avg;
//i_s.q = movavg_i_s_q.avg;

i_s.amp = sqrt(i_s.d * i_s.d + i_s.q * i_s.q);
i_s.ang = atan2(i_s.q, i_s.d);

/* -- WPT Estimation -- */
// Est_WPT();

/* -- DAC -- */
// SetDACMonitorChannel();

/* -- Servo state machine -- */
RunServoStateMachine();

/* -- Controller -- */
RunController();

/* -- LED Flash -- */
switch(counter)
{
case 12500:
GPIO_WritePin(31, 1);
GPIO_WritePin(34, 0);
break;
case 25000:
GPIO_WritePin(31, 0);
GPIO_WritePin(34, 1);
counter = 0;
break;
}
counter++;

/* -- Clear INT Flag & Acknowledge INT -- */
```

```
// ADC ISR
// Clear INT flag for this timer
AdcbRegs.ADCINTFLGCLR.bit.ADCINT1 = 1; //clear INT1 flag
// Acknowledge this interrupt to receive more interrupts from group 1
PieCtrlRegs.PIEACK.all = PIEACK_GROUP1;

// EPWM ISR
// Clear INT flag for this timer
    // EPwm1Regs.ETCLR.bit.INT = 1;
    // Acknowledge this interrupt to receive more interrupts from group 3
    // PieCtrlRegs.PIEACK.all = PIEACK_GROUP3;

    /* --  Clear GPIO 10 to indicate ISR end -- */
    GPIO_WritePin(10,0);
}

int SetAlarm = 0;

interrupt void ISR_MonitorLoop(void)
{
    // Detect alarm
    AL_Manager1.Monitor(&AL_Manager1);

    // Reset alarm if users demand
    if( *AL_Manager1.ptr_Cmd_ResetAlarm )
    {
        AL_Manager1.ClearAllAlarm(&AL_Manager1);
        ClearTZEvent();
        *AL_Manager1.ptr_Cmd_ResetAlarm = 0;
    }

    if(SetAlarm)
    {
        AL_Manager1.SetAlarm(&AL_Manager1, AL_OVER_STATOR_CURRENT);
        SetAlarm = 0;
    }

    PieCtrlRegs.PIEACK.all = PIEACK_GROUP5;
}

#pragma FUNC_ALWAYS_INLINE(Trigger_ISR_MonitorLoop);
void Trigger_ISR_MonitorLoop(void)
{
    if(++LoopCnt_Monitor == LOOP_DIV_Monitor)
    {
        PieCtrlRegs.PIEIFR5.bit.INTx4 = 1;
```

```
        LoopCnt_Monitor = 1;
    }
}

#pragma FUNC_ALWAYS_INLINE(Update_ADC_Data);
void Update_ADC_Data(void)
{
    // Sampling and update ADC data
    ADC_DataManager1.Update(&ADC_DataManager1);

    i_s.a  = ADC_DataManager1.i_s_a.oData;     // [A]
    i_s.b  = ADC_DataManager1.i_s_b.oData;     // [A]
    i_s.c  = ADC_DataManager1.i_s_c.oData;     // [A]
    u_dc   = ADC_DataManager1.u_dc.oData;
    i_H_dc = ADC_DataManager1.i_H_dc.oData;

    if(ControlAdmin.UserCmd.Meas_DC_Link_Voltage == Vdc_Assumption)
        u_dc = 320.0;

    if(ControlAdmin.UserCmd.ADCCalibration)
        ADC_DataManager1.DoCalibration(&ADC_DataManager1);

    _1_over_u_dc = 1 / u_dc;
}

#pragma FUNC_ALWAYS_INLINE(GetDACMyFavoriteChannel);
void GetDACMyFavoriteChannel(DAC_MyFavorite MyFav,
volatile struct DAC_REGS *Dac_regs)
{
    switch(MyFav)
    {
        case DAC_i_H_dc:
            Dac_regs->DACVALS.all = i_H_dc * GAIN_i_H_dc;
            break;

        case DAC_i_H_dc_est:
            Dac_regs->DACVALS.all = WPT_est.i_H_dc_est * GAIN_i_H_dc_est;
            break;

        case DAC_i_f_ref:
            Dac_regs->DACVALS.all = i_f_ref * GAIN_i_f_ref;
            break;

        case DAC_i_f_est:
            Dac_regs->DACVALS.all = WPT_est.i_f_est * GAIN_i_f_est;
            break;
```

```
case DAC_T_f_est:
 Dac_regs->DACVALS.all = WPT_est.T_f_est * GAIN_T_f_est;
 break;

case DAC_i_s_ref_d:
    Dac_regs->DACVALS.all = i_s_ref.d * GAIN_i_s_d + BIAS_i_s_d;
    break;

case DAC_i_s_d:
    Dac_regs->DACVALS.all = i_s.d * GAIN_i_s_d + BIAS_i_s_d;
    break;

case DAC_i_s_ref_q:
    Dac_regs->DACVALS.all = i_s_ref.q * GAIN_i_s_q + BIAS_i_s_q;
    break;

case DAC_i_s_q:
    Dac_regs->DACVALS.all = i_s.q * GAIN_i_s_q + BIAS_i_s_q;
    break;

case DAC_i_s_a:
    Dac_regs->DACVALS.all = (i_s.a * 0.002 + 0.5) * 4095 ;
    break;

case DAC_i_s_b:
    Dac_regs->DACVALS.all = (i_s.b * 0.002 + 0.5) * 4095 ;
    break;

case DAC_i_s_c:
    Dac_regs->DACVALS.all = (i_s.c * 0.002 + 0.5) * 4095 ;
    break;

case DAC_u_s_ref_d:
 Dac_regs->DACVALS.all = u_s_ref.d * GAIN_u_s_ref_d *
 _1_over_u_dc + 2047.5;
 break;

case DAC_u_s_ref_q:
 Dac_regs->DACVALS.all = u_s_ref.q * GAIN_u_s_ref_q *
 _1_over_u_dc + 2047.5;
 break;

case DAC_u_s_ref_alpha:
 Dac_regs->DACVALS.all = u_s_ref.alpha * GAIN_u_s_ref_alpha * _1_over_u_dc
 break;
```

```
        case DAC_u_s_ref_beta:
         Dac_regs->DACVALS.all = u_s_ref.beta * GAIN_u_s_ref_beta * _1_over_u_dc +
         break;

        case DAC_u_s_ref_a:
         Dac_regs->DACVALS.all = u_s_ref.a * GAIN_u_s_ref_a *
         _1_over_u_dc + 2047.5;
         break;

        case DAC_u_s_ref_b:
         Dac_regs->DACVALS.all = u_s_ref.b * GAIN_u_s_ref_b *
         _1_over_u_dc + 2047.5;
         break;

        case DAC_u_s_ref_c:
         Dac_regs->DACVALS.all = u_s_ref.c * GAIN_u_s_ref_c *
         _1_over_u_dc + 2047.5;
         break;

        case DAC_PWM1_CMPA:
         Dac_regs->DACVALS.all = EPwm1Regs.CMPA.bit.CMPA
         * GAIN_PWM1_CMPA;
         break;

        case DAC_PWM2_CMPA:
         Dac_regs->DACVALS.all = EPwm2Regs.CMPA.bit.CMPA
         * GAIN_PWM2_CMPA;
         break;

        case DAC_PWM3_CMPA:
         Dac_regs->DACVALS.all = EPwm3Regs.CMPA.bit.CMPA * GAIN_PWM3_CMPA;

        case DAC_OMEGA_r:
         Dac_regs->DACVALS.all = OMEGA_r.rev_per_min * 0.0005 * 4095;
break;

        case DAC_omega_r:
Dac_regs->DACVALS.all = omega_r.rad_per_sec * 0.001193662073189 * 4095;
break;

case DAC_THETA_r:
Dac_regs->DACVALS.all = (THETA_r.rad * _1_over_2_pi + 0.5)* 4095;
break;

case DAC_theta_r:
```

```
Dac_regs->DACVALS.all = (theta_r.rad * _1_over_2_pi + 0.5)* 4095;
         break;

case DAC_QPOSCNT:
Dac_regs->DACVALS.all = EQep2Regs.QPOSCNT *0.341278439869989;
break;

case DAC_DEBCNT:
Dac_regs->DACVALS.all = eqep.debug_cnt;
break;

        default:
            Dac_regs->DACVALS.all = 0.5 * 4095;
            break;
    }

    if (Dac_regs->DACVALS.all > DAC_OFFSET)
        Dac_regs->DACVALS.all -= DAC_OFFSET;
    else if (Dac_regs->DACVALS.all > 4059)
        Dac_regs->DACVALS.all = 4059;
    else
        Dac_regs->DACVALS.all = 0;
}

#pragma FUNC_ALWAYS_INLINE(SetDACMonitorChannel);
void SetDACMonitorChannel(void)
{
GetDACMyFavoriteChannel(ControlAdmin.UserCmd.DAC_MyFavorite_A, &DacaRegs);
GetDACMyFavoriteChannel(ControlAdmin.UserCmd.DAC_MyFavorite_B, &DacbRegs);
}

#pragma FUNC_ALWAYS_INLINE(ResetController);
void ResetController(void)
{
    /* For stator current control */
    i_s_ref.d  = 0;
    i_s_ref.q  = 0;
    i_s_ref.amp = 0;
    i_s_ref.ang = 0;

    u_s_ref.a     = 0;
    u_s_ref.b     = 0;
    u_s_ref.c     = 0;
    u_s_ref.amp   = 0;
    u_s_ref.ang   = 0;
    u_s_ref.alpha = 0;
```

```
    u_s_ref.beta  = 0;
    u_s_ref.d    = 0;
u_s_ref.q     = 0;

u_s_ref_unlim.a    = 0;
u_s_ref_unlim.b    = 0;
u_s_ref_unlim.c    = 0;
    u_s_ref_unlim.amp   = 0;
    u_s_ref_unlim.ang   = 0;
    u_s_ref_unlim.alpha = 0;
    u_s_ref_unlim.beta  = 0;
    u_s_ref_unlim.d  = 0;
u_s_ref_unlim.q     = 0;

    ref_update.value_m_a     = 0;
    ref_update.value_d_H     = 0;
    ref_update.value_i_s_d_ref = 0;
    ref_update.value_i_s_q_ref = 0;
    ref_update.value_i_f_ref   = 0;

    stator_PI.P_d = 0;
    stator_PI.P_q = 0;

    stator_PI.I_d = 0;
    stator_PI.I_q = 0;

    stator_PI.i_s_d_error   = 0;
    stator_PI.i_s_q_error   = 0;
    stator_PI.feed_forward_d = 0;
    stator_PI.feed_forward_q = 0;
stator_PI.u_s_d_ADP   = 0;
stator_PI.u_s_q_ADP   = 0;
stator_PI.i_s_d_AWP   = 0;
stator_PI.i_s_q_AWP   = 0;

    m.a = 0;

    /* For field current control */
    ref_update.value_d_H = 0;
    WPT_ctrl.i_f_error = 0;
}

#pragma FUNC_ALWAYS_INLINE(RunController);
void RunController(void)
{
    // Return when servo off
```

```
    if(ControlAdmin.Status.ServoState == SERVO_OFF)
    {
        ResetController();
        return;
    }

    if(short_time_test.activation_flag == 1) Short_Time_Test_Activation();
    if(sequential_test.activation_flag != 0) Sequential_Test_Activation();

    /* -- Current Controller: Voltage Vector Calculation -- */
    Ctrl_Current();
    /* -- Three-Phase PWM: CMPA Calculation -- */
    Calc_PWM();
}

#pragma FUNC_ALWAYS_INLINE(RunServoStateMachine);
void RunServoStateMachine(void)
{
    SERVO_STATE NextServoState = SERVO_OFF;

    // If alarm occurs, clear the servo ready flag and the servo on command
    if(AL_Manager1.F_HasAlarm)
    {
        ControlAdmin.Status.F_ServoReady = 0;
        ControlAdmin.UserCmd.ServoOn = 0;
    }
    else
        ControlAdmin.Status.F_ServoReady = 1;

    // Allow to enter servo on state only if users demand and servo ready
    if(ControlAdmin.UserCmd.ServoOn && ControlAdmin.Status.F_ServoReady)
        NextServoState = SERVO_ON;

    // Servo state change
    if(NextServoState != ControlAdmin.Status.ServoState)
    {
        if(NextServoState == SERVO_ON)
            PWM_on();
        else
            PWM_off();

        // Update servo state
        ControlAdmin.Status.ServoState = NextServoState;
    }
}
```

```
void ClearTZEvent(void)
{
    EALLOW;

    // Clear TZ-OST1
    EPwm1Regs.TZOSTCLR.bit.OST1  = 1;
    EPwm2Regs.TZOSTCLR.bit.OST1  = 1;
    EPwm3Regs.TZOSTCLR.bit.OST1  = 1;
    EPwm4Regs.TZOSTCLR.bit.OST1  = 1;
    EPwm5Regs.TZOSTCLR.bit.OST1  = 1;

    // Clear TZ-OST2
    EPwm1Regs.TZOSTCLR.bit.OST2  = 1;
    EPwm2Regs.TZOSTCLR.bit.OST2  = 1;
    EPwm3Regs.TZOSTCLR.bit.OST2  = 1;
    EPwm4Regs.TZOSTCLR.bit.OST2  = 1;
    EPwm5Regs.TZOSTCLR.bit.OST2  = 1;

    // Clear TZ-OST3
    EPwm1Regs.TZOSTCLR.bit.OST3  = 1;
    EPwm2Regs.TZOSTCLR.bit.OST3  = 1;
    EPwm3Regs.TZOSTCLR.bit.OST3  = 1;
    EPwm4Regs.TZOSTCLR.bit.OST3  = 1;
    EPwm5Regs.TZOSTCLR.bit.OST3  = 1;

    // Clear TZ-DCAEVT1
    EPwm1Regs.TZOSTCLR.bit.DCAEVT1  = 1;
    EPwm2Regs.TZOSTCLR.bit.DCAEVT1  = 1;
    EPwm3Regs.TZOSTCLR.bit.DCAEVT1  = 1;
    EPwm4Regs.TZOSTCLR.bit.DCAEVT1  = 1;
    EPwm5Regs.TZOSTCLR.bit.DCAEVT1  = 1;

    EDIS;
}
```

A.3 EQEP Function

```
#include "F28x_Project.h"

#include "API/Declaration_Constant_Values.h"
#include "API/Declaration_Class.h"

#include "API/Transformations.h"
#include "API/MovingAverage.h"
```

```
#include "API/Filter.h"

#include "Calc_EQEP.h"

float NewTHETA_r_pu, Newtheta_r_pu, NewPosDelta, NewSpeedRps;

void Calc_EQEP(void)
{

    // --- Obtain new value considering offset of d-axis
    // make sure pu value lies between 0.0 and 1.0
    // electrical angle (theta_r)
    Newtheta_r_pu = (float)(EQep2Regs.QPOSCNT + eqep.Position_shift) * eqep.K_PosCn
    if(Newtheta_r_pu < 0.0)
        Newtheta_r_pu = 1.0 + Newtheta_r_pu;

    // Shift to -0.5 to 0.5, but zero position keeps the same
    if(Newtheta_r_pu > 0.5)
        Newtheta_r_pu -= 1.0;

    // Get SI unit
    theta_r.rad = Newtheta_r_pu * _2_pi;
    theta_r.deg = Newtheta_r_pu * 360.0;

    // Leave if unit timeout event not occurs yet
    if (EQep2Regs.QFLG.bit.UTO == 0)
        return;

    eqep.debug_cnt++;

    /* -- Speed Calculation: calculate by every Unit Timeout -- */
    eqep.Position_new = (float)EQep2Regs.QPOSLAT;
    NewPosDelta = eqep.Position_new - eqep.Position_old;

    // Forward rotation
    if(EQep2Regs.QEPSTS.bit.QDF == 1)
    {
        if(NewPosDelta < 0.0)
            eqep.Position_delta = NewPosDelta + eqep.Position_max;
        else
            eqep.Position_delta = NewPosDelta;
    }
    // Backward rotation
    else
    {
        if(NewPosDelta > 0.0)  // when across the index
```

```
            eqep.Position_delta = NewPosDelta - eqep.Position_max;
        else
            eqep.Position_delta = NewPosDelta;
    }

    // -- calculation -- //
    NewSpeedRps         = eqep.Position_delta * eqep.K_PosCnt2SpdRps;

    LPF_OD1_omega.In = NewSpeedRps;
    LPF_OD1_New_Calc( &LPF_OD1_omega );
    NewSpeedRps = LPF_OD1_omega.Out;

    omega_r.rev_per_min = NewSpeedRps * 60.0;
    omega_r.rad_per_sec = NewSpeedRps * _2_pi;

    OMEGA_r.rev_per_min = omega_r.rev_per_min / EM.N_pole_pair;
    OMEGA_r.rad_per_sec = omega_r.rad_per_sec / EM.N_pole_pair;

    eqep.Position_old = eqep.Position_new;

    EQep2Regs.QCLR.bit.UTO = 1;

}
```

B

Appendix 2

DEPARTMENT OF SOME SUBJECT OR TECHNOLOGY
CHALMERS UNIVERSITY OF TECHNOLOGY
Gothenburg, Sweden
www.chalmers.se

CHALMERS
UNIVERSITY OF TECHNOLOGY